Tests on the performance of Actuators for the CTA MST & Studies towards a new and fast testing setup for spherical CTA mirrors

Diplomarbeit

eingereicht von
Stephan Bressel

Eberhard Karls Universität Tübingen
Mathematisch-Naturwissenschaftliche Fakultät
Institut für Astronomie und Astrophysik
Abteilung Hochenergieastrophysik

Juli 2015

Erklärung

Hiermit versichere ich, dass die vorliegende Arbeit von mir selbständig verfasst wurde und keine anderen als die angegebenen Hilfsmittel und Quellen benutzt wurden. Alle wörtlich oder sinngemäß aus anderen Werken übernommenen Aussagen sind als solche gekennzeichnet. Die vorliegende Arbeit war bisher weder vollständig noch in wesentlichen Teilen Gegenstand eines anderen Prüfungsverfahrens und die Arbeit wurde weder vollständig noch in wesentlichen Teilen bereits veröffentlicht.

Ort, Datum	Stephan Bressel

Abstract

The *Cherenkov Telescope Array* (CTA) project is an initiative of over 200 institutes in 31 countries, currently in the prototyping phase with the first full prototypes in the field, to build two arrays of optical telescopes of different sizes. One array will be located in the southern and one in the northern hemisphere. These telescope arrays observe the sky, detecting extensive air showers caused by very high energy particles and photons that impact into the atmosphere. The electromagnetic component of these air showers contain ultra-relativistic electrons and positrons, which produce *Cherenkov light* that is radiated in a cone with a small opening angle towards the ground. By observing the Cherenkov light with the arrays, the air showers can be reconstructed and thus the properties of the very high energy particle or photon, like their kind, energy and origin, determined.
The Institut für Astronomie und Astrophysik Tübingen (IAAT) participates in the CTA project in two ways. For one, it develops *actuators* for the medium sized telescopes (MST). Actuators are part of the interface between the telescope dish and the mirror facets. They function like motorized legs with adjustable length mounted to the facets. When their length is changed so is the pointing of the mirrors. With this, the mirrors of one telescope can be aligned to reflect the light of a star onto the same spot of the telescope camera. Depending on the quality of the mirrors, the size of the light spots (PSF) reflected by the mirrors onto the camera vary. Larger light spots lead to a decreased resolution of the telescope. Also, the reflectivity of the mirrors is important, because it determines the sensitivity of a telescope. The IAAT has a setup developed by the Max-Planck Institut für Kernphysik (MPIK) Heidelberg to measure the PSF and reflectivity of spherical mirrors, as will be used for the CTA project in an order of 8000. A problem of this setup is the long duration of 6 to 8 hours of one measurement. Therefore, the IAAT develops a faster new setup.
After a brief introduction in some of the physics behind the Cherenkov telescopes (chapter 1), the CTA is introduced (chapter 2). Then the test on the prototype actuators designed by Buck Engineering are presented (chapter 3). In the final part of this thesis (chapter 4), the setup built by the MPIK Heidelberg to measure the PSF and reflectivity of spherical mirrors is tested on its usability for CTA mirrors and the feasibility of a new and faster setup is evaluated.

Zusammenfassung

Das *Cherenkov Telescope Array* (CTA) Projekt ist eine Initiative von über 200 Instituten aus 31 Nationen um zwei unterschiedlich große Teleskoparrays aus Teleskopen verschiedener Größen zu bauen und befindet sich gegenwärtig in der Prototyp-Phase mit den ersten kompletten Prototypen im Einsatz. Ein Array wird in südlichen und eines in der nördlichen Hemisphäre liegen. Die Teleskoparrays beobachten den Himmel um ausgedehnte Luftschauer zu sehen. Die gesuchten Luftschauer werden von hochenergetischen Teilchen oder Photonen ausgelöst, die in die mit der Erdatmosphäre wechselwirken und eine Kaskade an Teilchenreaktionen und - produktionen auslösen. Die elektromagnetische Komponente dieser Luftschauer beinhaltet ultra- relativistische Elektronen und Positronen, die *Cherenkov Licht* produzieren, das in einen Kegel mit schmalem Öffnungswinkel in Richtung Boden abgestrahlt wird. Durch das Beobachten des Cherenkov-Lichtes mit den Arrays können die Luftschauer rekonstruiert und so die Eigenschaften der hochenergetischen Teilchen oder Photonen, wie z.B. ihre Art, Energie und Herkunftsrichtung bestimmt werden.
Das Institut für Astronomie und Astrophysik Tübingen (IAAT) leistet 2 Beiträge zum CTA Projekt. Zum einen entwickelt es *Aktuatoren* für die Teleskope mittlerer Größe (MST). Aktuatoren sind Teil des Interfaces zwischen der Teleskopschüssel und den einzelnen Spiegelfacetten, aus denen der gesamte Reflektor zusammengesetzt wird. Die Aktuatoren funktionieren wie motorisierte Stützen anpassbarer Länge, die an den Spiegelfacetten angebracht sind. Wenn ihre Länge geändert wird, so ändert sich auch die Ausrichtung der Spiegel. Damit können alle Spiegel eines Teleskops auf denselben Punkt der Teleskopkamera ausgerichtet werden. Abhängig von der Qualität der Spiegelfacette variiert die Größe der von ihnen auf die Kamera reflektierten Lichtpunkten. Größere Lichtpunkte führe zu einer Verringerung der Auflösung des Teleskops. Zudem ist die Reflektivität der Spiegel wichtig, da sie die Sensitivität des Teleskops bestimmten. Das IAAT betreibt einen Messaufbau, entwickelt vom Max-Planck Institut für Kernphysik (MPIK) Heidelberg, zur Messung der PSF und Reflektivität von sphärischen Spiegeln, wie es für eine Größenordnung von 8000 Spiegeln für das CTA Projekt geplant ist. Ein Schwäche dieses Messaufbaus ist die lange Messzeit von sechs bis acht Stunden pro Spiegel. Daher entwickelt das IAAT einen Messaufbau, der Messungen in einer kürzeren Zeit erlaubt.
Nach einer kurzen Einführung in einen Teil der Physik hinter CTA (Kapitel 1) wird das CTA Projekt selbst vorgestellt (Kapitel 2). Danach werden die Tests an Aktuatorprototypen, entworfen von Buck Engineering, vorgestellt (Kapitel 3). Im letzten Teil dieser Diplomarbeit (Kapitel 4) wird der Messaufbau, entworfen vom MPIK zur Messung von PSF und Reflektivität von sphärischen Spiegeln auf seine Verwendbarkeit für CTA Spiegel geprüft und die Machbarkeit eines neuen und schnelleren Messaufbaus untersucht.

Contents

Chapter 1

Introduction

This chapter will give a brief introduction to the spectrum of high energy cosmic particles, their correlation to high energy photons and how the classical detection of those with space observatories is limited. The explanations will follow the book by [13].

1.1 High energy particles

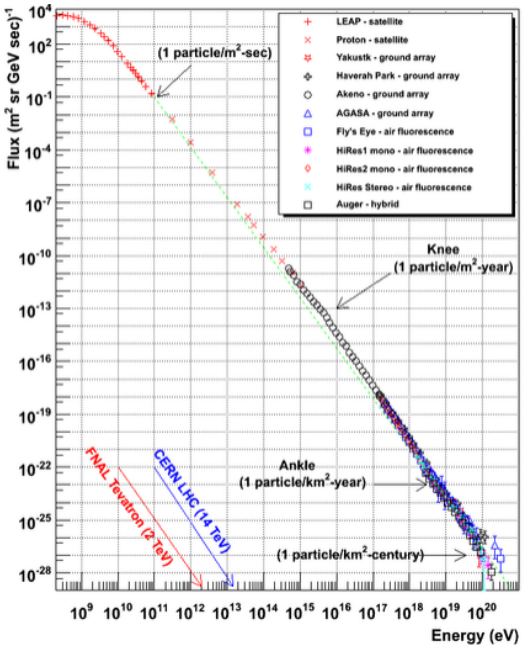

Figure 1.1: The cosmic ray spectrum for the energy range of 10^9 eV to 10^{20} eV measured with various experiments. It is composed mainly of protons (90%) and α-particles (9%). Originally published by Swordy (2001), and modified by Dr. William Hanlon of the University of Utah (http://www.physics.utah.edu/∼whanlon/spectrum.html)

At the beginning of the 20th century it was discovered that there is a constant radiation ionizing the atmosphere. This has been measured first by Hess in 1912 and Kolhoerster in 1914. For their experiments they flew up to heights of five and nine km in open balloons. During the last century more save and better means have been developed to study the high energy cosmic radiation. Today we know it consists of 99% nuclei, fully ionized atoms. Following the abundance of elements in the universe it consists of about 90% protons and

about 9% α-particles. Figure 1.1 shows the cosmic ray spectrum for energies above 10^8 eV, measured by various experiments. It extends to energies even above 10^{20} eV. As comparison, in the CERN Large Hadron Collider (LHC) charged particles like protons move through a very large ring pipe with over 26 km length. They get accelerated and are kept on track by the strong magnetic fields of huge superconducting coils, but only to energies of up to $14{\times}10^{12}$ eV.

Where the particles of the cosmic radiation come from and how they get accelerated to such high energies are amongst the leading questions for modern high energy astrophysics. The high energy cosmic ray spectrum can be described by a power law with an index depending on the energy range. In the energy range from 10^{10} eV to about 10^{15} eV, the so called knee, the index is -2.7. From the knee to energies of 10^{18} eV, the ankle, the index changes to -3.0, before returning back to -2.7 again. First of all, a power law means that the particles originate in a non-thermal process. One theory of such a process, capable to produce such high energy particles is the (first oder) *Fermi acceleration* or diffuse shock acceleration. The Fermi acceleration describes the acceleration of charged particles , e.g. an electron, in the presence of a shock front by stochastic means. Both sides of the shock front can be looked upon as gas clouds reflecting the electron. A very much simplified description is the following: Starting behind a shock front, surrounded by shocked material the electron's movement gets randomized by turbulent magnetic fields. These turbulences can be caused by other charged particles that interact with the shock front. With a certain probability the electron crosses through the shock front and in average it will gain energy. Right after the crossing the electrons movement is randomized again by the turbulent magnetic fields. Thus, there is the same probability as before it moves towards shock front again and crosses it another time. Then the electron has gained energy again. Now everything can start from the beginning.

In principle the energy a charged particle can gain through this process is only limited by how many times it can cross the shock front. And this is limited by the lifetime of the shock. Of course less and less particles are accelerated to higher energies, because only a few move in the right direction after the randomization. The flux of high energy particles produced by this process follows a power law with an index of -2. The gap between the power law index of -2 from the Fermi acceleration and the indexes from fits to the spectrum of cosmic particles can be explained by an energy dependent escape of the cosmic rays, that softens the spectrum to index to about -2.7.

The knee and the angle in the spectrum of cosmic rays can mean either a change in the effectiveness of production of high energy particles for such energies or a change in the type of source and production process. For the Fermi process a shock front and free charged particles with already higher energies are required. There are two well know types of sources with shock fronts: Supernova Remnants (SNR) and Active Galactic Nuclei (AGN). At the end of their life, massive stars usually die in a supernova explosion. During that explosion they eject most of their mass into space. The ejected material is accelerated to velocities greater than the speed of sound and is forming a forward shock front. The shock front sweeps up the surrounding interstellar medium, increasing the density of the material in front of it. When the swept up material reaches a high enough density, a part of the forward shock is reflected and forms another (backwards) shock front moving towards the center of the remnant. During the supernova explosion various processes occur and the ejecta consist of various components. But most of it is ionized and free charged particles are present with enough energy for the Fermi acceleration to start.

If the progenitor star had enough mass, its core collapses to a state of matter so dense, that the gravitational forces of this are so strong that not even light can escape from it. Therefore the name black hole. The centers of galaxies usually harbor giant black holes around which all

the stars and other galactic matter circle. Black holes can accrete mass from their surrounding and grow from this. The mass can not just fall onto the black hole directly but forms a disk around it. Perpendicular to the plane of the disc two jets can form. These jets are formed by accelerated particles following magnetic lines. Some of giant black holes in the center of a galaxy are more luminous than all the stars in their galaxy together. These are called AGN. A sketch of an AGN can be seen in Figure 1.2 right. AGNs also have shock fronts running through the jets, enabling Fermi acceleration. It is believed that the part of the spectrum of high energy cosmic rays from lower energies up to the knee is produced in galactic sources, e.g. SNRs. At the knee the particles produced by the galactic sources die out, e.g. due to the limits of the SNR's lifetimes. From here the spectrum is dominated by extragalactic particles produced in AGNs and unknown sources. Another theoretical source for high energy particles is the decay of heavy dark matter particles. Finding a source radiating in high energies but not in low energies would be evidence of the existence of dark matter.

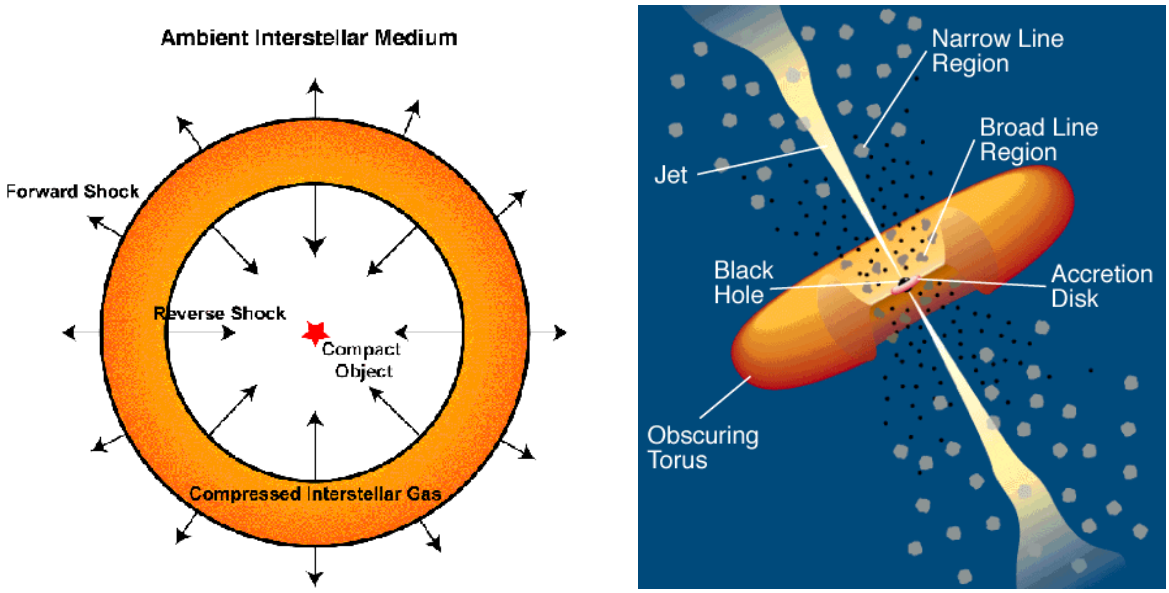

Figure 1.2: left: Sketch of an SNR. During the supernova explosion the matter of the dying star is accelerated to speeds faster than sound and forms a shock front sweeping up the interstellar medium in front of it. When the swept up material reaches a high enough density, a part of the forward shock is reflected and forms a second shock front running toward the center of the remnant. (Source: https://heasarc.gsfc.nasa.gov/docs/objects/snrs/snrstext.html) right: Drawing of an AGN. (Source: [17])

1.2 High energy photons

High energy particles that are accelerated by the Fermi acceleration are electrically charged and interact with magnetic fields. This has two consequences. First, when they move through a magnetic field their movement direction is altered by the Lorentz force. The galactic magnetic field of our galaxy might not be strong. But to reach Earth, the particles have to travel a very long distance and even slight changes in their moving direction have a strong effect, thus the galactic magnetic field can trap high energy charged particles and randomize them. Furthermore, the longer a particle has to travel, the higher the chance is it crosses through a part of the galactic plane with stronger magnetic fields or even to get close to

a black hole or a neutron star. Because of this, charged particles do not carry a reliable information of their origin. However, for photons this does not apply.
The Fermi acceleration occurs at places with a shock front and magnetic field turbulences. The particles that are accelerated to high energies are charged, move through the magnetic field and thus emit synchrotron radiation. They also move in the electric field of other particles and ions, leading to the emission of bremsstrahlung. The high energy particles can also interact with lower energy photons. Through inverse Compton scattering the particles lose energy to the photons. When high energy protons or nuclei interact with the ambient material in the sources, sort lived hadrons can be produced. Important for the production of energy photons is the production chain of the π^0 mesons. They are mainly produced in proton-proton collisions and decay fast into two photons.
Collisions between high energy photons and other photons in the Galaxy or Universe can lead to the production of electron-positron-pairs, if both photons together have an energy above the threshold. The cosmic microwave background (CMB) is present everywhere in the universe. Its photons have energies of around 6×10^{-4} eV. High energy photons with energies higher than 4×10^{14} eV start to interact with the CMB and thus their mean free path is much more limited. Photons of this very high energy arriving on Earth have to be generated at distances not larger than 10 Mpc.
The sources of high energy particles are sources of high energy photons, too. And the high energy photons arriving on Earth have not been affected by interstellar magnetic fields and still carry the information about their origin. This makes it possible to study the sources of high energy particles with detectors for high energy photons.

1.3 High energy photon detection

To detect photons, their interaction with matter is used. There are three different kind of relevant interactions:

- Photoelectric Absorption: The incoming photon interacts with a bound electron of an atom of the material. From the photon the electron gets enough energy to leave the atom. In this process the atom is ionized and the photon is absorbed.
- Compton Scattering: The incoming photon scatters on a quasi-free electron of the material. The photon is not absorbed, but it loses a part of its energy to the electron. The electron does not gain as much energy as it would through photoelectric absorption, but it is still enough to be raised to a free state and thus the atom to be ionized too.
- Pair production: When a photon has an energy greater than the rest mass of an electron and a positron together of two times 511 keV, it can form a positron-electron pair in the presence of the electrical field of the a nucleus. The presence of an electric field is necessary to ensure the conservation of momentum and energy.

Figure 1.3 shows a plot of the absorption coefficients against the photon energy for photons in matter (lead). The dashed lines represent the three different interaction possibilities and the solid line total value for any interaction to happen. All three photon interacting with a detector material produces free charges. By applying constant voltages they can be collected and read out. For more than 100 MeV photon energy the absorption coefficient for Compton scattering and photoelectric absorption is negligibly small and only electron-positron pair production occurs.
As stated in Chapter 1.2, high energy photons are produced by the interaction of high energy

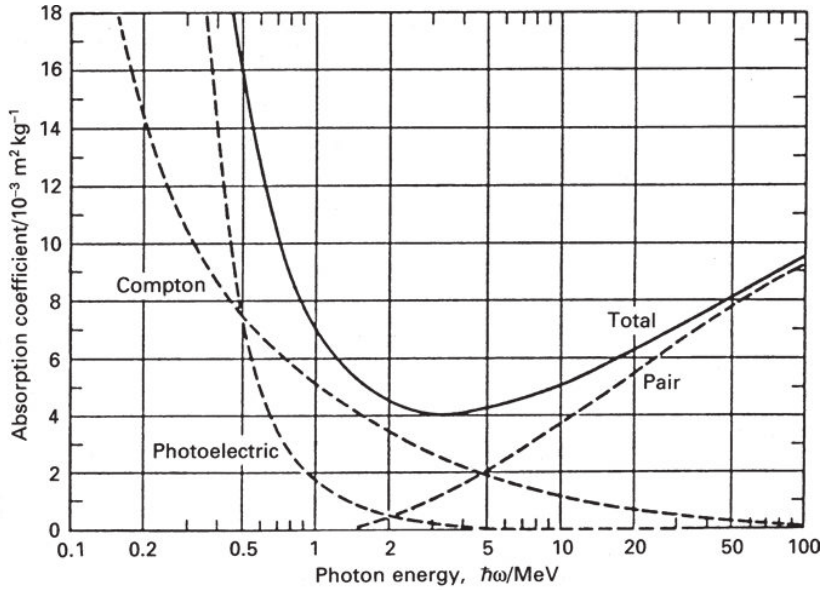

Figure 1.3: The different absorption coefficients for photons in the energy range from 0.1 MeV to 100 MeV in lead. At 100 MeV Compton scattering and photoelectric absorption can be neglected and the total absorption coefficient is dominated by pair production. (Source: [13])

particles with their surrounding. Therefore, the spectrum of high energy cosmic photons follows the spectrum of high energy cosmic rays. This means that measuring photons with higher energies is more difficult due to the strongly decreasing flux. To still measure a sufficient amount of events for higher and higher energies, larger and larger collecting areas are required. This sets a limit to the energy of photons that can be observed with space telescopes and detectors. To build a detector in space with a collection area of several km^2 is impossible for logistical and financial reasons. Among the present operating space observatories the Fermi Gamma-ray Space Telescope [14] can detect photons with the highest energy of 300 GeV. 300 GeV is still many orders of magnitude too small to probe very interesting parts of the cosmic ray spectrum like the knee. This means that other methods of detection are required.

Chapter 2

Ground based observations of high energy photons

This chapter will briefly explain the Cherenkov method for the detection of very high energy photons and the concept of Cherenkov telescope arrays. Afterwards the Cherenkov Telescope Array, a project to built the largest Cherenkov telescope array yet, and its design will be introduced.

2.1 Air Showers and Cherenkov light

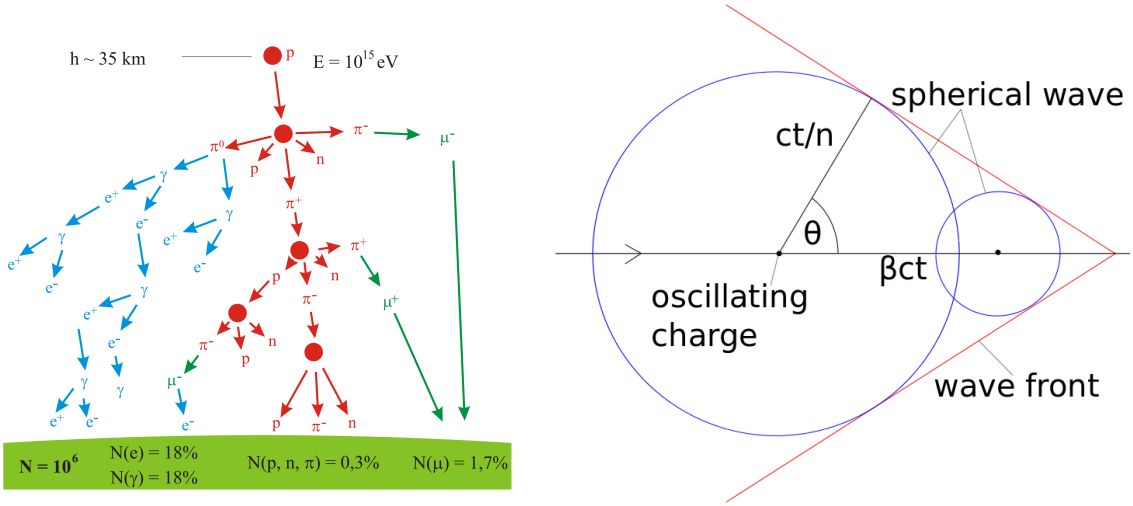

Figure 2.1: left: Particle cascade, caused by a primary high energy proton hitting the atmosphere, with its 3 branches. The electromagnetic branch in blue, the hadronic branch in red and the leptonic branch in green. (Source: https://en.wikipedia.org/wiki/Air_shower_%28physics %29#/media/File:AirShower.svg) right: Forming of an electromagnetic wavefront, caused by a charged particle traveling through a medium from left to right with a speed faster than the phase velocity of light: $\beta > \frac{1}{n}$. c is the speed of light in vacuum, t the time, n the refraction index and $\beta = \frac{v}{c}$, and the velocity of the particle is v.

When a high energy particle hits the Earth's atmosphere it interacts with air particles and initiates a cascade of particle reactions. Such cascades, called *air showers*, look different

in detail, depending on the primary particle. Figure 2.1 left illustrates an air shower caused by a proton:
A proton is colliding with a nitrogen atom of the atmosphere. In the collision the nitrogen is destroyed and many new particle, mostly pi-mesons but also hadrons like protons and neutrons, are created. The produced pions initiate three subchains: The hadronic chain (red), the muon chain (green) and the electromagnetic chain (blue). For the latter one, the Π^0 decays to photons. The photons interact with the electric fields of air particles and their nuclei, resulting in electron-positron pair production. The electrons and positrons emit new photons as bremsstrahlung which result in pair production again. This continues until the electrons and positrons energies fall under the pair production threshold of 1.022 MeV. The reaction chain for a primary photon hitting the atmosphere is the same as the electromagnetic chain for protons after the Π^0 decay.
If a charged particle moves through a dielectric medium, it will polarize the medium at its location by attracting charged particles of the medium to it or pushing them away depending on their charge. After the high energy particle has moved further the particles of the medium swing back to their original position and start oscillating around it. These are electrical dipole oscillations emitting the electrons kinetic energy as optical light. If the charged particle moves with a speed faster than the phase velocity of light in this medium, the particle will create new dipoles in front of the electromagnetic waves emitted by the dipoles. As illustrated in Figure 2.1 right, this leads to a pile-up effect producing a wavefront with a narrow angle to the moving direction of the particle. This optical and directed light is called *Cherenkov light*. Such Cherenkov light is produced by all charged particles in an air shower initiated by a high energy particle or photon. Of course only while their energy is above a certain threshold at which the particles speed is equal to the phase velocity of light in the surrounding medium. How much Cherenkov light photons are produced and arrive on ground depends on the number of electron-positron pairs and their energies. This in turn depends on the energy of the primary particle that initiated the air shower. The mass of the primary particle determines the kinematics of the collision with the air particle, too. High energy photons start the air shower by just decaying into a electron-positron-pair, which then emits Bremsstrahlung-photons which decay to electron-positron-pairs again, and so on. The decaying leads to a very narrow and round shape of the air shower. In the first collision of a proton with a nitrogen atom in the air, a lot of different particles are produced that also interact by collisions with their surrounding. This is a much more chaotic and less statistically uniform process. Such air showers have a wider shape due to a higher later momentum, and more intrinsic structures. These differences in shape, which are reflected by the produced Cherenkov light, make it possible to distinguish between photon and hadron induced air showers. Figure 2.2 show the results of simulations for a 300 GeV photon and a 1 TeV proton respectively. Before the collision with an air particle, the direction in which the primary particle travels is not altered. Hence, the air shower points exactly towards the direction the high energy particle or photon came from. This means that by measuring the emitted Cherenkov light and reconstructing the geometry of the air shower it is possible to determine the properties of the primary particle or photon, including its energy and direction of origin.
In case of a photon induced air shower the primary high energy photon produces an electron-positron pair in the electric field of an atom of the atmosphere. While these two new charged particles travel through the atmosphere they produce Cherenkov photons, but also lose their energy by radiating bremsstrahlung. These new created bremsstrahlung-photons can produce new electron-positron pairs, but with less energy than the first created pair. This process cascades to a whole shower of electrons. For each iteration the energy of electron-positron pairs is decreased. While their energy is changing with each iteration, so are the cross-sections

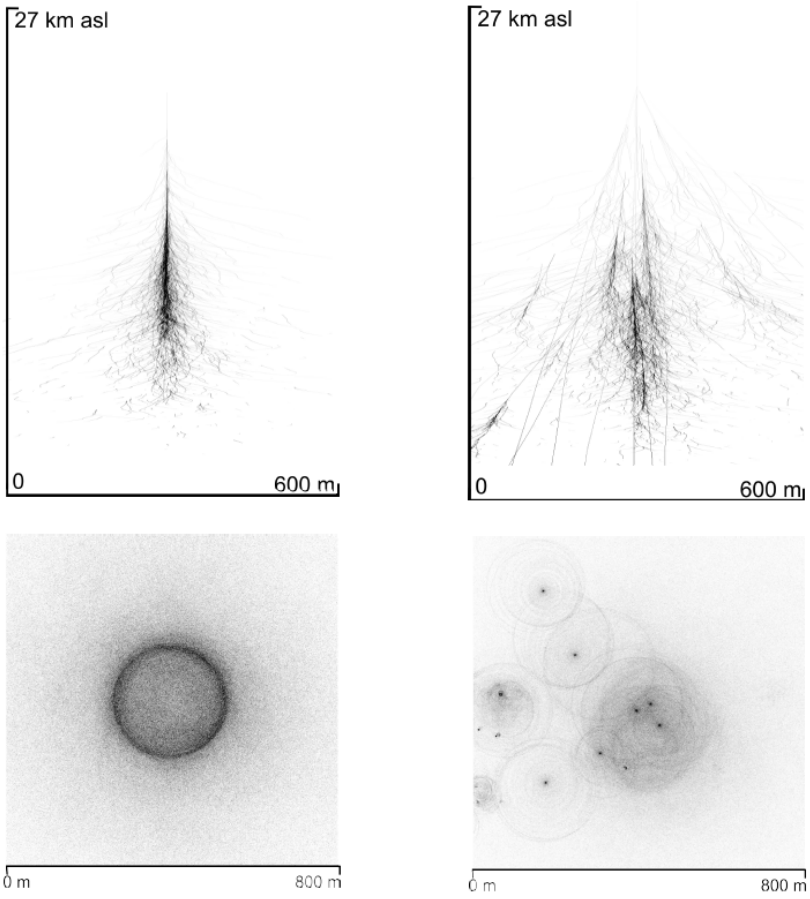

Figure 2.2: Monte Carlo Simulations of development of a particle air shower (top) and the resulting light distribution on the ground (bottom) for a 300 GeV photon (left) and an 1 TeV proton (right). (Taken from [16], originally from [1])

for the different interactions with the atmosphere too (see Figure 1.3). For a critical energy the cross-section for pair production decreased to the same order as Compton scattering and photoelectric absorption, and the cascade eventually reaches its maximum. From here on the energy losses are dominated by ionization and the cascade starts ceasing. How many iterations of electron-positron pairs there can be before that happens depends on the energy of primary particle. Hence, the amount of produced Cherenkov photons is determined by the energy of the primary particle. Also see [13]. In a hadron induced air shower the cascade is much more complicated because of its different branches. However, the principle is the same as for photon induced air showers and the amount of produced Cherenkov photons is determined by the energy of the primary particle, too.

An air shower caused by a high energy photon reaches its maximum around 10 km above see level. On the ground the Cherenkov light is spread over a circular area with a radius of around 120 m. For a 1 TeV primary photon this makes a flux of 100 Cherenkov photons per m^2. Also, because during the visible state all the particles in the air shower move with velocities higher than the phase velocity of light in the atmosphere, all the Cherenkov light is emitted during just a few nanoseconds [4].Therefore, large collection areas are required to have good statistics.

2.2 Stereoscopic Observations

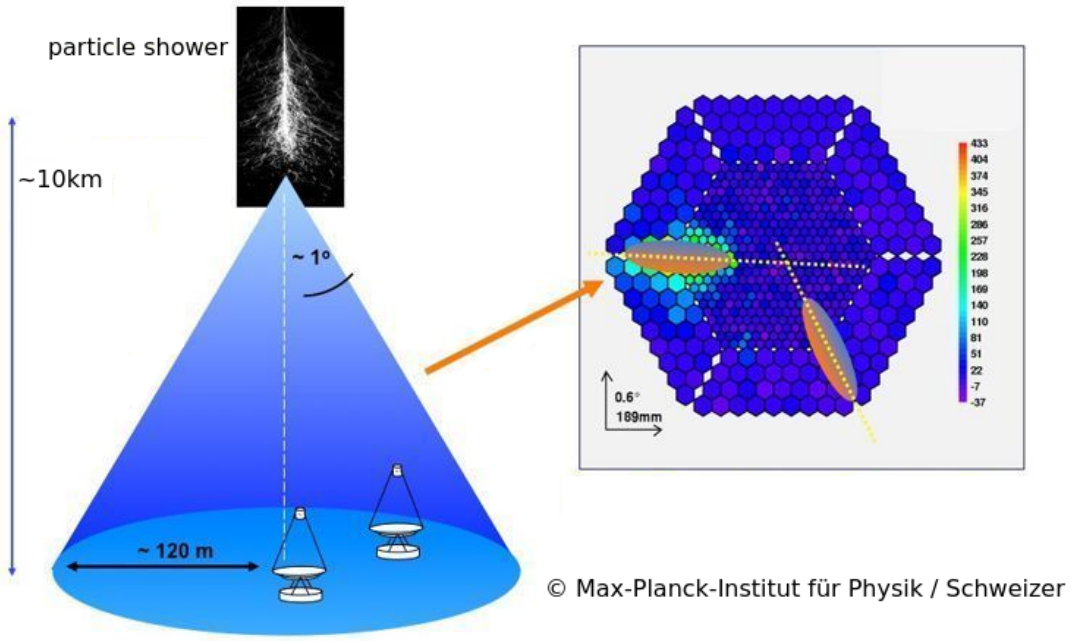

Figure 2.3: Schematic of an stereoscopic observation of an air shower with an array of two telescopes. The intersections of the long axis of the elliptical image of each telescope gives the position of the air shower.

An established observation method for air showers is the stereoscopic observation of the sky with two or more optical telescopes that can detect the Cherenkov light produced in the air showers. Such telescope arrays are called *Cherenkov telescope arrays*. Figure 2.3 illustrates the operating principle. All telescopes see the Cherenkov light produced in an air shower from different directions. Each telescope produces an elliptical image of the shower. The center of the air shower is located on the ellipses extended longer axis. Because several telescopes each deliver an image of the same shower, the reconstruction works with sufficient precision. The use of several telescopes is also increasing the total collection area.
There are three Cherenkov telescope arrays currently operating: H.E.S.S.(II) [7] [8], MAGIC[12] and Veritas[11]. MAGIC has two telescopes with 17m dishes, Veritas has 4 telescopes with 12 dishes and H.E.S.S. II has 4 telescopes with 12 m dishes and one with a 28 m dish. These arrays were developed and are operated by multinational groups consisting of institutes from different countries from all over the world [1]. In a new project, all the experience gained with these arrays is used to design and build one bigger and better array, simply called *Cherenkov Telescope Array*.

[1]For the full list of collaboration members see:
http://www.mpi-hd.mpg.de/hfm/HESS/pages/collaboration/institutions/
https://magic.mpp.mpg.de/backend/magic-team/cbmembers
http://veritas.sao.arizona.edu/collaborating-with-veritas-mainmenu-100/current-associate-members-mainmenu-102

2.3 CTA

The Cherenkov Telescope Array (CTA) project is an initiative of over 200 Institutes in 31 countries. The project is now in the prototyping phase. The first full telescope prototypes and prototype parts are either under construction or already built and used to study their performance. The major goals for CTA, compared to the current running arrays, are [3]:

- Improved sensitivity in 100 GeV too 10 TeV energy range with a factor of 5-10.
- Increased detection area of several km^2.
- Increased angular resolution of 0.2 degree to 0.02 degree for a better resolution of extended sources morphology.
- Extending the energy range well below 100 GeV and well above 10 TeV.

In an air shower the energy of the primary particle or photon causing it is converted into the kinetic energy of the shower particles and determines the amount of produced Cherenkov photons. So, to detect high energy particles and photons in the lower energy range, where less Cherenkov light is produced, telescopes with larger collection areas are required. The larger collection areas lead to a stronger measured signal, which can still fulfill the requirements for triggering. Primary particles or photons of the higher energy range lead to the production of more Cherenkov light. Therefore, only smaller collection areas are sufficient to measure a strong enough signal. But as Figure 1.1 shows, the flux of high energy cosmic particles decreases fast with increasing particle energy. And since the high energy photons are produced by these particles in the sources 1.2, they follow the same trend. To increase the amount of the observed very high energy events, a larger area on the ground can be covered by telescopes with small collection areas, just big enough to get a proper image of the shower.
There are two arrays planned. One for the northern and one for the southern hemisphere. The southern array will be able to observe most of the galactic plane in the full energy range. The northern array will see only a small part of galactic plane, but it has a good view on extragalactic objects. It will focus on the their observation in the lower energies. Therefore, it will consist of less telescopes. For the reasons stated above, the arrays will consist of a different number of different telescope sizes: 4 Large Size Telescopes (LST), 15 - 25 Medium Size Telescopes (MST), 36 – 70 Small Size Telescopes (SST, souther array only).

2.3.1 LST-Design

The LSTs have a 23 m diameter (approximately) parabolic dish with a focal length of 28 m. The telescope frame is made out of *Carbon Fiber Reinforced Plastic*. This makes it much lighter than a steel construction and easier to move. A disadvantage is that the carbon fiber reinforced plastic is not as stiff as steel, resulting e.g. in stronger dish deformations depending on the altitude angle. Therefor the LSTs will need an active alignment system to compensate these deformations.
The four LSTs are located at the center of the array and cover the energy range of 20-200 GeV. With their large collecting area LSTs can still detect enough Cherenkov photons for a sufficient high statistic and reaching the energy threshold for efficiently triggering events. The LSTs field of few will be 4-5 degree.

2.3.2 MST-Design

Around the LSTs the MSTs will be placed with a 100 m spacing. There are two designs of MSTs. One has a 12 m Davis-cotton dish and a focal length of 16 m. The Davis-cotton dish is spherical and is covered by 86 hexagonal spherical mirrors, arranged like a honeycomb and with two times the focal length of the dish. The second version has a dual mirror dish. The MSTs will cover the energy range from 0.1 to 10 TeV. This is the energy range of H.E.S.S., MAGIC and Veritas and thus well understood in terms of shower detection and reconstruction. Because of the increased amount of telescopes and increased array size, detected air showers will be uniformly sampled and there will always be a telescope in the optimal distance to the shower axis of 70-150 m. At this distance the flux fluctuations are small and the viewing angle is still big enough for an efficient reconstruction of the showers direction.

2.3.3 SST-Design

At the southern array the SSTs will be placed around the LSTs and MSTs to increase the array even further. There are three SST designs. Two of them are dual mirror telescopes. The third one has a 4m Davis-cotton dish with a focal length of 5.6 m. The SST cover the energy range from 10 TeV to more than 100 TeV. They are spread out wide, increasing the arrays area and thus the probability to detect air showers with very high energies.

2.4 Single mirror MST

Figure 2.4: Picture of the MST prototype in Berlin Adlershof, built and operated by DESY Zeuthen.

Figure 2.4 shows a picture of a single mirror MST prototype. It is located in Berlin Adlershof and built and operated by DESY Zeuthen, with contributions from other partners. At the time this thesis is written, the telescope dish is in redesign. Between the mirrors and the dish, there is a so called *triangle* with two actuators and a rotating bolt as interface to

the mirror. The triangle also is in redesign with the dish at the time this thesis is written. However, the triangular shape and its size are fixed. A picture of the "old" triangle with actuators and rotating bolt can be seen in Figure 2.5. The two actuators and the rotating bolt have a distance of 60 cm to each other. The rotating bolt is a bolt with a ball joint on each end. One end is connected to the triangle, the other end has a small round plate fixed to the ball joint. The actuators are also fixed to the triangle, but one can tilt in on direction. On their tip they also have a ball join with a small round plate attached to it. The small round plates are fixed to metal pads at the backside of a mirror. The pads are glued to the backside of the mirror with 60 cm distance from pad center to pad center. That one actuator can tilt, the ball joints and especially the rotating bolt make the mirror versatile enough to follow the movements of the actuators without suffering from mechanical stress.

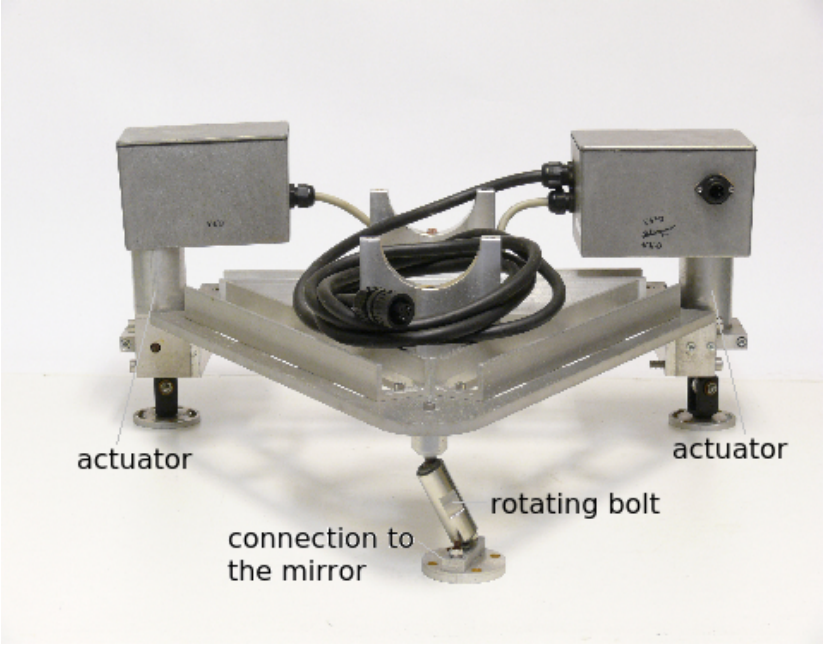

Figure 2.5: Picture of a whole mirror interface prototype with the steel triangle, two actuators and the rotating bolt in the front. The black and gray wires transport the signals and the power to the actuators.

2.5 Spherical Mirrors

For focusing light rays, that are parallel to the optical axis (*on-axis*), in the same spot, a parabolic mirror would have the perfect form. However, because of the varying curvature over the surface the production of such a mirror is either very costly or of low quality. In the case of spherical mirrors the circumstances are turned around . They are easier to produce, but their efficiency is limited by spherical aberration. As sketched in Figure 2.6 left, the profile of a spherical mirror is described by the following equation [10]:

$$R^2 = (x - R)^2 + y^2 \tag{2.1}$$

$$x = R \pm \sqrt{R^2 - y^2} \tag{2.2}$$

R is the radius of the sphere corresponding to the mirror curvature. The focus of a spherical mirror F is at $x_F = \frac{1}{2}R$. Equation 2.2 can be approximated with its binomial series:

$$x = \frac{y^2}{2R} + \frac{y^4}{2^2 2! R^3} + \frac{3y^6}{2^3 2! R^5} + ... \tag{2.3}$$

For a parabolic mirror all points on the mirror are described with [10]):

$$y^2 = 4Fx \tag{2.4}$$

$$x = \frac{y^2}{2R} \tag{2.5}$$

Now, the difference of a spherical mirror to a parabolic mirror is described by the difference of the x-coordinates of the points. Δx for a common y-coordinate is given as:

$$\Delta x = x_{circ} - x_{para} \tag{2.6}$$

$$\Delta x = \frac{y^4}{8R^3} + \frac{y^6}{16R^5} \tag{2.7}$$

Figure 2.6 right shows a plot of $\Delta x(y,R)$ for the three focal lengths of the CTA telescope mirrors (5.6m, 16m and 28m). Because of the small focal length the SST mirrors show the strongest deviation from a parabolic shape. But, with a diameter of 78 cm flat to flat they are also smaller than the other mirror types, resulting in a maximum Δx of less than 0.1 mm. The MST mirrors have a maximum value of 0.035 mm and the spherical LST mirrors of just 0.015 mm.

A light ray parallel to the optical axis, incident on a spherical mirror, pierces the focal plane

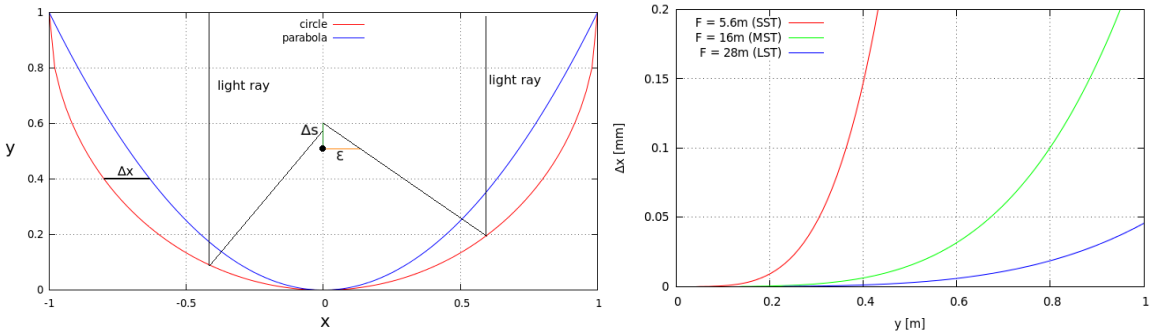

Figure 2.6: left: Comparison of the profiles a parabolic and a spherical mirror. For light rays incident close to the optical axis, the sphere is a good approximation for a parabola and the spherical aberration negligible. right: Dependency of the difference of a circles x coordinate to a parabola x coordinate on the y coordinate $\Delta x(y)$.

at a distance ϵ to the focus due to spherical aberration of (see Figure 2.6) [9]:

$$\Delta s = F \cdot (1 - \frac{1}{\sqrt{1 - (\frac{y}{2F})^2}}) \tag{2.8}$$

$$\epsilon = \Delta s \cdot \frac{y}{F} \tag{2.9}$$

For light ray incident on the edge of an LST mirror this makes an ϵ of about 0.06 mm, for an MST mirror 0.1 mm and for an SST mirror 0.25 mm. Thus, spherical aberration does no significantly increase the size of the spot for light rays parallel to the optical axis.

2.6 MST Camera

An air shower initiated by a high energy particle lasts around 5 ns [4]. This sets the time scale at which the cameras for Cherenkov telescopes have to be read out. For the MST two camera designs are in development, the NectarCAM and the FlashCam. The photon detection is done with modules of seven and twelve photomultiplier tubes (PMTs). The dead spaces between the PMTs are covered by custom designed Winston cones. They collect photons and direct them into the photomultiplier tubes. The Winston cones and the PMTs together give a hexagonal shape to the camera pixels. Each pixel has a diameter of 5 cm from one flat side to the opposing flat side. The main difference between the two MST camera designs is the electronics behind the photon detecting plane. The NectarCAM [4] is based on the NECTAr chip and stores measured events in an analog ring buffer. In the FlashCam [5] commercial FPGAs are used, the measured signals immediately digitalized and stored in a digital ring buffer in the FPGAs. The digital ring buffer does not produce any dead time for the camera during a read out.

2.7 Mirror Alignment: the function of the actuators

Independent of the telescope type and design, all the single mirrors mounted on the telescope dish have to function together as one large mirror. To do so, each mirror has to be aligned properly on the dish. When observing a point-like source, e.g. a star in the night sky, every mirror reflects the light of the star on the camera as a small spot. When the mirrors, attached to the triangle, are first mounted on the telescope, the procedure will leave the mirrors with a coarsely prealignment The actuators function as legs of the mirrors with adjustable length. By individually increasing or decreasing the length of the actuators, the pointing of the mirrors is changed. The actuators are controlled by the central telescope electronics. With the help of a specially developed algorithm all the reflected spots of the single mirrors can be automatically moved to the same spot on the camera. The quality of the alignment greatly influences the PSF of a telescope optics. The PSF , or minmal spot size, is a measure for how small structures can still be distinguished in an image and thus for the resolution, too. A Cherenkov telescope array is not directly observing an extended source like a supernova remnant, but the air showers induced by the high energy photons produced by it. The Cherenkov light produced in an air shower has an elliptical shape on the camera of a telescope (see Figure 2.3). When the alignment of the mirrors is bad, and thus the resolution, the shape of the ellipses can not be determined with high accuracy. This in turn means the direction of the longer symmetry axis can not be determined with high accuracy either and the reconstruction of the primary photons origin can only be done with a higher uncertainty. Additionally, the measured Cherenkov photons are spread over more pixel, resulting in lower signal per pixel and worse signal to noise ratio. Furthermore, this makes it more difficult to distinguish between photon and proton induced air showers, due to the increased later extension of both types in the camera images. Furthermore, the alignment of the mirrors influences the quality of the definition of the optical axis of the telescope and measure the pointing of the telescope. When a star of known position in the sky is observed, its image on the telescope camera is a spot of a size depending on the how accurate the telescopes optical axis is pointing at the star. Thus the minimal size of the spot determines the accuracy with which sources can be located.
The Quality of the mirror alignment is mainly determined by the precision of the actuators and by how big steps their length, and thus the pointing of the mirrors, can be changed.

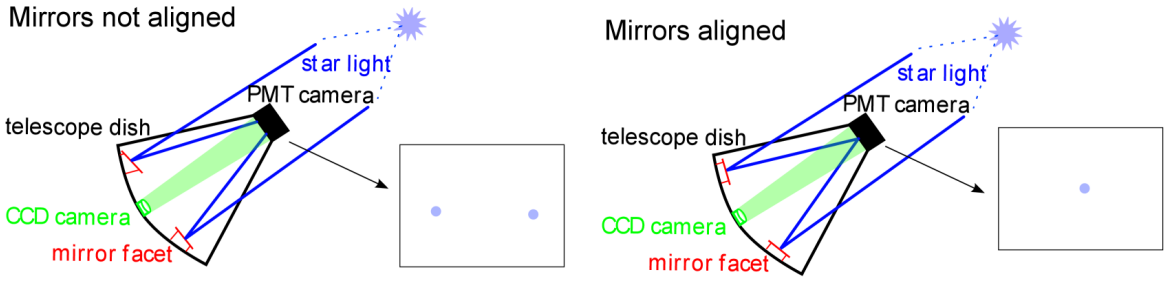

Figure 2.7: A star is observed with a single mirror telescope and the starlight is reflected as a round spot on the (PMT) camera by each mirror facet. When the mirrors are not aligned (left) several light spots can be seen on the camera. For a good alignment (right) all mirror facets reflect the starlight into the same point on the camera. (Source: [16])

2.8 Mirrors of the Single Mirror Telescopes

The mirrors of the single mirror telescopes are mounted on Davis-cotton dishes and thus are spherical too. For each single mirror telescope size there are different types of spherical mirrors in development. They are all hexagonal and have different sizes, usually described by the distance of two flat sides (flat to flat). SST mirrors have a diameter of 78 cm flat to flat, MST mirrors 120 cm and LST mirrors 151 cm. Because of the difference in size of their corresponding telescopes, all three mirror types have different requirements on their final weight and the stability of their material. E.g. a thin glass mirrors in the size for an MST or LST would bend or even break under its own weight, while a thick and massive mirror would be difficult to handle for the actuators (see Chatper 3). Therefore, different production processes and materials for the mirrors are tested. Most of production processes can be roughly described as follows [6]:
A glass layer is bended with vacuum over a mould (cold slumping). The mould has the negative form the mirror shall have (spherical curvature). Afterward the glass sheet is glued on a light body, e.g. an aluminum honeycomb structure. On the backside of light body another not slumped glass sheet can be glued. Then the curved glass layer is front-coated.

2.9 Mirror Coating

The Cherenkov light produced in air showers is optical light. This light needs to be collected as efficiently as possible. The array's efficiency in collecting Cherenkov photons depends on there factors. The first one is the quantum efficiency of the camera with all its components. The second is the area on the ground covered by the array or, for the lower energies, of the telescope dishes. The area covered can be increased either by increasing the amount of telescopes or by increasing the sizes of the telescope dishes. Increasing the number of telescopes is very costly and increasing the dish size is technically not easy, since larger dishes tend to deform stronger under their own wight and wind. Especially for the LST this would be difficult and these telescopes are already at the limits of a meaningful size. The third factor for the efficiency in collecting Cherenkov photons is the reflectivity of the mirrors. It needs to be as high as possible in the wavelengths of the Cherenkov light, but there are other important aspects, too. Figure 2.8 shows the simulated spectrum of Cherenkov photons produced in an air shower and the measured night sky background on La Palma. A background can be produced by nearby cities and other places with artificial light sources like street lights, but is always present due to light of the stars and the moon. To not collect photons that were not

produced in an observed air shower, the requirement for the reflectivity of the mirrors is to be at least as good as 85% between 300 nm and 550 nm. This indirectly excludes the part of Cherenkov photons with wavelengths bigger than 550 nm, but it also a lot of the background. However, the discussion is still ongoing if excluding all light with wavelengths above 550 nm, e.g. with special (dielectric) mirrors coatings, would be for the better or not.

The reflecting layer of the mirrors require a special coating to have such a high reflec-

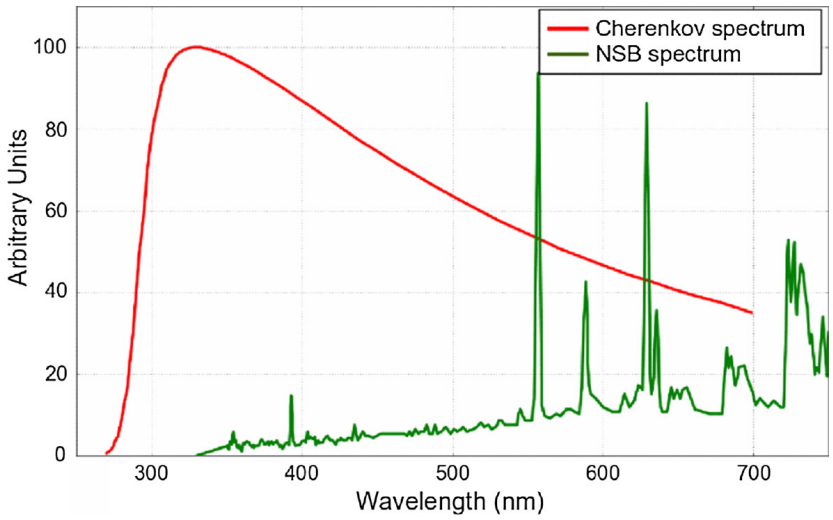

Figure 2.8: Simulated spectrum of the Cherenkov light arriving on the ground and the night sky background in arbitrary units, measured on La Palma. Most of the Cherenkov light is emitted in the range of 300 to 550 nm, while the night sky background is weak in this range. (Source: [6])

tivity over a 250 nm wavelength range. For the CTA different coatings are tested [6]. As reflecting material usually a layer of aluminum is used for its high reflectivity in the desired wavelength range. To protect the aluminum from deterioration different protection coatings are deposited on top of it. This can either be a classical coating of SO_2 or a 3-layer coating of SO_2+HfO_2+SO_2. A third option is a dielectric coating consisting of a stack of many alternating layers of two materials with different refractive indices, e.g. SiO_2+TiO_2. With a dielectric coating it is possible to produce a cutoff in reflectivity at 550 nm, reducing the effect of the night sky background.

2.10 MST Actuator Design

The concept of the triangle, actuators and rotating bolt as interface between mirrors and dish and as alignment tool as described in chapter 2.7 was originally developed by the MPIK Heidelberg for the H.E.S.S.II telescopes and has been adapted for the CTA. From there it was imported and adapted for the CTA telescopes. The IAAT took the task to develop an improved actuator design. The concept for the development was to trade some not necessarily needed accuracy in the mirror pointing against a decrease in the costs, weight and complexity, which means an easier assembly. Also, the H.E.S.S.II actuators are known to have a few weak points, e.g. a too weak spindle threat. To remove them was another goal. Figure 2.9 shows the mechanics and the components of first version of the redesigned actuator, that was the subject of the tests described in this thesis. Not seen is the 12V DC motor GMPD 404.905 from Valeo. It has a Hall sensor included that counts half rotations. All actuator movements are measured in *steps*, with one step referring to one count of the motor's Hall sensor. The

motor drives the spindle (left, red). On the spindle there is an iglidur nut and on top of the nut there is a cylindrical stroke unit (grey with little blue). When the spindle is driven, the nut is moved and carries the stroke unit in and out of the actuator. All other parts are either guiding the stroke unit or are part of the outer hull, preventing the environment to affect or damage the mechanics.

Compared to the design used for H.E.S.S., all the parts of the new actuator, designed by

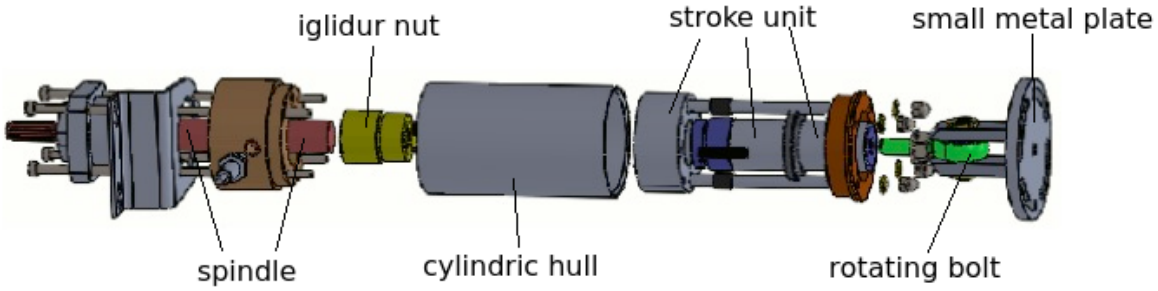

Figure 2.9: Drawing of the actuator parts. Left in red the spindle, in yellow the iglidur nut and on the right in gray with some blue on the left side is the stroke unit.

Buck Engineering, have higher tolerances for their production. This means reduced costs, but also reduced precision. Iglidur is a special material, ensuring a low-friction gliding of the nut on the steel spindle without the need of lubrication. The spindle now has a trapezoidal thread instead of triangular one. This thread is more durable to mechanical stress. Figure 2.10 shows an assembled actuator prototype. The lower box contains the motor and the control electronics. On one side the box has a metal membrane. While it is impenetrable for water, gas and steam can pass through it. This ensures pressure compensation between the inside and outside of the box. Small amounts of water that might get into the box can slowly vaporize and then leave through the membrane. The H.E.S.S.I actuators have a membrane made of synthetic material. Some insects in Namibia like to use the actuator boxes as nesting place and eat their way through the membrane. Using a metal version solves this problem, as proven with the model used for H.E.S.S. CT5.

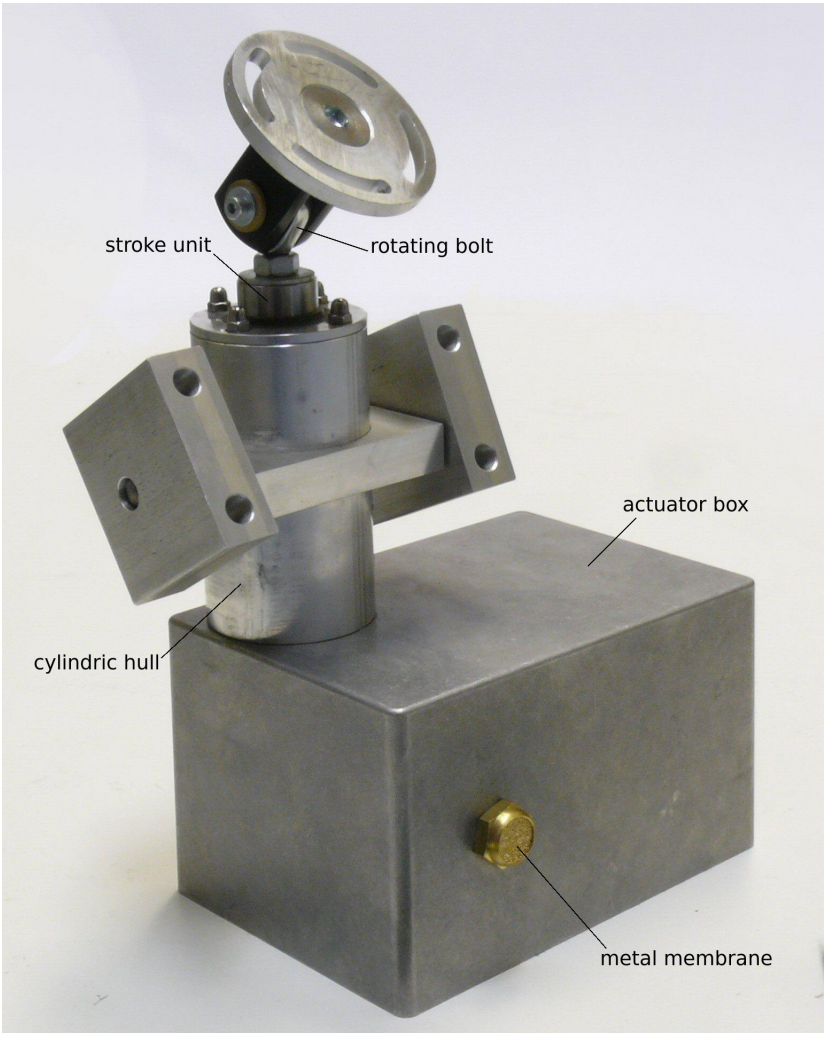

Figure 2.10: Picture of an assembled actuator.

Chapter 3

MST Actuator Testing

The IAAT actuators for single mirror MST designed by Buck Engineering have the important function to set and change the pointing of each individual mirror. To ensure a proper alignment and thus a good telescope performance, the actuators have to be fully functional under certain requirements. In this chapter these requirements are discussed and the actuator tested on their performance in different conditions.

3.1 Requirements on the actuators

At the time this thesis is written it is not yet known where the CTA sites will be located. But since there are not so many suitable places with e.g. enough nights with clear sky and not too much stray light from nearby cities, the list is limited. This means the telescopes and all its parts have to work under still not fully known conditions. However, there are a lot of constraints on what the telescopes have to endure. This leads to the requirements for the telescopes (MST) to be operational for (D203.5: MST Requirements):

- Air temperatures from -15 to +25 °C
- Air temperature gradient during night time ±7.5 °C/h
- Humidity in the range of 2 – 90%
- Wind speeds averaged over 10 minutes of <36 km/h

In addition all telescope parts must be resistant against UV light, 29×10^3 dust and sand particles of 5 μm in 1 m^3, as well as concentrations of NO, NO_2 and SO_2 < 30 ppb. Under bad conditions like storms, the telescopes do not have to be able to perform observations. But in case of emergencies, e.g. fast changes in weather, the telescopes have to be able to be moved into a save position to prevent damage. For this the single telescope parts do not have to work at full speed. In the save position the telescope also have to survive extremest conditions. These are specified as (CTA Ref : MAN-PO/120807):

- Temperatures from -20 to +40 °C (air temperature)
- Max. temperature gradient withing 24h ±30 °C
- Humidity in the range of 2 – 100%
- Wind gusts (1s duration) of 200 km/h or <120 km/h averaged over 10 minutes

- Maximum rainfall of 200 mm in 24 h and 70 mm in one hour, wind speed blowing rain of 90 km/h
- Impacts of 20 mm diameter hailstones with 1J kinetic energy
- Snow accumulation on the ground of <50cm
- Ice with a thickness of <20 mm on all surfaces
- Max. solar radiation of 1200 W/m^2
- Seismic activities: up to 0.26 g horizontal and 0.3 g vertical ground acceleration (South America, location depended)

Two actuators (and the rotating bolt) support one whole mirror. At the time this thesis is written it is not yet decided which and how many of the different types of MST mirrors will be finally used. In addition to a mirror's weight, wind with speeds as stated above can cause non static forces that must not influence the actuators functionality during observations. Ice, storms and earthquakes can push pull and shake the mirrors, increasing the maximal applying forces. To approximate the forces applied to an actuator a mirror weight of 40 kg is assumed. An ice[1] layer of the 20 mm on the mirror surface (2.5 m^2 for front side plus back side) has a weight about 50 kg. The forces caused by an earthquakes can be amplified in case of a resonance with the telescope structure. Thus, the maximum acceleration of 5 g results from simulations. A wind force F_w can be calculated as:

$$F_w = c_w \cdot \rho \cdot v^2 \cdot A \tag{3.1}$$

Here, ρ is the density of air of 1.4 kg/m^3 for about -20 °C, v the speed of a wind gust of 200 km/h and A the effective area in the wind direction, assumed as 10% of the mirror surface for wind blowing onto the side of the mirror. c_w is the drag coefficient with an assumed value of 2. This makes an F_w of 540.1 N applied on a mirror by the wind gust onto the side of the mirror.
In horizontal direction, the weight of the mirror with ice is shared between the two actuators. The wind forces can be assumed to only apply in horizontal direction, but because one actuator is tiltable in this direction, the whole force has to be endured by one actuator alone. Earthquakes produce forces in horizontal as well in vertical direction. The exact force the mirrors and the interface has to endure depends on the their position on the dish and also the elevation angle of the telescope. For a worst case scenario, it can be assumed, that one mirror's optical axis is parallel to the ground. Then, the mirror and the interface have to endure the whole maximal horizontal force of the wind guts and the earthquakes of 4955 N plus the vertical weight force of the mirror of 883 N. Both are parallel to the mirror surface but with a 90° angle to each other. Since one actuator can tilt in horizontal direction, the other actuator has be able to handle all the horizontal force alone. Thus, this actuator has to endure a force of $\sqrt{4955^2 + (883/2)^2} = 4972$ N or 507 kg, respectively. This force is applied perpendicular to the stroke units moving direction, referred to as *transversal direction*. Along the stroke units moving direction, referred to as *longitudinal direction*, the wind force can be 10 times as high as calculated before, due to the increased effective area. All forces in longitudinal direction are shared between both actuators of a mirror. Thus the maximum force that one actuator has to endure in longitudinal direction is 491 N or 500 kg, respectively. This numbers seem to be large, but these forces only applied for short times, like one second for a wind gust, and are worst case scenarios.

[1] 900 kg/m^2

During operation, the actuators do not have to endure earthquakes, storms or the additional weight of ice layers on the mirror. Only wind with speeds up to 36 km/h is required to be endured in addition to the mirror weight. Therefore, the maximum forces an actuator has to endure and still operate with sufficient precision is a third of the mirrors weight force of 131 N or 13.3 kg in longitudinal direction, for the mirror pointing upwards into the sky, and 201 N or 20.5 kg in transversal direction, for the mirror's optical axis parallel to the ground.
Besides the requirements stated above, there are additional with no certain specification. They will be discussed in the chapter below. When the mirrors together with the triangle and actuators are mounted on the telescopes, they might need a *prealignement* during which they are roughly pointed on telescope camera. For this the actuators have to have some clearance in the way they are fixed to the triangle.

3.2 Actuator precision and step width

The requirements listed above only state under what condition the actuators have to work and must not be damaged. With what precision they have to work is still a matter of discussions as this thesis is written. The actuators are part of the interface between the dish and the mirrors. They have the be able to change the pointing of each mirror far enough to point them onto the middle of the telescope camera. How far the mirrors have to be moved during the alignment process is not yet known or specified. A defect mirror is reducing the resolution of the telescopes images and therefore should not contribute to it. If the actuators shall be able to point a defect mirror away from the telescope camera is not specified either. For this purpose manually moving the actuators or triangles could be an alternative addition to a limited motorized actuator range. Since the dish and the triangle are in redesign these open questions can not be answered in time for this thesis. However, the precision of the final alignment will be a matter of the precision of the actuators.
During the alignment all the single reflected spots, one for each mirror, are moved to the same spot on the camera to produce one cumulated spot. The size of the pixel of the camera determines the size of two spots that can still be distinguished. Therefore, a good alignment is characterized by producing a cumulated spot with a size that is smaller than the size of a pixel of the camera. For MSTs there are two camera types in development (see Chapter 2.6). Both are using photomultiplier tubes and have a common pixel size of 5 cm. The cumulated spot is dominated by the largest spots reflected from the mirrors positioned at the outer part of the dish. When observing a star in the nigh sky, its emitted light rays can be assumed to arrive parallel on the mirrors. The spherical dish is so large that the rays hit the outer mirrors under an angle of 22°. Thus, the reflected spots of these mirrors are larger due to spherical aberration. For off-axis events - the telescope is not directly pointed at the air shower – this effect is even larger.
The precision of the mirror alignment is limited by how precise the length of the actuators can be set. And this is determined by the step width of the actuators. To calculate an uncertainty in the actuators length into an uncertainty of the mirror pointing angle a situation as in Figure 3.1 left was assumed: Both actuators stay parallel to each other, keep their distance of 60 cm, the rotating bolt plays no role and small increases in the mirrors length are possible. For the angle φ, corresponding to the actuators step width, the following formulas can be derived:

$$\varphi = \arctan(\frac{x+y}{d}) - \arctan(\frac{y}{d}) \tag{3.2}$$

$$\varphi = \arctan(\frac{x + tan(\alpha) \cdot d}{d}) - \alpha \tag{3.3}$$

d = 30 cm for half the distance between two actuators, y is half the difference of the two

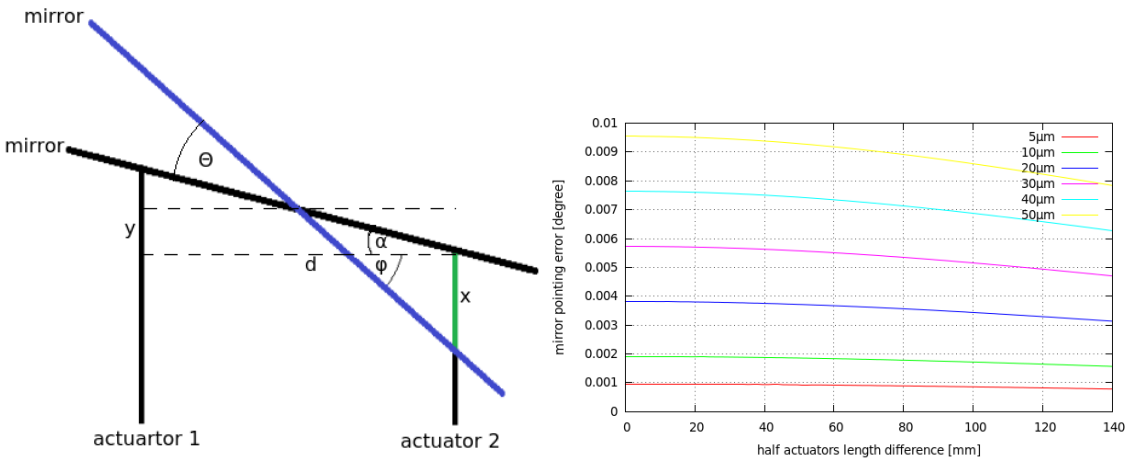

Figure 3.1: left: Sketch for calculating the uncertainty in the mirror pointing from the actuator step width. right: Plot of equation 3.2.

actuators lengths and x is the step width. Figure 3.1 right shows the plots of these equations for different actuator step widths. The maximum is seen for both actuators having the same length. Therefore actuators of the same length were assumed for further calculations and equation and become:

$$\varphi = \arctan(\frac{x}{d}) \tag{3.4}$$

For an assembly of mirrors the distances (or errors) of the single light spots reflected by the mirrors to a random spot on the camera after a full alignment follow a distribution given by the prealignment. Depending on how the prealignment will be done, the distribution is either uniform or a wide Gaussian. A wide Gaussian with a FWHM of the order of degrees restricted on a small interval of less then the order of 0.001 degree is only a little overestimated by a uniform distribution. To not underestimate any errors, the later one is assumed. To gain information on the impact of different actuator step widths on an MST, simulations were used. The simulations were done with the simulation program *sim_telarray* [2]. It is a version of the *sim_hessarray*, originally made for H.E.S.S., but with updated files and lists for CTA telescopes. The program simulates a shower of photons directed towards the telescope. From the output file of the simulation program *sim_telarray* which, among other informations, contains the coordinates in the focal plane of all the simulated photons that were reflected onto the camera by the aligned telescope mirrors. The coordinates are given as distances to the camera planes center in cm. To determine the size and quality of the accumulated light spot on the camera a *PSF* was calculated. *PSF* stands for *point spread function* and has different definitions. Here the *R80* was used. It is the Radius of a circle around the center of mass of the light spot, which contains 80% of the photons arriving on the camera plane. Some more information can be found in the PSF section of the second part of this thesis.
For simulating an MST dish, a mirror list with 84 hexagonal mirrors (120 cm diameter flat to flat) called *mirror_CTA-100_1.20-84-0.02.dat* was used. It had been already included in the simulation package together with a bash script to launch a simulation. For doing multiple simulations with different telescope parameters and extracting the desired informations and calculating the PSF, different python programs have been written. All parameters that needed to be changed are located in the file *hess2_dish.cfg* or could be changed within the

[2] http://www.mpi-hd.mpg.de/hfm/ bernlohr/index.html

bash script. The parameters for focal length of the mirrors, the focal length the dish and the position of the camera were set to 16 m. All parameters for offsets or errors in the telescope pointing have been set to zero. Since at the time this thesis is written no information on the performance of the MST dish were available, all parameters for errors in the dish quality were set to zero too. To assume perfect mirrors, all parameters representing the errors in the mirror quality were set to zero too. In the simulation program it is possible to give values for the mirror pointing angle in horizontal and vertical direction. The mirror pointing error is assumed to be equal in both directions. The simulation needs the mirror pointing error in degree as input parameter (called *mirror_align_random_horizontal* or *..._vertical*) and originally uses it as standard deviation for a random Gauss distribution. Each mirror got assigned a random error following this Gaussian distribution. To better match the influence of the actuators, the simulations source file *sim_imagin.c* was changed to use the input parameter as borders for an interval of an uniform distribution which the errors of single mirrors pointing are following.
Now, two case were simulated. The first case was perfect mirrors, the second case was realistic mirrors. Figure 3.2 shows the results of the simulation. For the imperfect mirror simulations the parameter *mirror_reflection_random_angle* was set to 0.02984 degree, corresponding to a sixth of a cameras pixel size. With this parameter, every time a photon hits a mirror in the simulation, a random error is added to reflection angle of photon. The random errors follow a Gaussian distribution with the value of parameter as FWHM. The Value for this parameter was derived from the requirements on the CTA mirrors (see chaptor 4.1.1). All real mirrors will have a PSF bigger than a minimal value. This minimal value should not be a lot smaller than the maximal allowed value due to the always present production errors. This means there might be a lot mirrors simulated with an unrealistic good PSF, this might underestimate the desired quality for mirrors. However, there will also be some mirror which would not be accepted for mounting on the telescopes. This might balance out the too good mirrors. Nevertheless, the simulation result stays an approximation.

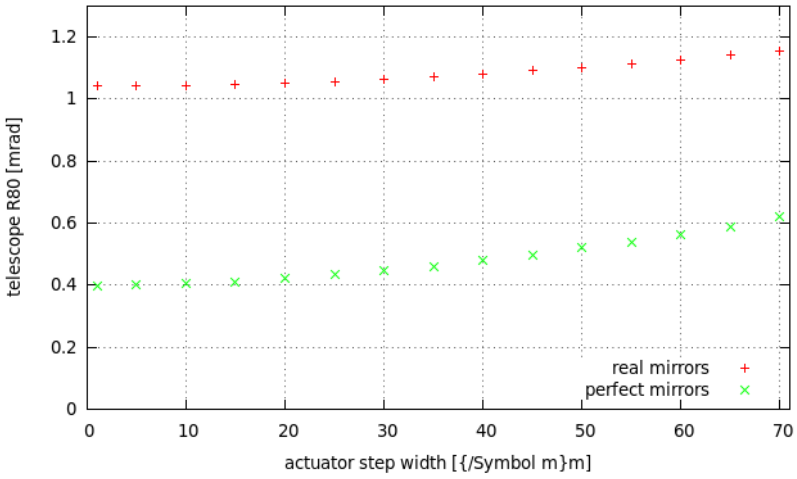

Figure 3.2: Simulated telescope PSF vs actuator step width for perfect and real mirrors.

A criterion on quality of the mirrors is to have a PSF (R80) smaller than a sixth the size of the camera's pixel (see chapter 4.1.1). A good measure for the PSF of a telescope (without dish deformations) is 2 times the maximal mirror PSF. This allows the Davis-cotton dish

design and the mirror interface, including the actuators, to produce around the same error as the mirrors. The PSF is often expressed as the opening angle of a triangle with one of it's corner on intersection of the optical axis of the telescope and the dish and the other two corners at opposite sides of the circle around the center of the camera representing the PSF (also see chapter 4.1.1). Here, 5 cm (diameter) correspond to an angle of 1.04 mrad. For 25μm actuator precision the telescopes PSF would still be below this value. A 30 μm precision might also still fulfill this criterion, because not the whole error bars lie above 1.04 mrad. However, aiming for 20 μm makes sure to stay below 1.04 mrad and gives a buffer for any unforeseen complications in the development or overestimating the mirror quality.
When the telescope is moved to different elevation angles than where the alignment was done, the telescopes dish will deform under its own weight. This leads to the mirrors not pointing on the same spot anymore and the PSF increases the further the telescope is moved out of the alignment position. This could be compensated by constantly changing the alignment depending on the elevation angle of the telescope. But driving the actuators more often increases the requirements on the actuator materials, which might results in higher production costs or the need to replace them more frequently. Two other factors increasing the telescope PSF are the finite distance at which the Cherenkov light is produced and that most of the air showers will be observed with an offset angle to the telescopes optical axis. The latter one is a geometrical effect that can't be prevented and dominates over the actuators influence. To properly do analyses with real air showers, atmospheric models and shower modeling with monte-carlo simulations are needed to be taken into account. This however, would go far beyond the scope of this thesis.

3.3 Actuator Testing

The spindles thread of the actuator design by Book Engineering has a steepness of 2 mm/turn. For one turn the motor counts 420 steps. This gives a step width of 4.762 μm. A spindle with such a thread was chosen for mechanical reasons. When the actuator is burdened with the weight of a mirror, the spindle shall not just slide into the direction the weight is pulling or pushing. To hold its position, it needs enough friction forces between the spindles thread and its counterpart. This is realized by a smaller steepness of thread and thus an angle between the threat moving direction and the direction of the forces closer to 90 degree. On the other hand, the actuator shall work smoothly for 30 years. Therefore friction forces should be kept as small as possible to prevent unnecessary deterioration. Additionally, strong forces perpendicular to the thin threads could damage them over time or during extreme conditions like earthquakes or storms. For the thread a strong trapezoidal shape was chosen to decrease the chance for this to happen. But it is also necessary to keep the angle between the thread and the forces different from 90 degree as much as possible. This is realized by an increased steepness of the spindle. The trade-off of this effects leads to the used spindle with its given steepness, which is self-holding, but should not cause unnecessary stress on the material.
In addition to the spindle thread steepness the precision of the actuators is also influenced by a lot of other factors like clearances, softness and assembly of all the single parts. To evaluate the actuator performance and locate potential weak points, tests under specific condition like weight loads, temperature and direction of forces were done.

3.3.1 Longitudinal precision and linearity of the movement

The actuators carry out a simple movement: stroke unit in and out. The position of the stroke unit is measured in counts of the motor's Hall sensor. One count or *step* corresponds

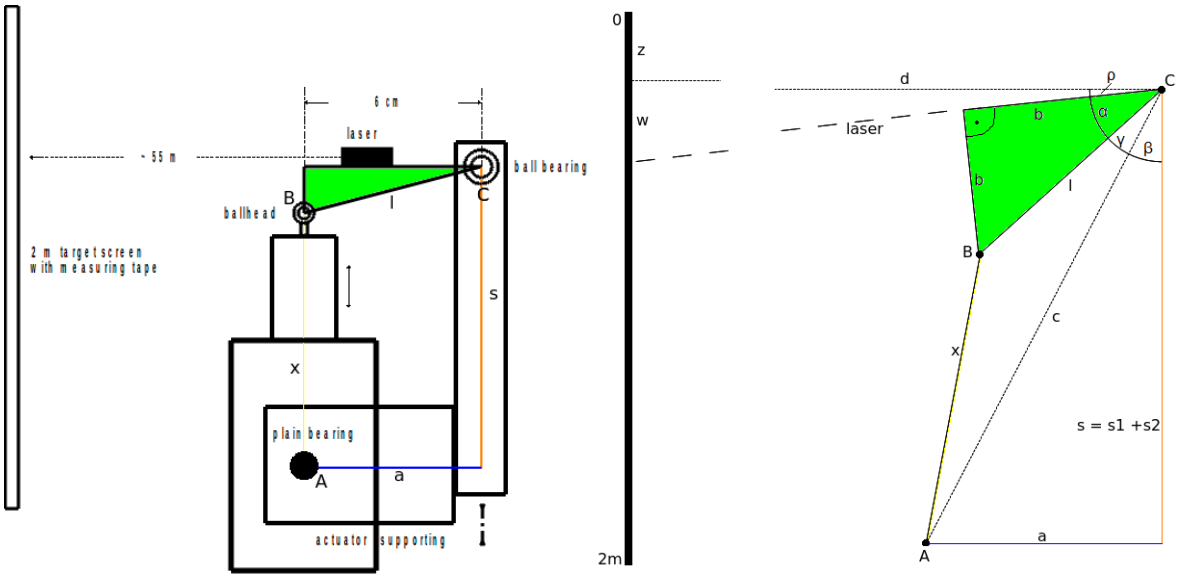

Figure 3.3: left: Sketch of the experimental setup to measure the step width of an actuator for different weight loads.
right: Sketch of the geometry used for calculating the actuator step width. A, B and C indicate the position of rotation axes.

to half a turn of the motor. How far the stroke unit is moved in or out of the actuator for each step should neither depend on the stroke units position nor on the weight load the actuator has to handle. As sketched in Figure 3.3 left the linearity of the actuator was checked. Two photos of the setup can be found in the appendix. The actuator was fixed in a special device in the same way it is supposed to be on a MST, just able to rotate around the marked point A. On one side a metal bar, directing upwards, is mounted on a rail. The bar can also be fixed immobile. Another metal device holding a point laser is connected via a ball bearing to the first one and directly connected to the ball head on top of the actuator. Around 55 meters in front of the laser, a vertical target screen with a scale is located. When the actuator stroke unit is moved up or down, it changes the angle in which the laser is pointing towards the screen. From the distance of the laser to the wall and the length of the path the laser spot moves on the target screen, a triangle is defined from which the change of angle of the laser pointing direction can be derived. Since the geometry of the rest of the device is known too, the length which the actuator stroke unit is moved can be calculated. The precision of the measurement is given by how good the change of the laser's angle ρ and the geometry can be determined. Measuring the geometry of the setup turned out to be a more difficult task than originally expected, because a very high precision of these values are needed. However, the big distance from the actuator to the screen of 55.5 m makes it easy to determine the angle with high precision. Figure 3.3 right shows another sketch of the setup with more details of the geometry that was used for calculations. The line x does only represent a part of the actuator, but since the change of the actuators length with each step is given by the difference of two actuator settings, meaning the difference of two measured x, absolute values for the length of the whole actuator are not needed. For the line segment x_i of one actuator setting the following formulas can be derived:

$$\frac{\pi}{2} = \rho + \alpha + \gamma + \beta \tag{3.5}$$

$$x_i = \sqrt{c^2 + l^2 - 2 \cdot l \cdot c \cdot \cos(\arctan(\frac{z-v}{d}) - \alpha - \beta + \frac{\pi}{2})} \tag{3.6}$$

$$\Delta x = x_2 - x_1 \tag{3.7}$$

z is the value at which the laser hits the scale on the wall perpendicular and v the value for an actuator position.

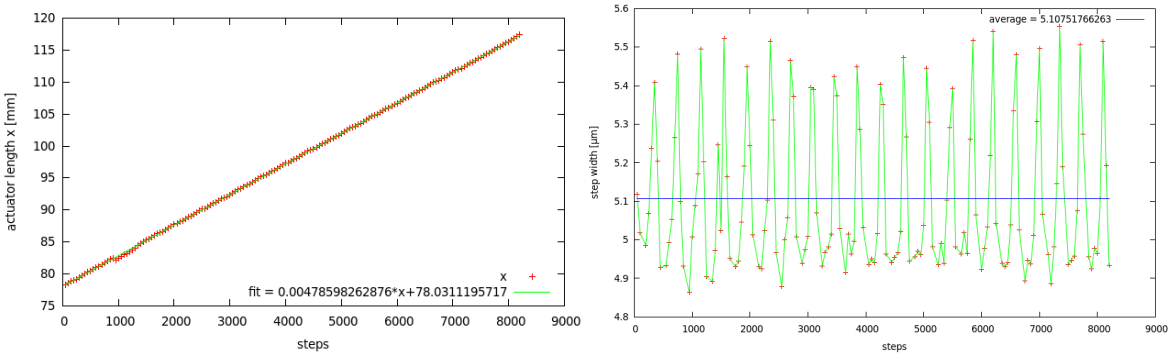

Figure 3.4: An example of results of the longitudinal precision and linearity tests for 30kg weight load pressing on the actuator and moving the stroke unit inwards.
left: Calculated actuator partial lengths x vs the position of the stroke unit in steps. The green line is a linear fit to these values, done with method of the least χ^2. The steepness of the fit is the measured step width in μm.right: Step width Δx between two neighboring data points divided by their difference in position (about 50 steps). Plotted vs the position of the larger data point. The blue line shows the average of single step widths.

As first part of the tests, the actuator was moved stepwise completely through the available range with weight loads of 10 kg and 30 kg pressing on it. Figure 3.4 exemplarily shows the result for 30 kg and moving inwards. The analyses of the measurement data was done in two ways. The first way was to calculate the length of x (Figure 3.4 left) and do a linear fit to the values. For the fitting the method of the least χ^2 was used. The steepness of the linear function corresponds to the step width of the actuator. The error bars are to small to be seen and therefore not plotted. The second way is to calculate Δx between two neighboring measured values and divide it by the amount of steps the actuator was driven (about 50 steps). Afterwards the average Δx was calculated. This value also corresponds to the actuator step width. Here, the error bars were not plotted for better visibility. The lines connecting the single values were plotted to better show the order in which the values were measured. The spread of the values look periodical. The reason for this might be uncertainties in the geometry which were thought to be negligible small and therefore not taken into account. All parts of the test setup have been produced with high precision. But small errors in the production or assembly of the parts, e.g. a square angles slightly differing from 90 degree, can have an impact on the measured values. Since the geometry consist of only triangles, a periodical increasing and decreasing of the error, and thus the measured value, is not surprising. This might also be related to the fact, that the connection of spindle to motor was not optimal adjusted for all prototypes actuators, leading to

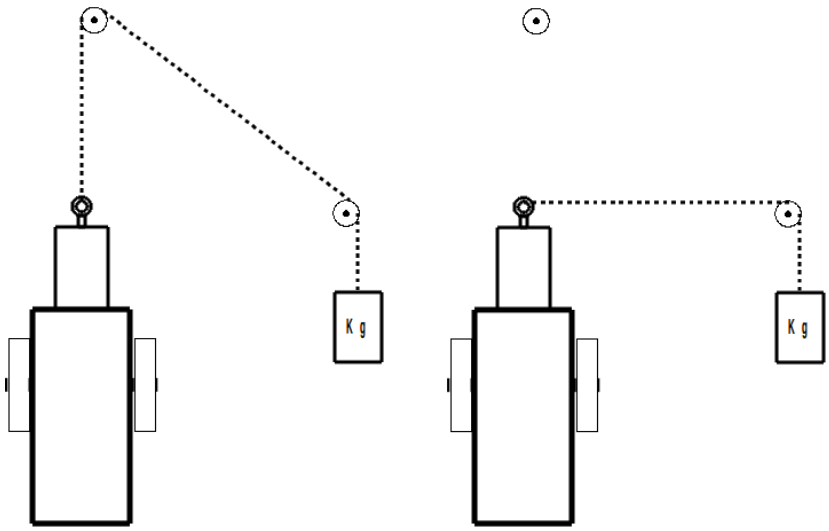

Figure 3.5: Sketches of how weight was applied to the actuator in longitudinal pull direction (left) and vertical direction (right).

The same test was repeated with weight loads pulling on the actuator in longitudinal (upward) as well as in transversal (sidewards) direction. See Figure 3.5 for a sketch. The weights were applied by a rope and a system of pulleys. Figure 3.6 shows the results for moving outwards with 30 kg transversal load.

Most results for the step width were a little higher than the expected value of 4.76 μm,

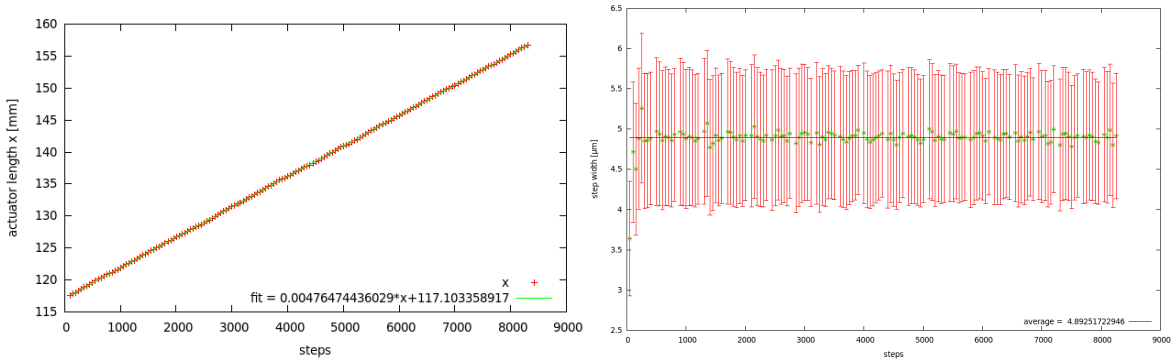

Figure 3.6: Both plots show the same as Figure 3.4, but for 30 kg weight load pulling vertical direction.

given by the steepness of the spindle. The error bars of the plot in Figure 3.6 right have a size of around ±30%. The standard deviation of the mean values of around up to 0.2 μm or about 3.9% do not always included the expected value and the averaged step width (method 2) values always are larger than the expected value. The maximum difference between a measured (average) step width (method 2) and the expected value was about 0.35 μm. This measurement setup has 9 different parameters. The errors of all of them are generously approximated. The big difference between the size of the calculated error bars and maximum difference between a measured (average) step width indicates that some of single error of the parameters might be overestimated. The offset of all the measured values to the expected value might be caused by overestimating the line segment s in Figure 3.3 right. As part of the

measurement process it was needed to be changed often and has been repeatedly measured. Measuring s with a caliper gauge is not an easy task and overestimating it by accident seems to be much more likely than underestimating.
The error bars as seen in Figure 3.6 representing the (overestimated) uncertainty in the actuators length are more than two times smaller than the desired 20 μm and the variance of the measured values is very small. For the different used weight loads an offset of up to 3.9% is seen, but it is most likely caused by the measurement process. Therefore, in the moving direction of the stroke unit the behavior of the actuator is sufficiently linear, independent of the direction and magnitude of the forces it was designed for.

3.3.2 Transversal precision

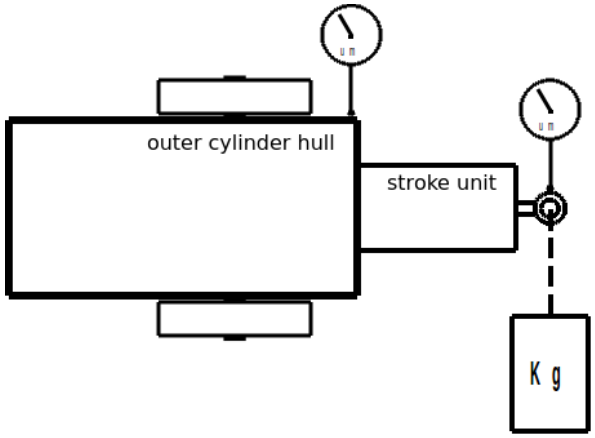

Figure 3.7: Sketch of how the transversal precision of the actuator was tested.

The mirror pointing can be mathematically described as a function depending on the effective lengths of the legs carrying it. It is an effective length because even if the leg lengths are fixed but their form is unstable, e.g. they are made out of gum, the mirror wight would compress and bend the legs, resulting in a very different pointing. The actuators are made out of steel and (hardened) aluminum, what seems not be comparable to gum. But demanding a high precision for the mirror pointing means also demanding high precision of the actuators effective length. Too much play or to soft and to thin material can result in a bending or a tilting of some parts. A small bending or tilting, which are always present, only produce an unsignificantly smaller change of the effective length. However, it still needs to be proven, that any bending or tilting is not increasing the actuators precision over the desired value of 20 μm. If a part of the actuator is bending or tilting or even both can not easily be distinguished. Therefore, all this possibilities will be collectively addressed as bending.
Figure 3.7 shows how the actuator was tested for bending and tilting. The actuator was fixed on a table with a granite tabletop. For different positions of the stroke unit, different weights were applied step by step on its tip. At the same time the positions of the outer cylinder hull and the tip of the stroke unit were measured with a dial gauge. For the outer cylinder no change in the position was observed. The stroke unit, however, has shown some bad results as seen in Figure 3.8 for maximum driven outwards position. The starting point was with no weight load. Then 10, 20 and 30 kg were applied stepwise and the bending/tilting value noted (blue line). The 30 kg remained hanging on the stroke unit for some minutes. Then everything was done backwards (red line). In addition some upwards forces were applied by pulling on the actuator stroke unit with a measuring spring. The measured values point out two problems:

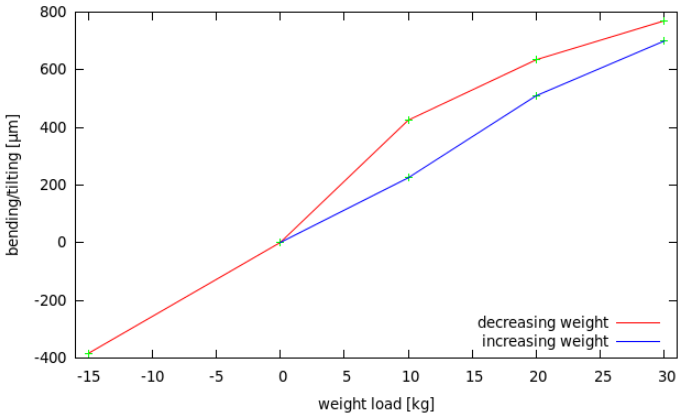

Figure 3.8: Plot of the bending values measured for maximum driven outwards stroke unit position. The blue line shows the values for step by step increased weight load, the red line shows the values for the then gradually reduced weight loads.

- Under a weight load of 30 kg and at 8000 steps, the actuator shows a bending tilting value of nearly 800 μm
- The bending/tilting shows a clear hysteresis for fast changes in the transversal weight load

The hysteresis might become a problem during the alignment of the mirrors. An MST has around 80 mirrors with 2 actuators each. Assuming it needs 5 minutes until the mirror reached its final position due to bending/tilting hysteresis effects, this makes over 13 hours waiting time for moving the mirrors only once. But the first alignment needs a lot of movements for each mirror. This might add up to a too large amount of time. However, if the bending/tilting of 800 μm is not significantly affecting the precision of the actuators, the hysteresis will not have any significant effect either. Compared to the desired precision of 20 μm, the bending/titling value is surprisingly high, but only a fraction of it really affects the actuators effective length. If it is assumed the actuator stroke unit is tilting with a fixed point inside the actuator, a bending b of 800 μm will cause a change in the effective length δ of the actuators:

$$\delta = (l - \sqrt{l^2 - b^2}) \cdot \frac{d}{d+b} \tag{3.8}$$

δ depends on the actual bending value b and also heavily on the actual actuator stroke unit length l. d is the distance between the actuators and an actuator and the rotating bolt. Here it is assumed only one actuator is bending while the other one is stiff and has the same length l. The actuator stroke unit length is a little underestimated with 14 cm. δ will become larger with smaller l (for a constant b). See Figure 3.9 for a plot of the function. Underestimating l prevents underestimating δ. This results in a $\delta = 2.29$ μm for the actuator–rotating-bolt axis and assuming the rotating bolt is stiff. 2.29 μm is 48% of the precision given by the motor and spindle. But there is a not yet fully considered fix parameter: the distance between the actuators and an actuator and the rotating bolt d is always 60 cm. This means the rotating bolt and the actuators have to bend together. In a simplified case of two actuators holding a bar representing the mirror, this should result in a change in the distance of the mirror to the camera of maximum 2.29 μm, what is negligibly small, and nearly no change in the mirror pointing. However, no material is perfectly stiff and there is always a clearance between parts. When an actuator is replaced by a rotating bolt in the simplified picture, then the situation

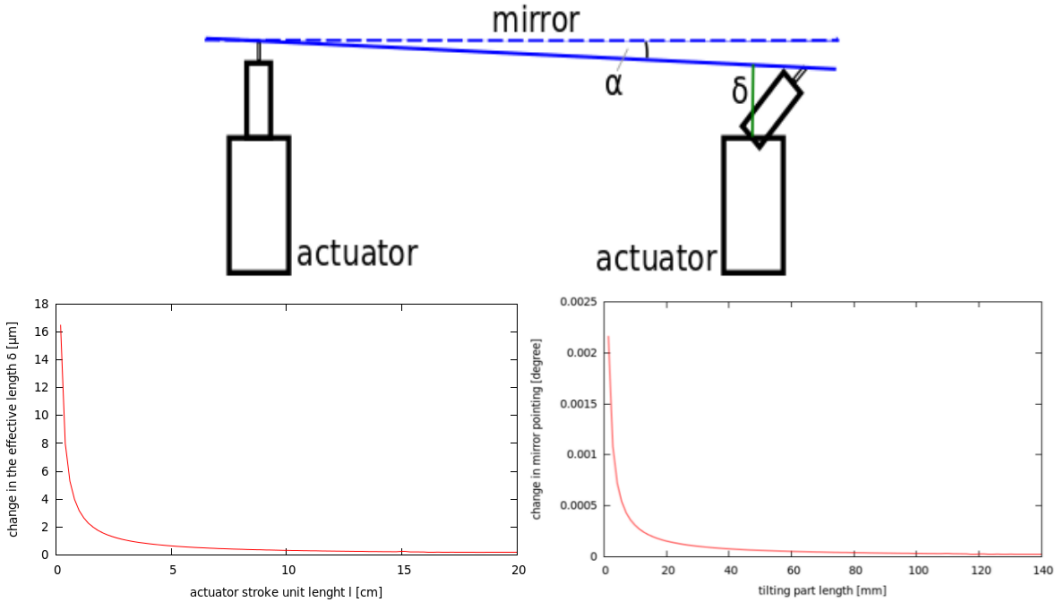

Figure 3.9: left: Change of the effective length of the actuator due to bending for a bending value of 800 μm vs the stroke unit length. right: Change of the mirror pointing vs the stroke unit length. The second actuator is assumed not to bend.

is more complicated and the behavior depends on how optimal the whole mirror interface is mounted on the telescope dish. This is an unknown factor. For such a configuration as sketched in Figure 3.10 left it can be derived:

$$\sqrt{(\sqrt{l_2^2 - b_2^2} + f - \sqrt{l_1^2 - b_1^2})^2 + ((b_2 + d) - b_1)^2} = d \tag{3.9}$$

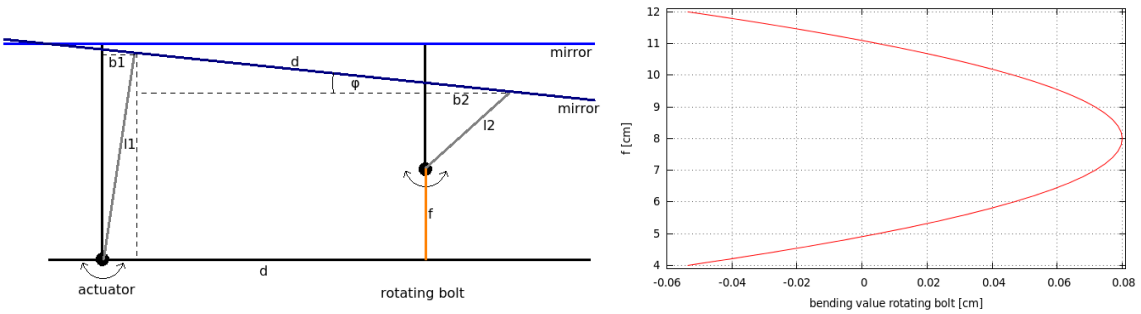

Figure 3.10: right: Sketch for calculating the change in the mirror pointing for a realistic actuator-rotating-bolt configuration.
right: Dependency of the length difference of the tilting part of the actuator f on the bending value of the rotating bolt b_2, derived from equation 3.9 and calculated for an actuator bending value b_1 of 800 μm

l_1 and l_2 are the length of the actuator stroke unit as tilting part and the rotating bolt, b_1 the measured bending value for the actuator and b_2 the resulting bending value for the rotating bolt. In an optimal mounting case, fully tangential to the dish, f is the difference of the actuators tilting part and the rotating bolt. Here the rotating bolt can follow the actuators tilting in the same direction. For a bending value of 800 μm this again results in

nearly no change in the mirror pointing, but just a small and negligible change of the mirror distance to the telescope camera.
In the case of a not optimal mounting and a triangle not tangential to the dish, this might have to be compensated during the prealignment by changing the connection point between the actuator and the triangle. This results in a situation as sketched in Figure 3.10 with a different f. Here, if the actuator tilts to the right, the rotating bolt might have to tilt to the left and thus increases the change in the mirror pointing. For f bigger than 5 cm and smaller then 11 cm this is still not a problem. But the exact behavior - also for optimal mounting of the triangle on the dish - depends on the exact fabrication of the system. Clearances, deviations of the distance between the actuators and the rotating bolt on the triangle, but also their connection points to the mirrors (e.g. the glued pads), can make the rotating bolt to prefer one or the other direction. However, the triangles are always mounted with the corner harboring the rotating bolt pointing upwards. This means gravity always pushes the mirror towards the actuators and away from the rotating bolt and ground. In Figure 3.10 left the weight forces would be point to left and down, depending of the angle between the mirror and the ground. For small angles only a small part of the weight force pulls perpendicular on the actuator, causing a small bending only. When the angle is larger, the bending is larger too. But the weight force is also forcing the mirror move as much as possible to the left (in Figure 3.10 left) and thus the rotating bolt to bend to the left too. Because the rotating bolt has a ball joints at each end, which allow free rotation, it can freely follow the mirror. Therefore, $\delta = 2.29$ μm can be assumed as maximum error in the actuators effective length for 30 kg weight load and 8000 steps outwards driven stroke unit.
The bending is not increasing the step width of the actuators. So, ignoring the hysteresis effect, during the first alignment all bending effects should get automatically repaired, but only for the telescopes zenith angle at which the alignment was done. When the telescope moves to different zenith angles, the mirrors press and pull in changing directions on the actuators. This means a changing bending value and thus a changing mirror pointing. However, this is not the only effect impacting on the telescope PSF. The dish itself is not perfectly stiff and deforms with a change in the telescope zenith angle. The deformation of the dish is unequal for the upper and lower, as well as for the inner and outer dish parts. This changes the pointing of the mirrors, depending on their position on the dish, in different directions and the telescope PSF is increased. From the H.E.S.S. array it is known, that the telescope PSF is dominated by the dish deformation. However, the precision of the MST actuators shall be kept not as good as the H.E.S.S. actuators. Therefore a better look on what affects the telescope PSF how much is taken with the help of some simulations in the next section.

3.3.3 Actuator precision and the PSF of MSTs

At the time this thesis was written no values for the MST dish were available. To still be able to look into a somewhat realistic case, values measured on the CT1 and CT3 telescope dishes of the H.E.S.S. array were used. In the simulation the dish deformation is described by the function $\sqrt{a[sin(\theta) - sin(\theta_0)] + b[cos(\theta) – cos(\theta_0)]}$ that gives an additional error in the mirror pointing for each individual mirror depending on the telescopes elevation angle. θ is the zenith angle of the telescope and θ_0 the zenith angle at which the alignment was done. θ is chosen as 26.6 degree in all simulations, also taken from H.E.S.S.. For a, a value of 0.023 in horizontal and 0.01 in vertical direction is measured on the CT1 and CT3. For b it is 0.0 and 0.0. Also, the parameter *mirror_align_random_distance* was set to 2.0 cm. The numbers were taken from the *sim_telarray* manual. How much an actuator is affected by bending depends on its position on the dish and the zenith angle of the telescope. Due to

the curvature of the dish, each mirror has a different angle to the ground (θ). The fraction of the mirror weight that pulls perpendicular to the actuator depends on the cosine of this angle. Therefore, all the actuators are affected differently by bending. The telescope dish has a focal length of 16 m (= radius of a sphere with the same curvature) and a diameter of 12 m. This results in an angle between the tangents of the outmost parts of opposite sites of the dish of 44 degree and thus a difference in the forces perpendicular to the actuators of a factor of up to $\frac{cos(0)}{cos(44°)} = 1.39$. *sim_telarray* does not have any parameter representing bending effects alone. As approximation the source code of the simulation was changed once again to add up linearly the maximum uncertainty in the mirror pointing produced by bending to the randomly assigned uncertainties produced by the actuator step width. This overestimates the bending effects. Figure 3.11 shows the results of the simulations. The values are simulated with a *mirror_align_random_horizontal* and *mirror_align_random_vertical* of 0.001 degree for the actuators precision. Figure 3.11 compares the result of the simulations with and without bending for perfect and somewhat realistic mirrors. The realistic mirrors where generated the same way as in section 3.2. No error bars were plotted, because their size is roughly equal to the size of the data points. For perfect mirrors, an increase in the R80 of the telescope of 0.04 mrad can bee seen for a zenith angle of 75 degree. This is less than 6.6% of the R80 without bending included. For zenith angles closer to the alignment angle of 26.6 degree the increase is smaller. For imperfect mirrors no change in the telescope R80 is found. The results of the simulation show no effect on the telescope performance through

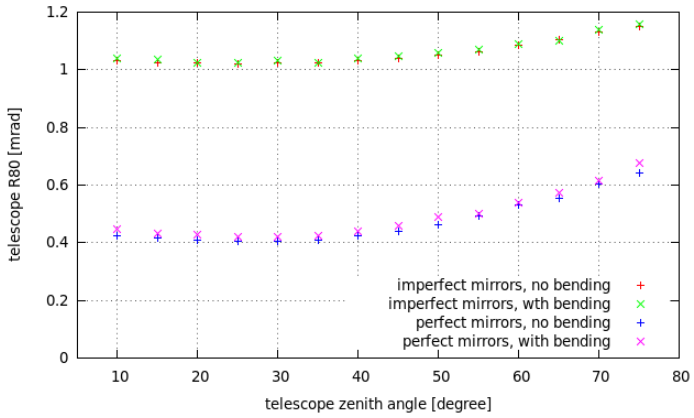

Figure 3.11: Simulated R80 for on axes events at different telescope zenith angles, for realistic and perfect mirrors, each with and without bending.

bending for the realistic mirrors. The bending was overestimated in the simulations. On a real telescope and during normal operation, not the whole mirror weight pulls and pushes on the actuator perpendicular to the spindles axis. Also, the stroke unit should be moved out of actuator around 4000 steps only. Both lead to a smaller bending value as used in the simulation. This leads to the conclusion that the measured bending does not affect the actuators precision significantly.
Besides the result for the precision, any kind of unexpected freedom in movement of parts of the actuator at least indicated the danger for unwanted stress working on the materials. In case of the bending this even concerns the spindle and thread, which, together with the motor and the electronics, are the most important parts of the actuator. Considering storms and ice on the mirrors, the forces working on the actuator increase up to a factor of 4 to 5 over the values used in the measurement. When examined by hand and eye, the outer cylindric hull and the guidance of the stroke give the impression of being to fragile. The latter can even

be slightly deformed by hand. Therefore, the survivability of the actuator under extreme conditions is questioned. More tests are needed and probably design changes necessary.

3.3.4 Reliability of the position switch

The motor's hall sensor only provides a way to count the steps the actuator stroke unit moved relative to a starting point. As seen in the results of the linearity tests, the behavior is sufficiently linear. But just by counting steps it is not known how much the actuator is actually moved in or out in absolute values. A reference position is needed. One way to find a reference position is by moving the actuator stroke unit up or down until it hits the end of its range and presses against the top or bottom of the actuator. The motor current is rising over a predefined value and signals that the actuator has to be stopped. But because the motor is not stopping immediately, this applies mechanical stress to the actuator parts, especially the spindle thread. And it is not possible to distinguish between the most inwards or outwards position of the actuator stroke unit. In order to solve this problem a sensor is put into the actuator. The sensor is meant to give a signal when the stroke unit is very close to its maximum inward position and the motor can be stopped safely. It is sufficient for the sensor to have a precision of millimeters. However, a precision of the order of the actuator step size (μm) has the advantage that, in case of power blackout and the loss of the electrically stored position of the stroke, the position can be reproduced buy just moving the stroke unit to the reference position and counting the steps needed. Therefore a μ resolution is preferred.
The used sensor is an inductive proximity sensor of the type IM04-0B6PO-ZU1 from SICK Sensor Intelligence. The sensor is producing a magnetic field and measuring its strength. Most of the actuator is made out of aluminum, which is paramagnetic. If some steel (ferromagnetic) get close to it, the magnetic field strength gets changed and the sensor changes its sent signal.
First, the sensor's reliability was tested in the climatic chamber by moving the stroke unit, without weight load and at a temperature of 19.5 degree, several times from a fixed starting position to the reference position (sensor gives signal) and back. The number of steps the stroke unit was moved until the sensor reacted was recorded (see Figure 3.12 left). The statistics are small, but an error of 1 step in 1 out of 10 movements is a good result. Equally good results with low statistics have been reproduced. However, repeating the test for different temperatures (-20, 0, +20 and +40 degree) and 10 kg weight load have shown a too big temperature dependence. This can be seen in Figure 3.12 right. The position at which the sensor gives a signal varies more then 40 steps. 40 steps are only 0.5 % of the maximum range, but still much more than expected. It is unclear what causes this big dependence. However, the sensor is mounted into the actuator by just gluing it into a hole drilled for it. Looking at this, it might be the position of the sensor has changed due to thermal expansion of the surrounding material. This might also influence the fixation of the sensor. Taking wind gusts, telescope movements and earthquakes into account, which shake the actuators, the sensor might even be moved away from its original position over time. In addition, the mounting for the sensor does not give a precisely defined position for the sensor. Since the sensor reacts very sensitive to the magnetic fields, which change a lot with bigger distance, this might end in completely losing its functionality. Although the sensor is specified to work under temperatures in the range of -25 to 70 degree, it is not known if the temperature has an effect on the sensitivity of the sensor. If it does, this would increase the uncertainty in when the sensor is reacting. And if the sensor is glued too deep into its hole, the sensor maybe will not react at all. It needs to be tested, if the sensor's sensitivity depending no the temperature. Also, a better fixation is needed, e.g. by adapting the size of the holes better

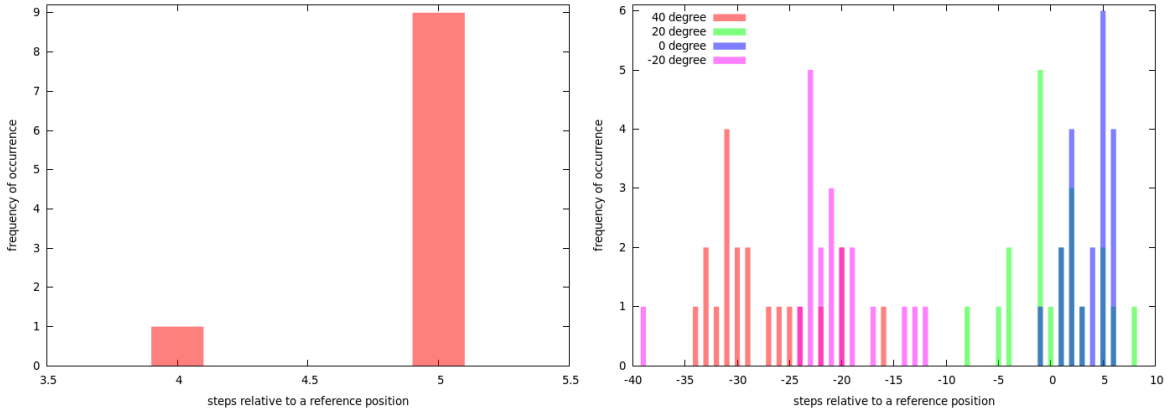

Figure 3.12: left: Histogram of the positions at which the position switch gave a signal for a temperature of 19.5 °C. right: Histograms of the positions at which the position switch gave a signal for different temperatures.

to sensors length and width. Alternatively, a new sensor of better fitting size and without a temperature dependency could be used.

3.3.5 Temperature dependence of the motor current

The motor gives all needed strength to the actuators to move the mirror they carry. But it does not have a built-in intelligence. If for any unforeseen reasons the actuator or mirror gets stuck or blocked, the motor will just keep moving and applying bigger and bigger forces to the spindle and mirror until something might break. To prevent this from happening, an electronic solution is needed. The electronics need a parameter to observe and defined restraints that make possible to distinguish between normal and unusual operation. A good parameter can be obtained by measuring the motor current. Since the motor is working with a constant direct voltage, the delivered power is proportionally depending on the current. To know at what motor current values the motor has to be stopped, the fluctuations during uncritical operation must be known. Therefore, the dependency of the motor current on the temperature was measured in the climate chamber. The temperature range was -20 to +40°C. The used weight load was 10 kg. For the measurements the whole range of the actuator stroke unit was used for moving in outwards and inwards direction. Figure 3.13 shows some exemplary results for moving upwards with the starting point at 0 steps. The two lower curves at around 800 mA were measured for 20 and 40°C. The middle curve at around 900 to 1000 mA was made for 0 degree and upper curve for -20 degree. Clearly visible is a strong nonlinear dependence of the motor current on the temperature. Also, this dependence has a range of over 800 mA or more than a factor of 2 to the minimal current in this temperature range. In addition, for low temperatures the motor current is a lot higher at the start of movement.
The large range of the motor current with changing temperature means it is necessary to define current intervals for safe operation which also depend on temperature. Therefore, the temperature of each actuator needs to be measured too. This could turn out to be very difficult, because the actuators do not necessarily have the same temperature on each side and in each component. To compensate this, a lot of temperature sensors spread all over the actuator might be needed. And furthermore ,the temperature flow inside the actuator would

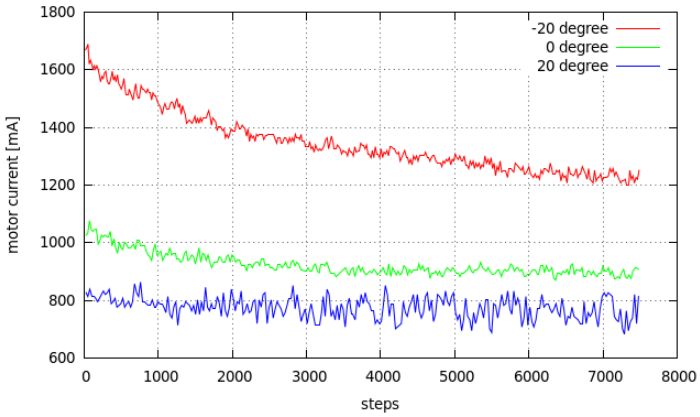

Figure 3.13: Measured motor current vs stroke unit position in steps for different temperatures. The stroke unit was moved continuously outwards for each curve.

be needed to be studied.
The big difference in the starting motor current and the current after some movement at low temperatures is also a problem. It increases the maximum current value with which a problem can be detected. Because of this an emergency might be recognized too late and damage not prevented. More-over, increased currents indicate mechanical stress inside the actuator. Since the actuators shall be operational for up to 30 years all mechanical stress, which corresponds to deterioration, need to be an absolute minimum. The probable cause for the increased current at the start of the movement is the difference in the temperature expansion coefficient with a factor of 10 of the iglidur nut to the steel of the spindle. For low temperatures the iglidur nut shrinks. This increases the friction forces and power needed to move it. Through friction however, heat is produced, the iglidur nut expanses again and the motor current decreases more and more to normal values the longer the actuator is driven. Thus the measured behavior of the current. This could also be just an effect of a rapid change of the lubrication properties of the surface of the iglidur nut with the temperature. Alternatively, friction forces could lead to deterioration of the iglidur nut until it has enough room again to move freely. But no damage to the iglidur nut could be seen by eye.

3.3.6 Actuators on the prototype telescope in Berlin Adlershof

In Berlin Adlershof there is a MST prototype built and operated by DESY Zeuthen. 16 mirrors (4 prototypes and 12 dummies) are mounted with actuator prototypes designed by Buck engineering. There they have been exposed to the environment for about a year without being used or moved. However, all but one of these actuators still work fine and seemed to be in very good shape. One actuator clearly had a lot of water inside its box. At the time the actuator was checked the water had already vaporised and left the actuator through the membrane. But it left a lot of white dust-like traces in the actuator box. It is not clear how the water got in. It seems very likely that the sealing of the box failed, though. The damage the water did to the actuator was not mechanical, but it entered the motor and caused a short circuit that killed it. Also, some steel parts inside the actuator box, e.g. some screws, were rusty. The sealing and overall waterproofness of the actuators requires to be tested further and probably has to be improved.

3.3.7 Summary

The tests have shown that the step width of the actuator is around 5 μm and behaves sufficiently linear against the actuator stroke unit position. No dependency of the step width on the direction or magnitude of the applied weight forces was found. Bending or tilting of the actuator -most probably the actuator stroke unit- increases the uncertainty of the mirror pointing from around 0.001 degree by the actuators step width up to 0.002 degree. The value depends on the mirror weight, the angle between the mirror and the ground and how far the actuator stroke unit is moved out of the actuator. The 0.002 degree is a maximum value for a mirror weight of 30 kg and an actuator stroke unit that is moved out to the maximum range of around 8000 steps, but the requirement on the actuators are to work with even higher weight load (see section 3.1). Therefore more test are need to ensure the desired performance, although the stroke unit should only very seldom be moved out to maximum length and in most cases of operation the bending smaller. A precision better than the goal of 20μm, which correspond to 0.00382 degree, is achieved. However, the actuator design by Buck Engineering needs improvements. The actuator box waterproofness failed once in the field test and lead to the destruction of the electronics in the motor. This also revealed that some parts in the actuator are not stainless. The dependence of the motor current on the temperature, perhaps caused by the thermal expansion coefficient of the iglidur nut or its lubrication properties dependency on temperature, makes it difficult to define parameters for an emergency shutdown. The high starting values for the motor current indicate increased mechanical stress. The bending or tilting of the actuator might cause mechanical stress to different actuator parts, especially the spindle thread, too. Increased mechanical stress leads to increased attrition of the materials. Thus, the lifetime of the actuator can be shortened. It has not been tested how the actuator behaves under extreme condition and if it fulfills all of the requirements stated in chapter3.1 is unknown and because of the high bending value this can be questioned. The longevity of the actuator has been tested only in small numbers and over around one year in Berlin Adlershof. There, the weather conditions are not as rough as at the potential CTA sites. Therefore more test for the lifetime and fitting to the environment of the later used CTA site are necessary.

3.3.8 Outlook

Because of the mechanical reasons stated above, it was decided to design a new improved actuator. The goals for this new design, developed by Lesatech, are to fix the problems of bending, the temperature dependence of the motor current, improve the waterproofness and also make the actuator resistant to hazardous environment influences, as demanded in the requirements, and survive extreme conditions as storm, ice, earthquakes and any combinations of those. Figure 3.14 shows a drawing of the new design. In this design clearances are smaller, the material more resistant and the sealing waterproof. The iglidur nut was exchanged by a bronze nut. Bronze is lubrication free, too. The Sensor to determine the reference position for the stroke unit was also exchanged and its fixation improved. Compared to the design by Buck Engineering, one major change is that now the cylindric outer hull is massive and it is guiding the stroke unit. This guidance concept, that is also used in the H.E.S.S. actuators, should be much more stable and fix the bending problem. However, no tests of a complete prototype have been performed by the time this thesis was written.

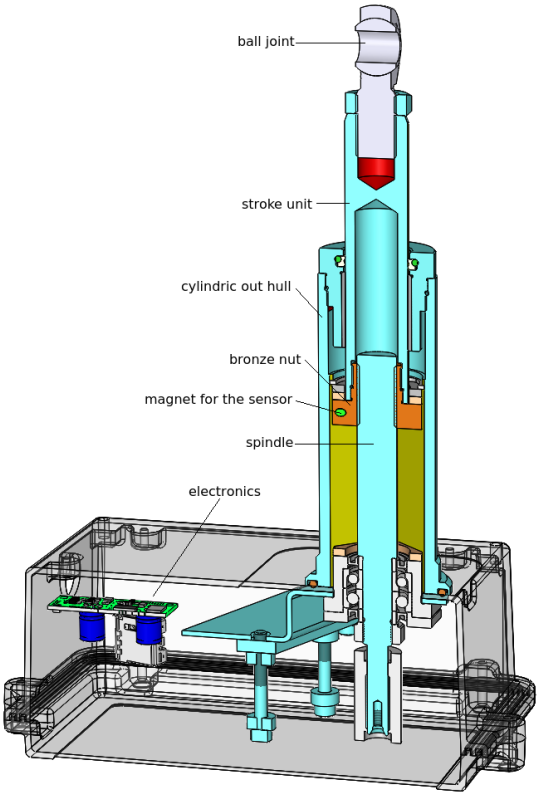

Figure 3.14: Drawing of the new actuator design in development, including the actuator box and electronics.

Chapter 4

Setups To Measure The Quality Of Spherical CTA Mirrors

In this chapter the 2f method for measuring the PSF and reflectivity of spherical mirrors is introduced. Also, the two measurement setups, the old setup built by the MPIK Heidelberg and the new setup in development by the IAAT, wich both use this method are presented and the results from measurements on CTA prototype mirrors discussed.

4.1 Mirror Quality

The reflectors of the CTA telescopes consist of a lot of smaller hexagonal mirrors with a diameter of 78 cm to 151 cm flat to flat. The telescope dish, at which the mirrors are mounted, gives the general shape (spherical, parabolic, etc.) to the reflector. The mounted mirrors need to get aligned to point to the focus of the dish, where the overlapping reflected images of the single mirrors projected on the camera form the total image the telescope camera sees.
The sharpness of the total image for observed on axes events is largely determined by the deviation of the Davis-cotton dish from a parabolic shape, but can also deteriorated by an insufficient sharpness of the images of the singles mirrors. A mirror with a theoretical perfect spherical shape reflects a perfectly shaped[1] image of the observed source. If the radius of the curvature of a mirror is wrong, the inner paraxial part of the reflected image looks still like that of a perfect mirror, but the outer parts have focus points e.g. behind the focus point of a perfect formed mirror. Light reflected by these parts of the mirror is directed to this different focus. The angle between this reflection direction and the optical axis of the mirror is larger than for paraxial mirror parts and this reflected light hits the camera plane in different point. Thus the reflected image of this mirror is enlarged compared to a perfect mirror. See Figure 4.1 for a sketch. The same happens if the mirror has the correct general form, but also local errors. Furthermore, if the surface of the mirror has to much errors on the microscopic scale, e.g. is to rough, a large part of the light will be reflected diffusely.
The image the reflector reflects on the camera does not only give information about the shape of an observed particle air shower, but also gives the amount of total radiated Cherenkov light, and thus the energy of the primary high energy photon, too. To be able to determine the total amount of radiated Cherenkov light, the efficiency with which the Chrenkov photons are collected has to be known. The efficiency is given by the flux of Cherenkov photons arriving in the telescope camera compared to flux onto the reflector. This ratio is mainly determined

[1] spherical aberration ignored

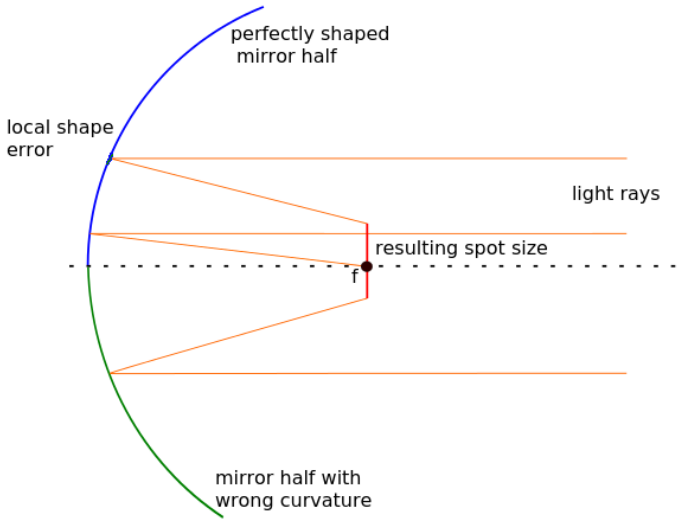

Figure 4.1: Examples for errors in the shape of a spherical mirror, without spherical aberration. The blue half of the mirror has a perfect shape, except for one point with some local errors. The green half has a wrong curvature. Parallel light rays (orange) incident on the mirror surface will not be reflected into the focus f (black spot), if they hit on a part of the mirror with imperfect shape. Thus the resulting sport size (red) is increased and not point like.

by the mirrors reflectivity. In this chapter with reflectivity the ration between the mount of light incident on a mirror and the amount of light focused onto the telescope camera is meant. Because the flux of Cherenkov photons can be very low, the reflectivity of the mirrors has to be as high as possible.

4.1.1 Requirements On The Mirrors For CTA Single Mirrors Telescopes

Ignoring aberrations, when a perfect focusing optic is irradiated by a point source, the reflected image of the source produced by the optics is just a point again. For real mirrors the effects described above are present and the reflected image now is an expanded spot instead of point shape. Because the expansion of the image is caused by the errors of the shape of the mirror, the size of the spot is a good parameter to describe these errors and the quality of the shape of the mirror. The size of a light spot is described by the *point spread function* (PSF). The PSF has no unified definition, but a good measure for the PSF is the radius or diameter of circle containing a certain amount of light. As example for the telescope mirrors, the radius or diameter of a circle containing 80% of the light irradiated on the mirror, usually called R80 and D80 respectively. The center of the circle can be either in the point of maximum intensity or in the center of mass of the intensity.
The reflectivity itself already is a parameter describing the quantum efficiency of the mirrors. Although the PSF is more complicated in detail, it is the reflectivity that is far more difficult to measure, because to determine the precise flux of light onto a mirror will turn out to be a challenge.
For the single spherical mirrors for CTA single mirror telescopes, the requirements on their PSF and reflectivity has been defined as [3]:

- "85% of the light incident onto the mirror between 300 and 550 nm has to be reflected into a spot of 2/3 of the pixel diameter."

- "The diameter of a circle that contains 80% of this light (d80), that is focused into 2/3 of a pixel size, needs to be smaller than 1/3 of the pixel size."

Figure 4.2 right presents these requirements as a drawing. In the next chapters two testing setups to measure the PSF and reflectivity on spherical mirrors will be presented. An older and running setup, and a new setup still in development. The old setup uses a slightly different measure for the PSF and the reflectivity:

- The light focused into a circle of 1 mrad radius around the center of mass of the reflected spot is defined as 100% of the total reflected light.
- The PSF is the diameter of a circle around the center of mass of the reflected spot containing 80% (D80) and 95% (D95) of the reflected light, respectively.
- The reflectivity is equal to the ratio of total reflected light (defined above) to the light incident onto the mirror.

For the mirrors the PSF or a circle diameter is often expressed as the opening angle of two lines originating in the center mirror and ending on opposite sites of the spot or circle. See Figure 4.2 left for a sketch. To be able to compare both testing setups the PSF and reflectivity are measured like this in the new setup too.

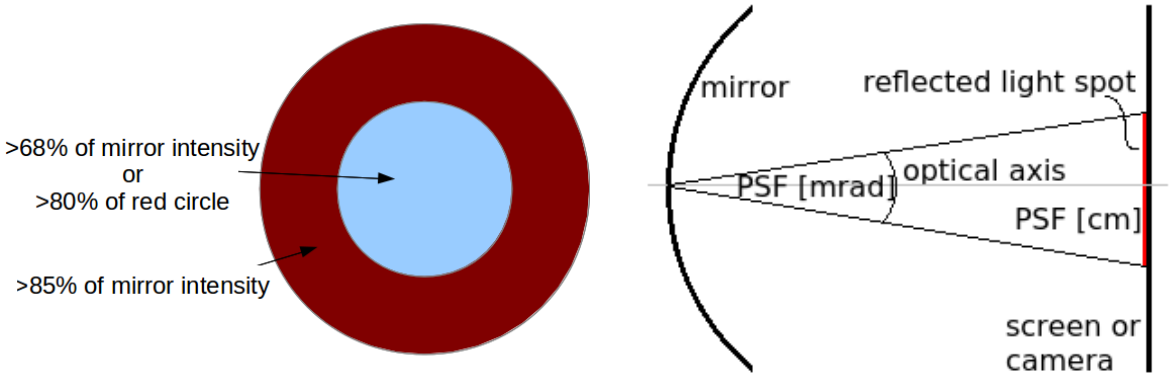

Figure 4.2: left: Sketch of the requirements on mirrors for CTA singel mirror telescopes. The red circle has a diameter of 1/3 of a camera pixel and the blue circle 2/3 of a camera pixel. *Mirror intensity* stands for the total intensity of the light incident on the mirror. right: Illustration on how the PSF as radius or diameter of circle is calculated into an angle.

4.2 Measuring Mirrors

Measuring the PSF and reflectivity of the mirrors for the CTA telescopes is an important task to control the quality of the mirrors. To measure the PSF, a setup is desired in which a perfect mirror, that has to be checked on its quality, produces a point like reflected spot. Then the size of the spot, the PSF, represents the quality of a real mirror with the always present deviations from perfection. The question is how to realize such a setup. Irradiating a mirror with parallel light incidence is not easy done due to the lack of a simple and proper light source. And putting a light source at a large distance would need a laboratory or testing facility with a length of many kilometers. For the spherical mirrors there is a solution in using their spherical properties in the so called 2f method. This method, two setups using it and

measurements on prototype mirrors for CTA single mirror telescopes with this setups will be presented and discussed in the following chapters.

4.2.1 2F Method For Spherical Mirrors

The most important property of a sphere is the total symmetry to its center. When a point like light source is placed in the center of a mirror that is curved like a sphere, all light rays radiated by this light source hit the mirror rectangular to its surface. Since, according to the law of reflection, the angle between the surface and the incident ray is equal to the angle between the surface and the reflected ray, all light rays are reflected back to the point like light source in the center of the sphere. If the mirror sphere is cut in half, the distribution of the light reflected by the half sphere onto the plane covering the open side depends on the quality of the shape of the mirror and how much it deviates from a perfect sphere. In a

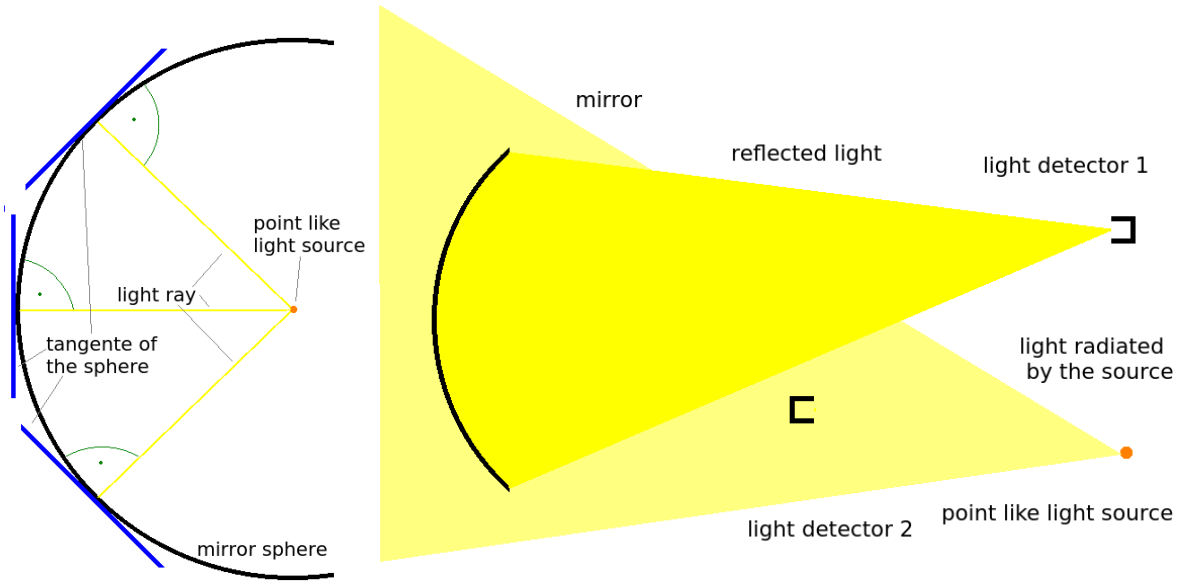

Figure 4.3: left: A point like light source is placed in the center of a mirror half sphere. All light rays hit the mirror rectangular to its tangents and are reflected back towards the center of the sphere. right: The concept of the 2f measurement method. An approximately point like light source irradiates the spherical mirror from a distance of two times the focal length. The mirror is positioned as such, that the reflected light is focused at the position of a light detector. This light detector determines the PSF and the amount of reflected light. Another light detector is placed between the light source and the mirror to determine the amount of incident light on the mirror.

measurement according to the 2f method, the spherical mirror is irradiated by a point like light source from a distance of two times the focal length (2F). Two times the focal length are equal to the radius of a sphere with the same curvature as the mirror. Thus, the situation is the same as described above. A small difference is, that the mirror is slightly rotated to point besides the light source. In the focal plane next to the light source a light detector is placed at which the reflected light is focused on. With the help of this detector the distribution (PSF) of the reflected light in the focal plane can be analyzed. In a second measurement another detector is placed between the mirror and the light source to determine the amount of incident light on the mirror. Figure 4.3 shows a sketch of the concept.

4.3 The Old Setup

The Max-Planck-Institut fuer Kernphysik in Heidelberg has developed a measurement setup to measure the reflectivity and the PSF of the mirrors of the H.E.S.S. phase 1 telescopes [15]. This setup uses the 2f method and, with minor changes, was has been relocated into the cellar of the IAAT for measurements on the mirrors for the larger H.E.S.S.2 telescope. While the H.E.S.S.1 mirrors have a focal length of only 15 m, the mirrors of the H.E.S.S.2 telescope has a focal length of 36 m. For using the 2f method, a laboratory with a length of more than 2 times the focal length of the mirrors, 72 m for H.E.S.S.2, is needed. The IAAT could provide such a facility and all of the 875 mirrors mounted on the telescope plus additional spare mirrors have been tested there.
At the time this thesis is written, parts of this setup are already about 10 years old. Therefore, and also to distinguish between this setup and the new developed one, this setup is referred to as *old setup*. Furthermore, as first step this setup was tested on its functionality and will be used as a reference to compare to the results of the *new setup* in development.

4.3.1 The Components

The old setup uses the 2f method as explained in 4.2.1. Pictures of the single components can be seen in Figure 4.4. As light source, halogen lamps of the type OSRAM HLX 64655 and 64657 XENOPHOT are used. To reduce stray light, the lamp is located inside a container with an aperture. In front of the aperture a *chopper wheel* rotates and choppers the light in periodical peaces. This gives the light a pulse shape with a period depending on the frequency of the chopper wheel. As light detector a photo diode with different filters is used. The photo diode has a light sensitive area of 25 mm^2 and is connected to a lock-in amplifier that is filtering the signal it gets from the photo diode. Only the part with the exact same pulse shape as the light gets by passing through the chopper wheel in front of the halogen lamp is extracted. This makes the whole setup very resistant against influences of background light. The chopper wheel originally was implemented to make it possible to measure the reflectivity and the PSF of the whole H.E.S.S.1 telescopes at their construction site in broad daylight [15] . The filters are located in a filter wheel that rotates to move the desired filter in front of photo diode. Both, the photo diode and the filter wheel, are located in a black box with one round opening for light to come in. On top of the opening a tube can be plugged to reduce stray light. There are four narrow-band filters of different wave lengths in use: 310 nm, 400 nm, 470 nm and 600 nm. The halogen lamp in its container is mounted on a front corner of a 3D moving table. The moving table is like a table without tabletop, but with an arm that is able move a screen mounted to it freely in all directed. Under the screen the photo diode box can be mounted. Both count as *detector 1* in Figure 4.3. There is another position for the photo diode at about 2 m in front of the halogen lamp, corresponding to the *detector 2* in Figure 4.3. Also at about 2 m distance, but in front of the screen and the diode position on the moving table, a camera, that used without filters and that is not sensitive in the uv, is located to take images from the reflected spot on the screen.

In a distance of two times their focal length to the light source the mirrors are mounted on a special bracket. The whole apparatus is mounted on wheels on one side and on a rail on the other side. The rail is not fixed to the ground, so it can be moved to any position needed according to the mirror focal length. There are different options to mount the mirror. The usually preferred one is to fix the mirror on a light steel frame with its pads and screws. Then the frame is mounted on the big apparatus by putting it onto two flat steel hooks and fixing it with a third hook from above. If a mirror has no pads glued to it, it will be directly mounted to the big apparatus like the frame work, but with some soft buffers. There are also

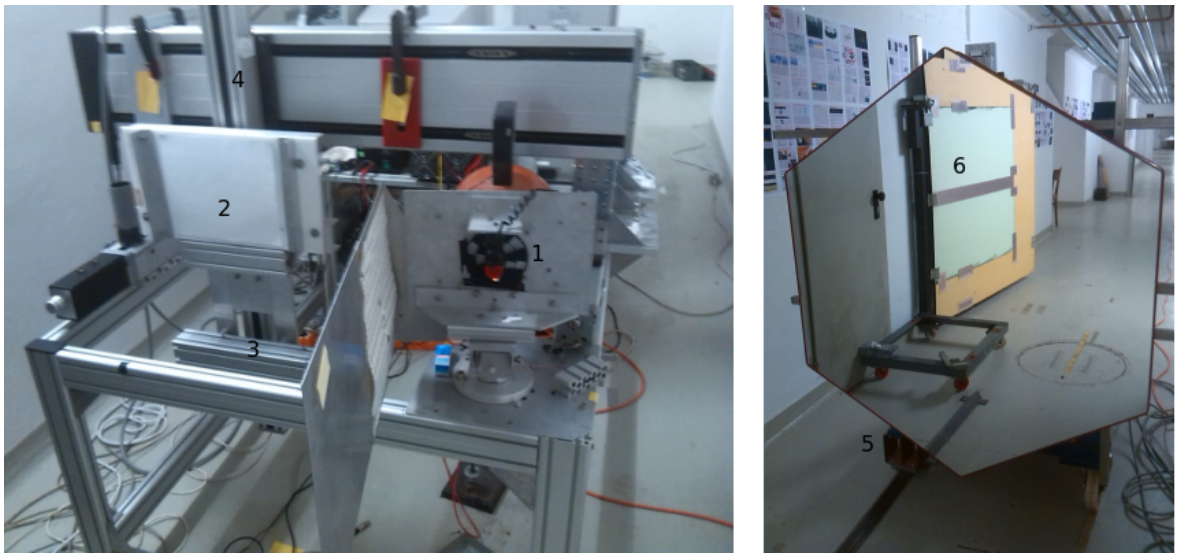

Figure 4.4: Pictures if the old setup (left) and an MST prototype mirror mounted on the mirror mounting. 1: The container (orange) of the halogen lamp with the aperture and the chopper wheel in front of it. 2: The screen at which the reflected light spot can be seen, for images with the camera. 3: Position of the photo diode for the scan over the reflected light spot. 4: The arm of the moving table that holds the screen and moves the photo diode over the reflected spot during the scan. 5: The portable rail of the mirror mounting. 6: An MST prototype mirror, reflecting the image of the large shutter to cover the mirror for the background measurements.

smaller and softer hooks available. However, if a mirror practically stands on one of its edges, what they are not designed for, it can bend and deform under its own weight what might very much influence the measurement. The light reflected by a mounted mirror can be aimed at the screen or photo diode at the moving table and next to the light source with the help of two actuators, similar to how the alignment of the mirrors work on the telescope. In front of the mirror a mobile shutter can be placed to cover the mirror for background measurements. The moving table, the photo diode with the filter wheel, the lock-in amplifier and the chopper wheel are all connected to a central control Linux pc with custom written software(MPIK Heidelberg).

4.3.2 Measurement Procedure

The old setup has two measuring procedures. The faster one of those has not been used for this thesis due to its high uncertainties in the measured values. For the long but more precise measurements the procedure is the following:
As first step the halogen lamp needs to be running for at least 8h with constant voltage to prevent fluctuations during the measurement. When the lamp is stable, the mirror, that is placed in a distance of two times its focal length to it, is aligned to reflect the incident light onto the screen at the moving table next to the lamp. Then, the arm of the moving table is moved until the photo diode mounted under the screen is at the same location as the spot. During this movements, the photo diode always stays in the same plane parallel to the mirror and at a distance of two times the focal length of the mirror as much as possible. With this the position of the spot is known to the control pc for later use. But prior to this, the photo diode is placed in front of the halogen lamp with about 2 m distance and on the line connecting the

lamp with the center of the mirror. Here, the flux of the light is measured for all four filters. This is referred to as *reference measurement*. After this, the photo diode is mounted on the arm of the moving table again. Next, three images of the reflected spot on the screen are taken by the camera. Right afterwards the shutter in front of the mirror is closed and three more pictures are taken for the background measurement. Later in the analyses software the three picture of the reflected spot as well as of the background are averaged and the average background image is subtracted from the average spot image. From this picture later, a PSF for crosschecking is calculated, as well as the position of the spot derived. As final step the photo diode is moved stepwise over the whole reflected spot and the surrounding with the help of the moving table, measuring the flux of the reflected light and producing another image of the spot with a pixel size equal to the size of the photo diode (5 mm × 5 mm). The reflected light spot is scanned with the photo diode one time for each of the four filters.
After the measurement is done, all data are transfered to the analyses PC. The analyses software is written in astroroot and does all the analyses automatically. For each filter the reflectivity and PSF is calculated out of the images of the reflected spot created by the scan with the photo diode over the reflected spot. For the reflectivity the reference measurement is also used. From the measured value of the reference measurement the light flux through an area of the size of the diode at a distance of 1.91966 m from the halogen lamp is known. The light flux per unit area F(r) is decreasing with $\frac{1}{r^2}$, with the distance from the point like light source r. Hence, the flux onto the mirror F(2f) can be calculated as following:

$$F(2f) = L \times \frac{1}{(2f)^2} \tag{4.1}$$

$$F(d) = L \cdot \frac{1}{d^2} \tag{4.2}$$

$$F(d) = \frac{I_{diode}}{u \cdot s} \cdot \frac{1}{A_{diode}} \tag{4.3}$$

$$F(2f) = F(d) \times \frac{d^2}{(2f)^2} \tag{4.4}$$

L is the luminosity of the halogen lamp, d is the distance of the diode to the halogen lamp during the reference measurement of 1.91966 m, f is the focal length of the mirror and A_{mirror} and A_{diode} are the areas of the mirror and the diode, respectively. For F(d) the measured signal from the photo diode I_{diode} can be taken, but scaled with a conversion factor u·s. u ensures the the correct units and s scales the value according to sensitivity of the photo diode. Photo diodes usually have a linear behavior, meaning the measured current at the photo diode is proportional to the light flux onto it. This means the measured current values do not need to be scaled and s is equal to one. Therefore, the light flux at the position of the reflected light spot, represented as a current I_{refl}, is just given by the sum over all currents measured in the single pixels of the scan I_i and the reflectivity R as:

$$I_{refl} = \sum_i I_i \tag{4.5}$$

$$I_{mirror} = F(2f) \cdot s \cdot A_{mirror} \tag{4.6}$$

$$R = \frac{I_{refl}}{I_{mirror}} \tag{4.7}$$

The PSF is calculated by first transforming the coordinates of the pixels of the scan images into the coordinate system in which the chosen center of the spot is in the origin. The center of the spot is chosen by eye during the measurements with the help of the images of the reflected spot taken with the camera. Then the analysis software searches the smallest circle

which contains at least 95% and 80% of the reflected intensity and has its center in the origin. As described in section 4.1.1 100% of the reflected light is defined as the light that falls into a 1 mrad radius circle. The diameters of the circles are the measured PSF (D95 and D80). It need to be considered that a pixel of the scan image can only be completely inside or completely outside of a circle. Hence, the PSF values vary in steps of one pixel. A second PSF is calculated from images taken with the camera. This value is averaged over the whole bandwidth the camera can observe, but is calculated out of an image with higher resolution and gives a second value that can be compared to the PSF measured with the photo diode scan.

4.3.3 Hand Reflectometer

To have alternative measurements to compare to the 2f-setups, a hand reflectometer was used to measure the reflectivity of all available mirrors. The hand reflectometer, which is a loan from the MPIK Heidelberg, consist of 3 major part: The reflectometer itself, glass fibers clamped into thin metal pipes in a y-form and a round foot. Figure 4.5 shows an image of the whole device. The pipes containing the glass fibers function as a leg on which the reflectometer stands. The foot gives the needed balance to stand and also function as cover to darken the part of the mirror that is measured. The reflectometer contains a lamp that is operated in a pulsed mode with a frequency of 200 Hz. This light is guided by the glass fibers to a distance of about one centimeter or less to the surface of mirror. From there it is radiated onto the mirror. A part of the light is reflected, later collected by the glass fibers again and guided into the reflectometer where it is analyzed. As first part of the measurement, the reflected light signal of a reference mirror has to be measured. Now, all new measured values are given as relative values to the reference signal. If the reflectivity of the reference mirror is know, a file containing it can be loaded into the pc software. Then, the software will automatically calculate the relative values into absolute values.

While handling the hand reflectometer, the thin leg turned out to be the weak point in

Figure 4.5: Pictures of the hand reflectometer, with the pipes containing the glass fibers (1) and the additional supporting.

the construction. The glass fibers are very sensitive to deformations. Under the weight of the relfectometer the thin leg bends slightly. This means the glass fiber bends too and the carried light signal changes. Furthermore, during several measurement this process seems to be neither completely reversible nor reproducible, resulting in fluctuations of the measured

reflectivity of even up to 10%. Therefore, the device was upgraded with an additional supporting for the leg, stabilizing the shape of the glass fibers and reducing the fluctuations of the measured values. The reflectivity of a mirror was determined by measuring its reflectivity in 20 to 30 points on its surface and averaging over all values of the measured points.
There is an important difference between a measurement with a hand reflectometer and a measurement with a 2f-setup. The hand reflectometer collects the reflected light very close to the mirrors surface. In the 2f-setup diffuse reflected or not correctly focused light, e.g. due to errors in the local shape of the mirror, will not arrive at the 2f-setups detector and not contribute to the measured reflectivity. This is an intended effect, because it is the same situation as for a mirror on a telescope. But the proximity of the hand reflectometer to the mirror surface leads to the gathering of a large fraction of this light. Thus, the reflectivity values measured with the hand reflectometer are expected to be higher than the values measured with the 2f-setups. Experiences of the MPIK Heidelberg with the mirrors of the H.E.S.S. 1 telescopes give a usual difference in the measured values of about 5% [15]. But since this depends on the quality of the mirror as well on the coating, this might differ for other mirrors, especially all the CTA mirrors. However, this effect should be independent from the wavelength of the light and therefore producing an offset only.

4.3.4 Mirror Measurements

As a first test for the old setup, an old spare mirror for the H.E.S.S 2 telescope was measured. The mirror has the name G711, a diameter of 90 cm flat to flat (hexagon) and a focal length of 36 m. The results for reflectivity and D80 of several measurements on this mirror can be seen in Figure 4.6. In addition to the reflectivity measured with the old setup, the values of a measurement with the hand reflectometer are plotted. The plots show a deviation of the

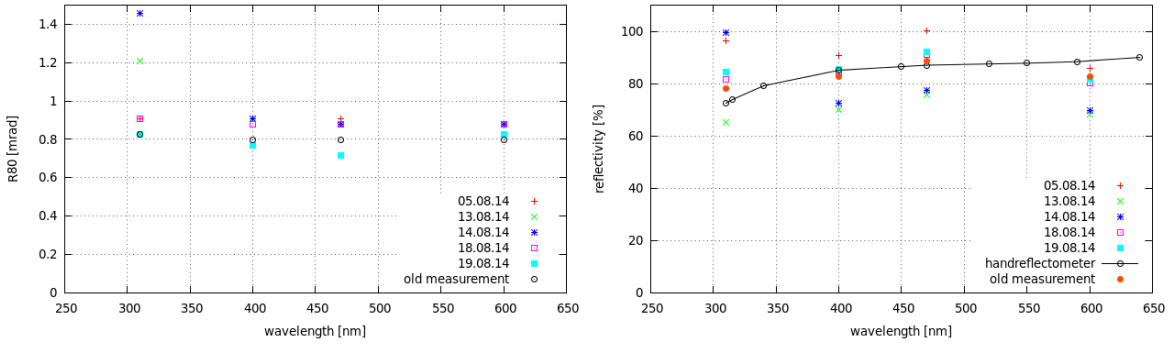

Figure 4.6: Result of the different measurements on the H.E.S.S.2 mirror G711 with the old setup. The *old measurement* was found in archives of the H.E.S.S. mirror campaign. left: Measured PSF values. right: The measured reflectivity values with the result of a measurement with the hand reflectometer.

measured reflectivity values measured with the old setup of up to 20% for 400 nm, 470 nm and 600 nm wavelength. For 300 nm the deviation is even higher, but easily explainable. The halogen lamp does not produce as much light in the uv as for higher wavelengths. Because the lamp was operated with only 20 V instead of 24 V to increase its life time, the flux measured with the diode and the 300 nm narrow-bad filter was less than one order of magnitude above the noise. For the other filter the signal to noise ratio was of the order of 100 too 1000, increasing with the wavelength. Here, the deviations can be explained differently:
As described in section 4.2.1, the detector to determine the light flux onto the mirror surface

has to be placed exactly on the virtual line connecting the point like light source and the center of the mirror. Then, the flux onto the mirror can be determined with the help of the circle symmetry. But for the old setup this is not automatically the case. The container harboring the lamp has to be realigned by hand each time the lamp is changed, what is usually every 200 hours. But there is no built-in help for aiming the light onto the mirror center. Also the position of the photo diode for the reference measurement (detector 2 in Figure 4.3) can vary up to two centimeter perpendicular to the symmetry axis of the lamp-mirror system, because there is no proper marking telling where it has to be placed. Figure 4.7 shows an image of a Teflon screen right in front of the photo diode at the position of the reference measurement. The Teflon screen was illuminated by the halogen lamp with the 5 mm aperture in front of it, as it was used for the measurements of the mirror G711. A small black square shows the position of the photo diode behind the Teflon screen. The line shows the cut at which the profile of the light distribution on the screen was taken. Figure 4.7 right shows the profile. In the image of the light distribution, the maximum should be at the position of the photo diode. But obviously this is not the case, although it was tried to align the halogen lamp and the photo diode properly. The mirror G711 has a diameter flat-flat of 90 cm. A projection of this mirror into the image taken at the position of the reference measurement has a size of about 125 pixels while the diode has a size of 20 pixels (5 mm). If during the reference measurement the photo diode is placed in a 1 cm to the side of its optimal position, then, in the image of Figure 4.7 left, the photo diode measures the intensity of a part of the light distribution 50 pixel away from where it should. Over 50 pixels the intensity changes up to 500 units of the camera. This makes an uncertainty of $\pm 1.4\%$. The two youngest measurements (14.08.14, 18.08.14 and 19.08.14) and the old measurement that was found in archives all are inside an interval of 5% reflectivity. Since it can be expected the position of the photo diode for reference measurement is not the only sorce of errors, the 5% interval is not surprising and still reasonable. The other three measurements however differ a lot. The reason is, for this three measurements no aperture was used. Without an aperture the light distribution is much more narrow and decreasing faster, resulting in a much higher uncertainty.

When taking a second look at the measured values of a single measurement a pattern can

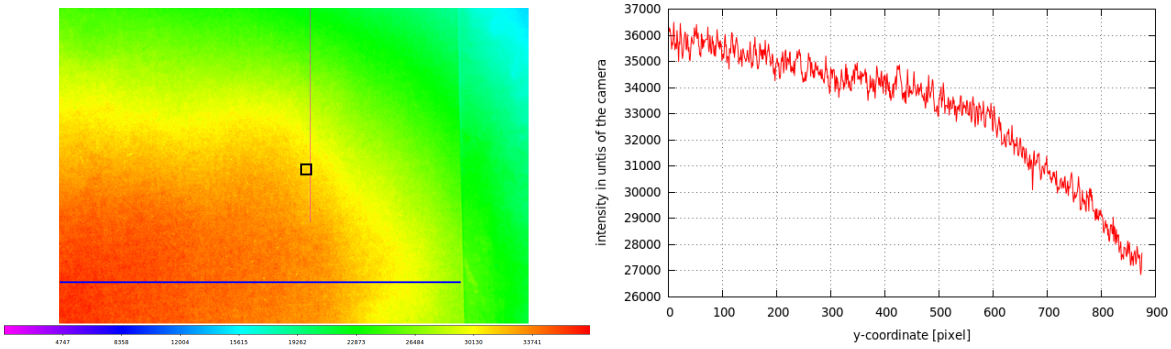

Figure 4.7: left: Color coded distribution of the light of the halogen lamp on a Teflon screen right in front of the photo diode at the position of the reference measurement. The square shows the exact position and size of the photo diode. right: Profile of the light distribution on the Teflon screen alongside the blue line.

be recognized. The measurement with the hand reflectometer shows that all values for 400 nm and above should be equal. However, the values measured with the old setup are not. The reflectivity for 470 nm always is above the reflectivity for 400 nm and 600 nm. And the value for 400 nm is always above 600 nm. This increases the error in the measured values for

a few percent, but also can be taken into account when the measurement results are rated and so that there is no significant increase in the uncertainty.
Figure 4.6 right shows the PSF (D80) values measured with the old setup for the mirror G711. The PSF should not depend on the wavelength and thus all four values of one measurement should be equal. For most of the plotted measurements this is the case. The values for 300 nm vary again because of the too low intensities of the halogen lamp operated with 20 V in this wavelength. The PSF values from the measurement 19.08.14 show an unexpected characteristics similar to the reflectivity values, but turned upside down. An attempt to explain this will follow further below.

Next, two Krakow MST prototype mirrors have been measured with the old setup. The results can be seen in Figure 4.8. Here, the reflectivity and PSF values show the same pattern

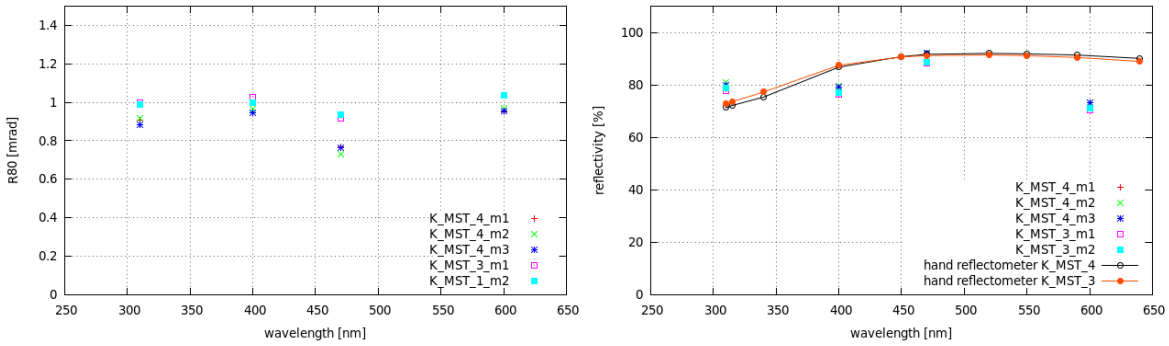

Figure 4.8: Result of the different measurements on two MST prototype mirrors with the old setup. For the measured reflectivity values (right) the result of a measurement with the hand reflectometer is plotted. A pattern can be seen for both, the PSF and the reflectivity values.

as seen for the G711 mirror. For the reflectivity values the pattern look even stronger. But the hand reflectometer measurements shows that for this MST mirror the value for 470 nm has to be about 1% higher than for 400 nm and 600 nm. Still, here all the PSF values have the pattern as seen in just one measurement of the G711 mirror, too. Three of the measurements even vary up to 20%.
Figure 4.9 shows the results of the measurements on an SST mirror. Again, all the measurements show the same pattern in the PSF and reflectivity values as for the other mirrors. The reflectivity values from different measurements vary a lot, because the alignment of the halogen lamp has been very difficult. The SST mirror was a thin glass mirror. When it was mounted with hooks standing on its edge, it started to bend under its own weight. Therefore, the metallic bar construction used to mount the H.E.S.S 2 mirrors on their pads has been adjusted to be usable for the SST mirror. However, the mirror center now has been higher than for all other measurements before. Due to this, the position of the diode for the reference measurement had to be changed accordingly. Unfortunately, the mounting for the photo diode has not been designed for this. Additionally, because of the proximity of the mirror to the moving table, the halogen lamp needed to be turned more than it was possible. In the end the mirror was measured with different lamp and photo diode configurations. All configurations have not been optimal, leading to results plotted in Figure 4.9. Nevertheless, this only explains an offset of the reflectivity values, not the pattern. But, in the PSF values, there are two measurements where the pattern is much stronger. Since the big difference of the single measurements is the configuration of the halogen lamp and the photo diode during the reference measurement, there has to be a connection. It also needs to be mentioned, that

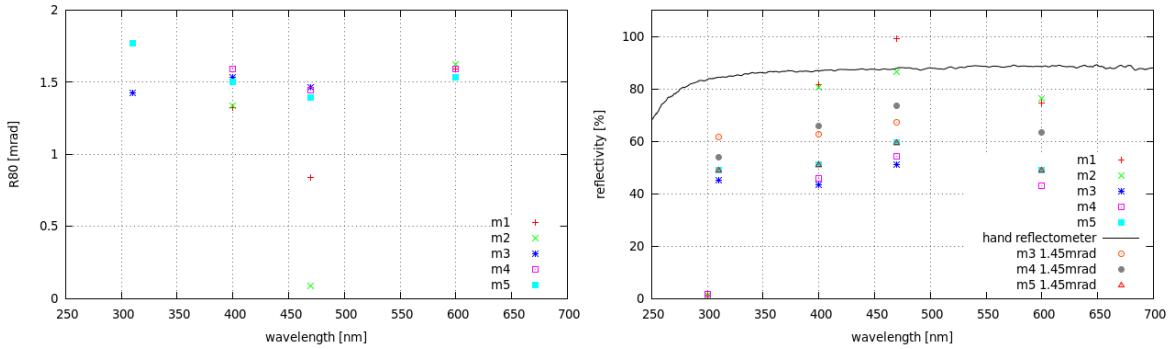

Figure 4.9: Result of the different measurements on an SST prototype mirrors with the old setup. For the measured reflectivity values (right) the result of a measurement with the hand reflectometer is plotted. A pattern can be seen for both, the PSF and the reflectivity values. The large variations in the values of different measurements is caused by different configuration of the halogen lamp and the photo diode during the reference measurement, that could not been set optimal.

for the SST mirror the actual size of reflected spot is smaller than one step of the photo diode during the scan.
Both patterns for the PSF and reflectivity have in common, that it seems like the values for 470 nm are out of place. In general, there is a dependency on the wavelength. The obvious question is, if the narrow-band filters are the problem. Hence, they have been send to the MPIK Heidelberg, where their transmission has be tested. Figure 4.10 shows the results of the test. They reveal that the filters are of different types. The 600 nm filter also a trans-

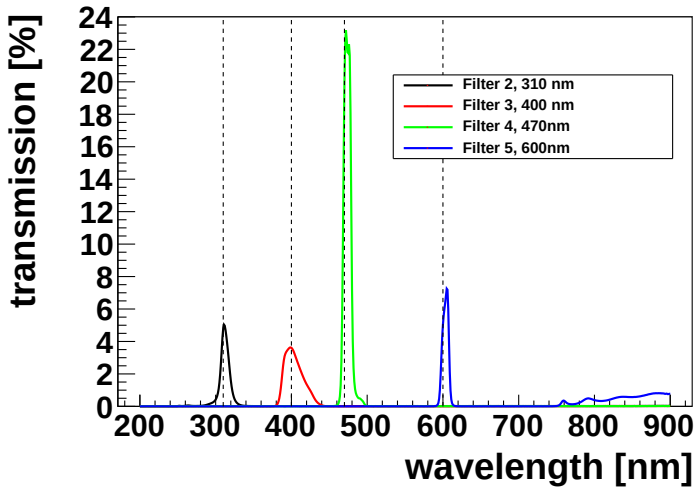

Figure 4.10: Transmission of the filters of the old setup, measured by the MPIK Heidelberg.

mission higher than zero for wavelengths higher than 750 nm. There the mirror have a lower reflectivity, decreasing for higher wavelengths. The halogen lamp is also producing a lot of light in this band. This means, the setup is actually measuring a mix of the reflectivity of the narrow bad of the filter and the band above 750 nm, which is lower than the expected value. The 470 nm filter has a much higher transmission than the other filters and has to

be of a very different type. Indeed, it is an interference filter while the others are not. It might be speculated, that either through the difference in material and function principle or through aging of the filter, the photo diode behind them sees the light of the reflected spot in different ratios depending on what filter is used. Any way, if the filters are the problem, using new filters of the same type will be the solution.

4.3.5 Improvements On The Old Setup

In parallel to the development of the new setup described in the next section, the old setup was upgraded and some better measurements have been made. The writer of this thesis did not participate in this work. Nevertheless, the measurement results will be used to compare them to measurements with the new setup in the next chapter. Also, the upgrades shall be introduced here too:

- The pointing of the halogen lamp and the position of the photo diode for the reference measurement is now controlled and adjusted with the help of a laser.
- The aperture now has a little smaller diameter of 3 mm and is located closer the Halogen lamps. This widens the light cone of the lamp a even more, flattens the light distribution seen in Figure 4.7 and decreases the uncertainty in the measured reflectivity values due to errors in the alignment of the lamp, the photo diode during the reference measurement and the center of the mirror.
- The filters have been replaced by new ones of the same type and from the same producer.
- The measured SST mirror now is mounted with its center in the same hight as the other mirror types. This makes it unnecessary to adjust the position of the photo diode for the reference measurement in hight.

4.4 The New Setup

The old setup, especially after the upgrades, is working and delivering reliable results. However, a full measurement of one mirror lasts 6 to 8 hours. For the CTA project it is planned to verify the quality of a large fraction of maybe 10% to 20% of all mirror that will be used. All the planed CTA telescopes together have of the order of 10000 spherical mirrors. Testing all of them with the old setup would take over 7 years. Therefore, a new 2f-setup with a drastically reduced measurement time is in development.

4.4.1 General Idea and Goals

The time consuming part of a measurement with the old setup is the scanning with the photo diode over the reflected spot. Therefore, an alternative light detector is needed, preferably one that can detect the whole reflected spot at once. Such an detector is actually already implemented in the old setup: The camera with the screen. But the problem is, that the camera does not distinguish between the light of different wavelengths and UV-light is even totally invisible to it. Therefore, a UV sensitive camera is used and the halogen lamp is replaced with diodes of different wavelengths, including a UV diode. The big advantage of diodes over a halogen lamp is their stability in intensity of their radiated light. A regular exchange of the diodes is not necessary over a long period of time. Thus, it is possible to fix the positions and pointings of the LEDs for every mirror focal length once with high

accuracy and also make the reference measurement just once in a longer time, that needs to be determined. Because neither the configuration of the LEDs nor their radiated intensity is changing significantly, the once measured reference values can be used for a large amount of measurements. This reduces the repeated work for a measurement to mounting the mirror in the right distance to the LEDs and simply taking pictures from the reflected spot. The analysis of the images can be handled by a simple software within seconds.
The cellar of the IAAT has already been occupied by the old setup that needs to be kept operational at any time. Therefore all components have had to be able to be moved aside at any time too. Thus, the new setup have been only provisional and the goal of this thesis has been to determine if and how well the concept of this setup functions and what is needed to make it work with high accuracy and for implementing it into the frame of the old setup.

4.4.2 Setup Configuration And The Single Components

The new setup also uses the 2f method. Figure 4.11 illustrates how it works. Pictures of the setup components can be found in the annex. LEDs are placed at a distance of two time the focal length of the mirror and irradiate it. As light detector a UV-sensitive camera and a Teflon screen is used. They are used for taking pictures of the reflected spot as well as of the light radiated by the LEDs in the direction of the mirror. From the image of the reflected spot the PSF and the amount of light reflected by the mirror can easily be derived. For a reference measurement, the camera and the screen are also placed between the LEDs and the mirror to determine the amount of light incident on the mirror. This is done by projecting the mirror into the (background subtracted) image taken at this position and integrating over the part of the image that is covered by it. The following chapters describe the single setup components, how they function together and what problems and solution from them have been found.

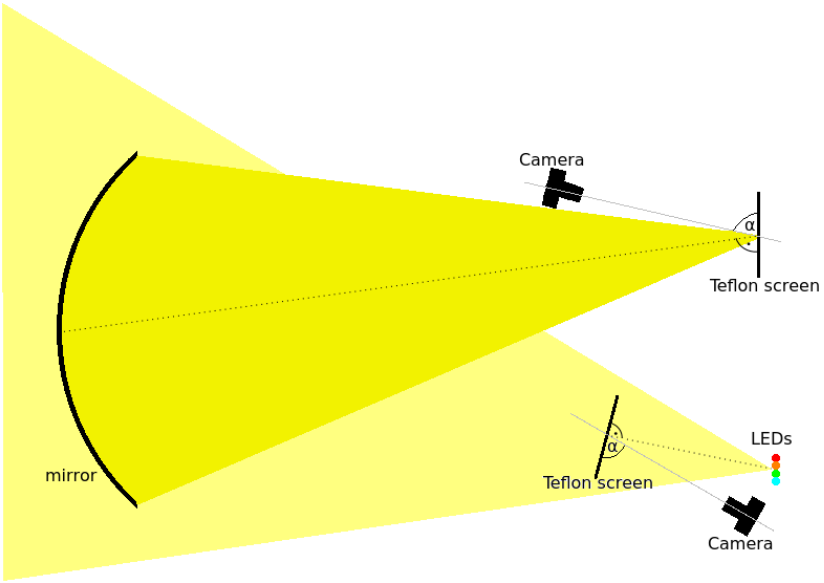

Figure 4.11: Schematic of the new setup: As light source LEDs of different wavelength are used to irradiate the spherical mirror placed two times the focal length in front them. A UV-sensitive camera and a Teflon screen are used as light detector. The configuration of the camera and the screen (angle α and distance) have to be the same for both positions.

Camera and Optics

The Camera is of the typ ALTA U47 from Apogee. For wavelengths above 400 nm and below 700 nm the camera has a quantum efficiency higher than 60%, and in the UV still above 50%. Its CCD consists of 1024×1024 pixel. During measurements the camera is cooled to -20°C with its internal cooling system, to reduce the noise due to dark currents. Via a USB wire it is connected to a Linux pc that runs the control software. Figure 4.12 shows a picture of the camera. The camera is used together with a triplet of UV lenses in a custom made retainer, that set the focus to 3.18 m. At this distance the field of few is 20 cm × 20 cm. Images take with the camera are send in the FITS format to the control PC. These .fits-files include 2 dimensional matrices, with each matrix entry filled with the value of the intensity of the corresponding CCD pixel. All images that are presented in this thesis and were taken with this camera were done in the focus of camera at 3.18 m. The typical exposer time was 3-6 seconds.

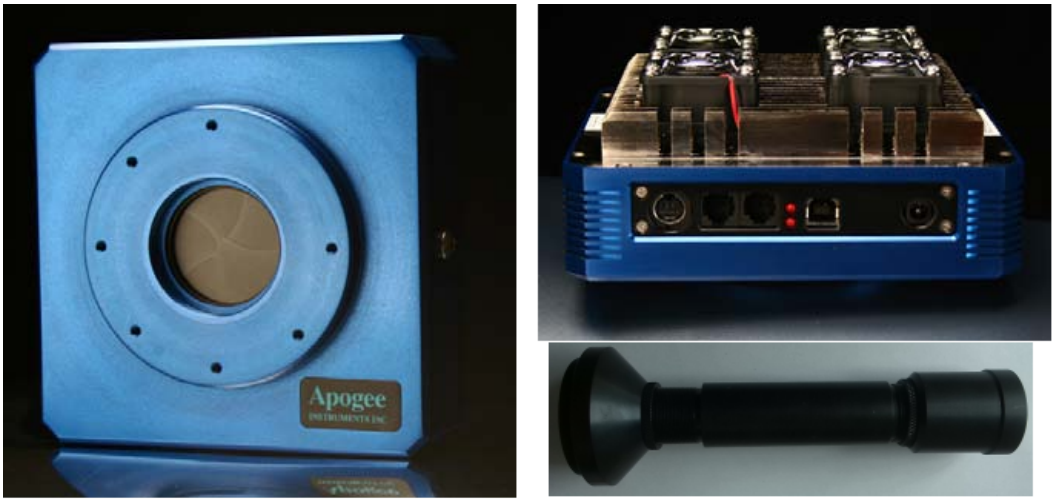

Figure 4.12: Pictures of the UV camera and optics of the new setup.

Teflon screen

As screen it was decided to use a plate made out of Teflon (PTFE). Teflon has a very high reflectivity of over 90% for the whole required wavelength range from 300 nm to 550 nm and above [2]. Furthermore, the behavior of Teflon is close to a Lambertian scatterer, which means nearly all the light reflected by this material is reflected diffusely. Therefore, the dependence of the intensity seen by the camera on the screen should be mostly independent of the angle between the cameras viewing direction and the screen (α in Figure 4.11). The tested and used commercial Teflon plates were cut and polished by the IAAT workshop to smoothen the surface and remove dirt and other materials on the surface. Unfortunately, the quality of the screens is not as high as hoped for and some structures inside the material can be seen in the images. Also, with a thickness of about 5 mm the Teflon plates are easily bending. Furthermore, the thickness of the screen fluctuates over the screens surface up to 8%, and small irreversible deformations are seen even by eye. All tis will lead uncertainties in the measurement presented and discussed later in this thesis.

4.4.3 Taking Pictures With The Camera And Screen

To rate the performance of the camera and the Teflon screen, it is necessary to discuss first, what is expected to be seen in the images made in the different situations of a measurement.

What should be seen

When irradiating the screen head-on with e.g. a laser, a round spot is seen. But when the screen is slowly turned, the round spot is changed and has a complicated shape, making it very difficult to analyze it. Therefore, during a measurement it is most important to always irradiate the screen perpendicular to its surface.
If it is assumed the LEDs are point like light sources, they will radiate light homogeneous in a solid angle 4π. For the reference measurement to determine the amount of light incident on the mirror, the screen is placed between the point like light source and the mirror. On the screen, there will be seen the projection of the spherical light distribution produced by the light source onto the plane of the screen. This is sketched in Figure 4.13.

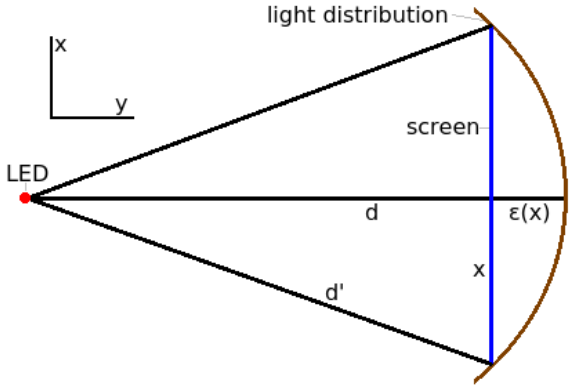

Figure 4.13: The spherical light distribution of a point like light source (LED) is projected into the plane of a screen. The exact intensity seen on the screen depends on the distance x from the center of the screen.

For a distance d between the light source and the screen, the relative change in the seen intensity is equal to the negative change of ϵ. These are given by:

$$\begin{aligned} r &= d + y \\ r^2 &= x^2 + y^2 \\ y &= \sqrt{r^2 - x^2} \\ \epsilon &= y - d \end{aligned} \tag{4.8}$$

For a typical d of 1.5 m and a distance x from the center of the screen of 10 cm (half the field of few of the camera) this makes a change in the intensity compared to the center of the screen of just about +0.3%.
There is second effect producing a radial intensity distribution on the screen. Each part the screen has a different distance to the camera. For the camera viewing onto the screen center and perpendicular onto the screen surface, the difference in the distances to the camera of two points on the screen is simply given as (see Figure 4.13):

$$d' = \sqrt{x^2 + d^2} \tag{4.9}$$

$$\Delta d = d' - d \tag{4.10}$$

Assuming again an x of 10 cm and a d of 3.18 m, this makes a Δd of 0.157 or 0.05%. The intensity is proportional one over the square of the distance. This makes a relative change of the local intensity along d' compared to the center of the screen of -0.31%. Together with the change calculated above this makes a total change of only about 0.01% and thus this effects together are negligibly small.
However, because the camera is not allowed to stand in the path of the light and can not look through the mounting of the LEDs, the viewing direction of the camera will not be perpendicular to the surface of the screen. This leads to two similar effects as described above, but they are not negligible. First, because of the viewing angle of the camera onto the screen, the optical path for the light to reach the different edges of the screen differ. A sketch can be seen in Figure 4.14. The dependency of the local intensity on the screen seen

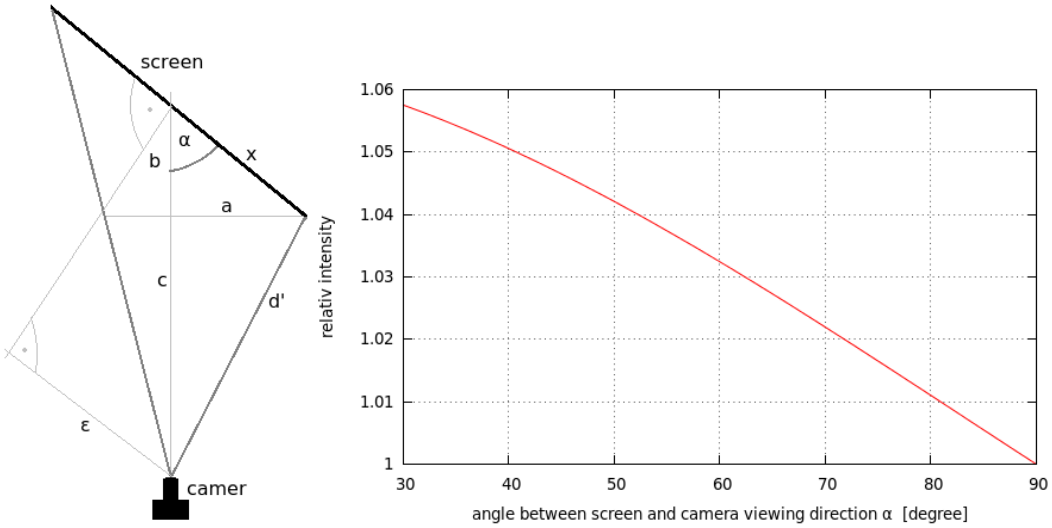

Figure 4.14: left: Sketch to calculate the effect of the different distances of the outer part of the screen compared to screen center, for a viewing angles of the camera onto the screen, that is not perpendicular. Here, c+b is equal to 3.18 m for all α. left: Plot of the local intensity seen at the border of an image relative to the image center. The image center corresponds to the screen center and the image border to part of the screen with a distance of x = 10 cm.

by the camera along d' is again proportional to one over the square of the distance d'. d' is easily calculated as:

$$d' = \sqrt{(\sin(\alpha) \cdot x)^2 + (d - (\cos(\alpha) \cdot x)^2} \tag{4.11}$$

Figure 4.14 right shows the plot of the local relative intensity on the screen seen by the camera normalized to an α equal to 90°. x is assumed to be equal to 10 cm again. The plot shows, that already for α equal to 80° the error is over one percent. Although it only are one percent at the border of the field of view of the camera and integrated over a whole image centered in the center of the screen, the error should be averaged to smaller values, the angle α should still be kept as close to 90° as possible to avoid small errors to add up. Especially since the currently used screens have not the desired quality, the effect described here might add up with the bending and deformations of the screen, as well as with that even Teflon is not a perfect diffuse reflector and a small dependency of the reflected intensity on the reflection angle might me be present.
Furthermore, there is still a second effect. If the viewing direction of the camera is not rectangular to the surface of the screen, the camera will only sees a projection of the actual

light distribution on the screen. E.g., while in Figure 4.14 left a spot might have a diameter x, the object the camera sees only has a diameter a. Assuming the screen is a perfect diffuse reflector and ignoring the effect stated above, the camera sees the same intensity for all angles α on a screen that has the exact same size as the field of view of the camera. But, while for α equal to 90° the screen fills the camera's full field of view, for e.g. 45° it does not. This means all the intensity is projected into a smaller area for any α different from 90° and thus a higher flux of light and smaller PSF measured. Additionally, a to high flux measured in the reference measurement decreases the measured reflectivity
Another way to describe this effect is by what size of an area on the screen is projected into one pixel of an image taken with the camera. Figure 4.15 right shows an image of the screen with a metal ruler in front of it. The images was taken with the camera viewing onto

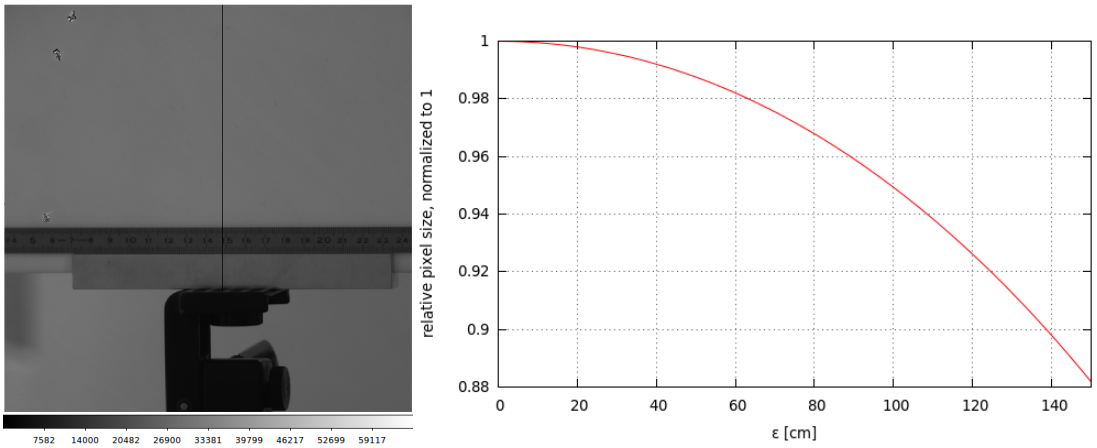

Figure 4.15: Left: Image of the Teflon screen with a metal ruler in front of it, for determine the pixel size. Right: Plot of the change of the pixel size depending on the distance of the camera to the line perpendicular to the screen and piercing through the screens center.

the screen head-on. By simply counting the number of pixels located between two markers on the ruler, the pixel size for head-on images have been determined to be 0.2 mm. The same was repeated with an angle of about 30° between the viewing direction of the camera and the screen. Here, the measured pixel size is about 1.5% higher than before. However, using Figure 4.14 again shows this effect should be much stronger. For a given length x, the corresponding length y in an image can be calculated as:

$$\alpha = \frac{\epsilon}{b+c} + 2\pi \tag{4.12}$$

$$y = \cos[\arccos(\frac{\epsilon}{b+c})] \tag{4.13}$$

Figure 4.15 right shows the plot of this function. ϵ is the distance between the camera and the imaginary line piercing through the center of the screen rectangular to its surface. For an ϵ of 80 cm that corresponds to an angle α of 14.57° the pixel size already decreased 3.2%. The much slower decrease measured by putting a metal ruler on the screen as described above might be cause by the ruler. It was somewhat bent and not flat. Due to optical effects the curvature of the ruler might have compensated the geometrical effect of turning the screen. The pixel size determined for head-on view of 0.2 mm should not have an effect.

The LEDs and first images

As a light source for the new setup LEDs are used. The advantage of the LEDs over the halogen lamp are their high stability in the radiated light flux over a long time periods and that they radiate only in a narrow wavelength-band. Because the narrow band no filters have to be used and the high stability might make reference measurements unnecessary for a long time periods in a final version of the setup where the camera, when the screen and the mirror have fixed position that will not be changed.
Two different LEDs where mainly used for all tests. For one, a 4-color-LEDs consisting of four LEDs of different wavelength on one chip under a common optical grade 5 mm diameter lens. Figure 4.16 left shows a picture of such a combined LED. The peak wavelength of each LED depends of its temperature and can vary:

- blue: 455 - 460 nm
- green: 530- 535 nm
- amber: 585 - 595 nm
- red: 620 - 630 nm

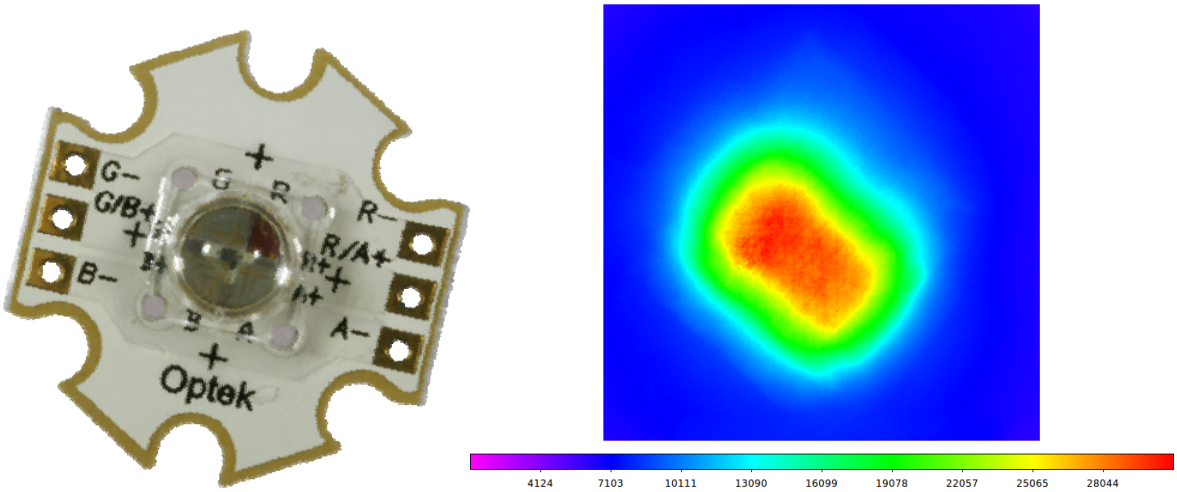

Figure 4.16: left: Picture of the 4-color-LED with its 4 LEDs on one chip and a common lens. right: Image of the light distribution on a Teflon screen irradiated head-on by the uv-LED. The distance of the uv-LED to the screen was about 1.36 m.

In addition to the 4-color-LED a uv-LED (315 nm) with a collection lens was used. The collection lens is necessary, because uv-LEDs are not as luminous as LEDs of higher wavelength. By concentrating the light with a lens a high enough light flux for a measurement is reached, but the light cone is very narrow. Figure 4.16 right shows an image of the light distribution on a Teflon screen irradiated head-on by the uv-LED from a distance of about 1.36 m. The light spot has somewhat rectangular shape with a distance between the two longer sides (intensity decreased to 50%) of about 430 pixel or 8.6 cm on the screen, respectively. Projected into the image of uv-spot, a SST mirror has a diameter of 13.3 cm flat to flat and thus can not be irradiated uniformly. If during a measurement a mirror is not uniformly irradiated, the measured reflectivity and PSF will be dominated by the quality of the parts of the mirror irradiated with the higher intensities and not represent the whole mirror. A

solution to this problem would be to implement several uv-LEDs with different lenses which are used according to the focal lengths of the mirrors.
There is a similar problem with the 4-color-LED as for the uv-LED. Figure 4.17 shows the light distribution of the red color on a Teflon screen irradiated head-on from a distance of about three meters. Along the black line the intensity decreases 20% over 1024 pixels

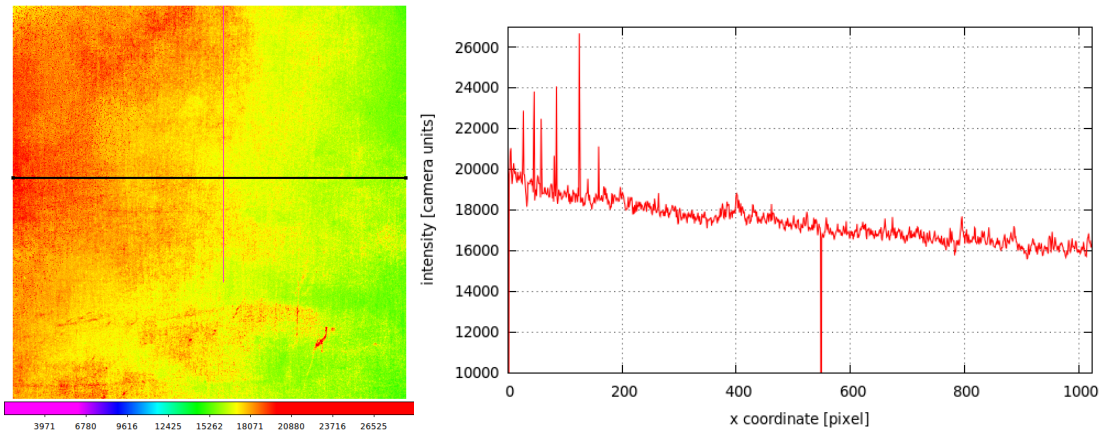

Figure 4.17: left: Image of the light distribution on a Teflon screen irradiated head-on by the 4-color-LED (red) from a distance of about three meters. right: Profile of the light distribution along the black line. The spikes for x smaller 200 pixel is probably caused by some kind of dust grains with higher reflectivity than the Teflon on the screen.

corresponding to 20.48 cm on the screen. An SST mirror projected into the image has a diameter flat to flat of 29.25 cm. This means the light intensity on the mirror surface differs up to 30% from one side to an other. Due to its much longer focal length, the projection of an MST mirror into the image has a diameter of only 5.63 cm. Here the intensity differs still up to 5.5%.
In Figure 4.17 left it seem like the maximum of the 4-color-LED lies somewhere top left and maybe not on the screen. If the maximum were centered in the field of few of the camera, the intensity should decrease equally on all sides, but only over a length of half the field of few and this the maximum difference half the value as before. So, it would be obvious to try to aim better with the LED onto the screen. However, the real problem is not the aiming but the one common lens for the 4 LEDs on the same chip. All 4 LEDs are not placed in the center of the lens, but around it. Thus, their light is focused in different direction. The angle between the maxima of two colors was roughly tested by placing the 4-color-LED in front of the photo diode, turning it and observing how the intensity measured by the photo diode is changing. As result, the angle has been estimated by eye to be even larger than 45°. This makes it impossible to properly aim with all 4 colors from a fixed position for the LED. Furthermore, the focusing lens is changing the optical path of the light, producing a virtual light source further behind LEDs. In a measurement with the new setup, this might produce an uncertainty in the distance of the Mirror to LED of only a few millimeters and seem to be insignificant compared to two times the focal length of at least 11.2 m (SST mirror). However, for the reference measurement, precisely measuring distances turned out to be very important and a large source of uncertainty in the measured reflectivity, due to the strong dependency of the light flux of one over the square of the distance from the light source. This will be further discussed in section 4.4.4. Because of the problems with the 4-color-LED, it was decided to search for better an alternative, like single color LEDs. Unfortunately, only one single color LEDs with a wavelength of 450 nm was available and operational for test.

Figure 4.18 shows the results of the same measurement as for Figure 4.17, but with the single color LED. Here, in horizontal direction, along the black line, the intensity is changing less

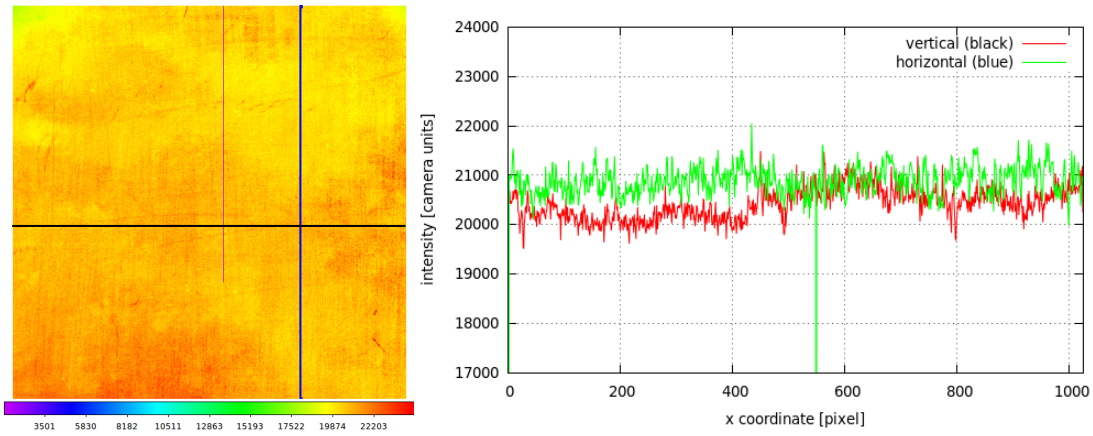

Figure 4.18: left: Image of the light distribution on a Teflon screen irradiated head-on by the single color LED from a distance of about three meters. right: Profile of the light distribution along the black line.

than 1% in average over the fluctuation. In vertical direction it is still around 5% from top to bottom (1024). However, this is at least partially caused by the orientation of the screen towards the camera. Only the bottom side of the screen was fixed to the mounting and under its own weight the screen always tends to slightly bend or tilt, and in case of this measurement bend away from the camera. Nevertheless, this shows the light distribution produced by the single color LED is much better than for the 4-color-LED. However, the more homogeneous illumination of the screen revealed more problems of it.
The fluctuations in the intensity over just a few pixels are caused by scratched on the screens surface or can be due to the not flat fielded camera. The large spikes in Figure 4.17 right, are caused by some kind of dust grains with higher reflectivity than the Teflon. They overlay with fluctuations over several tens to 200 pixels which are cause either by deformations or the variations of the thickness of the screen. The later one can mean variations of the local reflectivity across the screen, but also slight variations in the orientation of the screen section toward the LED and camera. All of this leads to a dependency of the intensity seen by the camera on the observed part of the screen.
During test measurements with the new setup it was observed, that the measured intensities for identical setup configuration were time dependent. This had two reasons. Fist, the magnitude of background light and its variations where underestimated. A better sealing of the windows solved most of the problem, but further improvement are needed. Second, the luminosity of the LEDs is temperature dependent. When they are switched on, they are at room temperature, but because of their electric resistance they are heated up by the currents flowing through them. This also has an effect on the actual resistance the LEDs have. Depending on the used electronics and power source, this changes their luminosity. This was measured for the 4-color-LED and also single color LED for a power source that supplied a constant current and another power source that supplied a constant junction voltage to the LED. For this measurements the LEDs were placed in front of the photo diode of the old setup again with the chopper wheel in front of them and the photo diode set to continuously measure. Then the LEDs where started at room temperature with prior set currents of 50 mA, 100 mA and 150 mA. Also, the provided (start) currents were changed for the already running LEDs with stable luminosity and thus temperature. Figure 4.19 shows

some exemplary results for 3 colors of the 4-color-LED for each power source. The starting

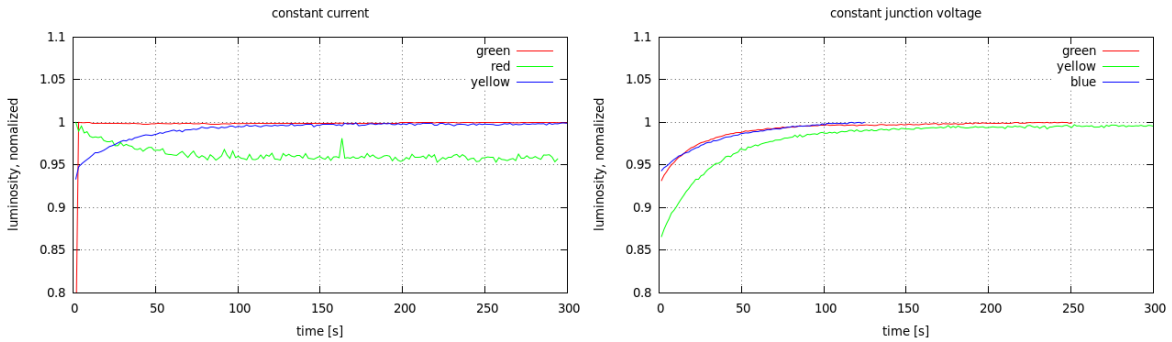

Figure 4.19: Normalized luminosity of the different colors of the 4-color-LED for a power source supplying a constant current (left) and a constant junction voltage (right) vs the time after power-up. The LED was provided with a starting current of 100 mA and started at room temperature. After the power-up the LED is heated up by the electric current and changing its luminosity. This characteristic of the LED depends on the used color and power source.

currents were always set to 100 mA and the starting temperature at room temperature. The results show, that the behavior of LED is not only determined by the used power source. For a constant current the luminosity of *red* is decreasing while it is rising for *yellow* and *green* shows only a very small decrease. However, for a constant junction voltage *green* shows the same strong rising behavior as blue. *Yellow* seem to rise slower as the other colors, but that might be a matter of a wrong used time scale. The photo diode and lock-in amplifier do not produce data points in constant time intervals. However, the average time between two data points stays constant for longer time periods of several minutes or longer, but was also observed to change during a measurement. The average time between data point was checked at the beginning and end of a measurement for one LED (color) and starting current, but there is still the possibility of strong fluctuations in between that were overseen.
While the PSF measurement only depends on the light distribution of the light reflected by the mirror and thus is not sensitive to changes in the luminosity of the light source, the measured reflectivity is. It is calculated as the amount (or flux) of light reflected by the mirror divided by the amount of light incident on the mirror. Both are measured in different positions in the setup and thus at different times. If the luminosity of the light source changes in between these measurements, e.g. for 3%, the error in the measured reflectivity is also increased for 3% of the true value. To prevent this, after switching on an the LED, at least 5 minutes have been waited for the LED to thermally stabilize before measurements was started. In a full mirror measurement, this of course had to be done for all colors, resulting in a total waiting time of 25 min (5 colors).
All LEDs are expected to have a high long term stability in their luminosity, but this has not been tested yet. One idea for a final version of the new setup is to constantly observe the LEDs with the help of optical fibers and a light detector, e.g. a photo diode or the camera of the setup, and , when necessary, to adapt the reflectivity measured with the new setup according to the observed changes in the LEDs luminosity. With this, the reference measurement has to be done only once for each configuration of the setup and does not have to be repeated in every single measurement of a mirror during a long testing campaign.

4.4.4 A Full Test Measurement

In previous sections the most important parts of the new setup have been presented and discussed. Still mot presented are a tube with an iris from an optical bench and curtain. The tube with iris is placed in front of the LED to reduce the stray light. The curtain is placed between the LED and the screen-camera configuration at the position to measure the reflected light spot, also to reduce stray light and to prevent the LED from directly shining into the camera. See Figure 4.11 to get reminded on the configuration of all the parts again, because now a full test measurement with the new setup will be presented, analyzed on the precision and problems discussed.

Measurement proceeding

The used mirror is a prototype for MSTs and thus has a focal length of 16 m. After placing it at a distance of two times the focal length from the 4-color-LED, the tube with iris set in place in front of the LED as such that the whole mirror was still completely illuminated, but as much stray light as possible prevented. Then, the led was replaced by a laser, that was aimed through the iris onto the center of the mirror. At the mounting of the tube with iris there is another fixed laser, pointed onto the center of the mirror, too. Now the Teflon screen was placed about 1,5 m in front of the laser (*reference measurement position*) and an image of screen was taken with the camera, that was moved with the screen and put in a distance of 3.18 m to it. Next, the 4-color-LED replaced the laser behind the tube again, is switched on and another image taken with the camera still standing in the exact same position as before. Afterwards, the screen was placed in the nominal focal plane of the mirror (*reflected spot position*) and an image was taken from the reflected light spot with the camera. Here, the configuration of the camera and screen has been kept the same as for the image of the light distribution in front of the camera. Now the color of the LED was changed and everything done in revers. For the third color the reference measurement was done first and for the fourth color everything reverse again.
During all 4 runs, the distance of the screen to LED was measured and after changing the LED color 5 minutes waited for the LED to thermally stabilize. For every set of images of the light of the LED or the reflected spot, there have been a set of dark images taken which are subtracted from the bright images. This eliminated influences from stray light, background light and also effects of dark currents in the electronics that produce a minimal measured intensity (noise).

Analyzing the images: PSF

From the averaged and background subtracted images taken at the reflected spot position the PSF is derived. A self-written c-program transforms the pixel values of the image started in the .fits-file into a two dimensional array (like a matrix), with each array element representing one pixel. Then the center of mass of the whole image is determined. It is used as center of a circle, with a diameter of 500 pixel, of which a new center of mass is calculated. This is repeated several times with circles of smaller and smaller diameter. A circle with 1 mrad radius (160 pixel for MST mirrors) is used define the light containing it as 100% of the light reflected by the mirror. By simply integrating of circles with bigger and bigger radius until the contained light is a least 80% of the reflected light the R80 is determined.
Measuring the PSF is simple. The only difficulty is to put the screen in the exact right distance to the mirror and as such that the virtual line from the mirror center onto the screen is perpendicular to its surface. Otherwise the reflected light spot will be enlarged and

deformed. Figure 4.20 shows an image of the reflected spot of the measured MST prototype mirror.

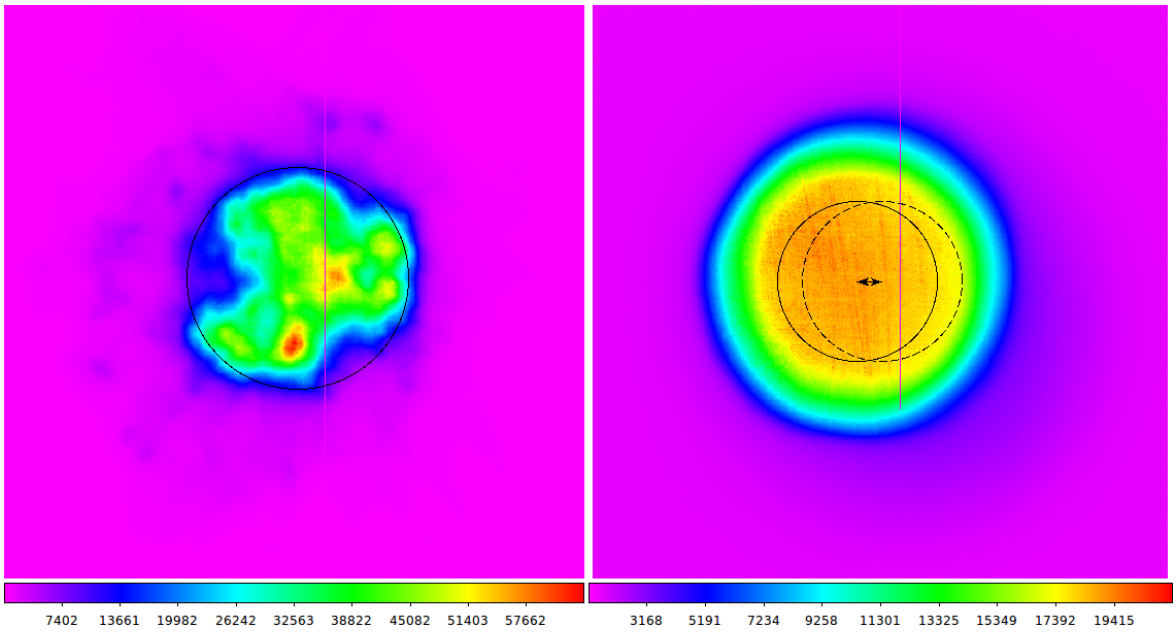

Figure 4.20: left: Image of the reflected light spot for the color *red* of the 4-color-LED and prototype mirror for MSTs. The black circle represents the measured PSF (R80). right: Image of light distribution of the 4-color-LED for *red* at the reference position on the Teflon screen in a distance of 1.48 m to the LED. The round shape is produced by the iris with a diameter of 6.3 mm, located about 10.8 cm in front of the LED. The dashed circle is located around the center of the MST mirror projected into the image plane and has the same diameter as this projection flat to flat. The black arrow indicated the distance of the two circles centers.

Analyzing the images: reflectivity

To determine the reflectivity, the amount (or flux) of the reflected light and the light incident on the mirror is needed. The first is determined by a circle with a 1 mrad radius in the image of the reflected spot, the second is the tricky part. For the first measured LED color, at the reference position two kind of images have been taken. One contains the light of the LED, the other one the two lasers pointed at the center of the mirror. The laser aimed through the tube and iris gives the information where the virtual line connecting the LED and the Mirror center lies in the image plane. After the reference measurement, the camera has to be moved to the reflected spot position and it is not possible to later put the camera back into the exact same position, that the cameras field of view is identical to before. The second laser marks a common spot for all images taken at the reference position with which the virtual line connecting the LED and mirror center, marked by the other laser in the image of the first used color, can be found. To now determine the amount of light incident on the mirror, the mirror is projected into the image of the LED light distribution, taken at the reference position. Simply with the theorem of intersecting lines, the size w_i of the hexagonal mirror in the image plane can be calculated:

$$w_i = \frac{w_0}{2f} \cdot d \tag{4.14}$$

w_0 is the size of real mirror, e.g. a diameter of 1.2 m flat to flat for MST mirrors, f is the focal length and d the measured distance of the LED to the screen. Since the shape of the mirrors is of a regular hexagon, it is completely defined by w_0 alone. What is still missing is the information where the center of the projected mirror is. In theory, it is simply given by intersection of the virtual line connecting the LED with the mirror center. In practice, there are several complications leading to a lot of uncertainties in the exact location of the intersection. For one, the location of the laser aimed trough the iris can not be 100% reproduced when it is exchanged with the LED. Assuming the LED is misplaced for 0.5 cm and the screen has a distance from the LED of 1.5 m, this results in distance of the center of the projected mirror to the spot marked by the laser of 4,8 mm or 24 pixel, respectively. In addition, the laser spot on the screen has a finite size and perfectly aiming on the center of the mirror is difficult with the current equipment. This results in an uncertainty of at least 15 pixels for one laser spot. For the two laser spots, used to find the intersection, together this makes at least 30 pixels. Summed up, this makes an uncertainty of ± 54 pixels of the location of the intersection in all directions.
Figure 4.20 right shows an image taken at the reference position for the color *red*.The dashed black circle indicates the position of the measured hexagonal MST mirror projected into the image plane, determined by the two lasers, and the diameter of the circle is equal to the diameter (flat to flat) of the projection. While reducing stray light a lot, the iris with a set diameter of 6.3 mm is producing the circular shape of the light distribution in the image and thus potentially increasing the uncertainty in the determined light intensity incident on the mirror. If the configuration of the setup had been perfect, the projection of the mirror (dashed circle) would have been located in the center of the light distribution, like the solid circle in Figure 4.20. Obviously this is not the case. The projection (dashed circle) is close to the edge of the light distribution where the intensity falls off. Thus varying the position of the projection can have a big impact on the determined amount of light incident on the mirror. Since the position of the projection has an uncertainty of ± 55 pixel (or maybe even higher), the uncertainty in the amount of light incident on the mirror can be of the order of 10%, too.

Results of the measurement

Figure 4.21 shows the results of the measured PSF and reflectivity for all 4 colors of the 4-color-LED and for comparison the result with the upgraded old setup, as well as a hand reflectometer measurement on the same mirror, too.

The precision of the measurements is determined by the errors made as already described in the section before. They sum up to the error bars seen in Figure 4.21 right and consist of the following parts:

- Camera-screen configuration: The Camera had an angle of about 12.2° to the screen (α in Figure 4.11). According to Figure 4.15 ($\epsilon = 67$ cm) this results in a decreased pixel size of about 2.2%. This applies only in the horizontal direction. An uniform hexagon can be formed out of one rectangle and 4 equal triangles and therefore the correction has to be applied linear.

- Distance measurement: The measured distance between the LED and screen at reference position determines the diameter of the projection of the mirror into the taken image. This dependence is linear. However, the area contained by the hexagonal projection is proportional to the square of its diameter. Furthermore, the error depends on the distribution of the intensity. As approximation a homogeneous distribution is

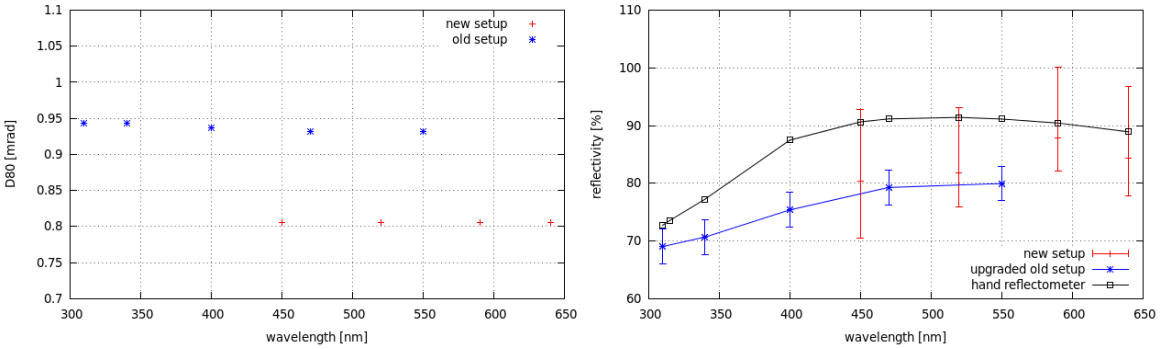

Figure 4.21: left: The PSF values measured with the old and the new setup for different wavelengths for an MST mirror. right: The reflectivity values measured with the old and new setup for different wavelengths.

assumed. This results in an error proportional to the square of the error of the measured distance. The precision of the measured distance is estimated as ± 1 cm. For a distance of about 1.5 m this makes a relative error of ±4.44% on the measured amount light incident onto the mirror.

- The location of the projection of the mirror into the images of the reference measurement is determined with an error. To determine the impact of this error on the measured reflectivity, which depends on the light distribution in the reference measurement and the aiming of the laser and LED, the reflectivity was calculated for different centers of the projection in 10 pixel steps for ±50 pixels in both image direction. The exemplary result for red can be seen in Figure 4.22. Here, the measured reflectivity coefficient varies [-0.013,+0.082] or [-1.55%,+9.7%]. The plots of the results of the other three colors can be found in the annex. The determined error for blue, green and yellow in order are: [-0.11%,+11.38%], [-0.61%,+9.41%], [-5.60%,+11.08%].

The PSF measured with the new setup has the same value for all 4 colors of the 4-color-LED. This value is more than 10% smaller than the value measured with the old setup. Both is expected, because the size and shape of the reflected spot is determined by the quality of the shape of the mirror and thus not depending on the wavelength, and the old setup is not using the center of mass but a point chosen by eye for calculating the PSF.
The large discrepancy between the reflectivity measured with the old setup and the hand reflectometer of up to 12% is surprisingly high, but may be a result of a bad mirror quality. It was expected that both measurement only differ by an offset and do not differ in their behavior. This might be caused by how the average of the mirror was calculated for the hand reflectometer. The density of the measured points per area was higher in the center of the mirror than on the outer parts. This means the inner parts, which have a lower reflectivity in the lower wavelength, might have been overweighted and produced the seen behavior. However, for wavelengths about 550 nm it can be assumed that the values measured with the old setup, if the right filters available, would follow the behavior of the hand reflectometer and decrease the same way.
Since the new setup is using the 2F-method, it should reproduce the measured values of the old setup and their (guessed) extrapolation according to the behavior of the hand reflectometer values. For 450 nm and 520 nm the values measured with the new setup are just about 2% above the guessed extrapolated values of the old setup. The hand reflectometer measurement decreases from 550 nm to 640 nm about 1.2% and assuming the values of the old setup follow

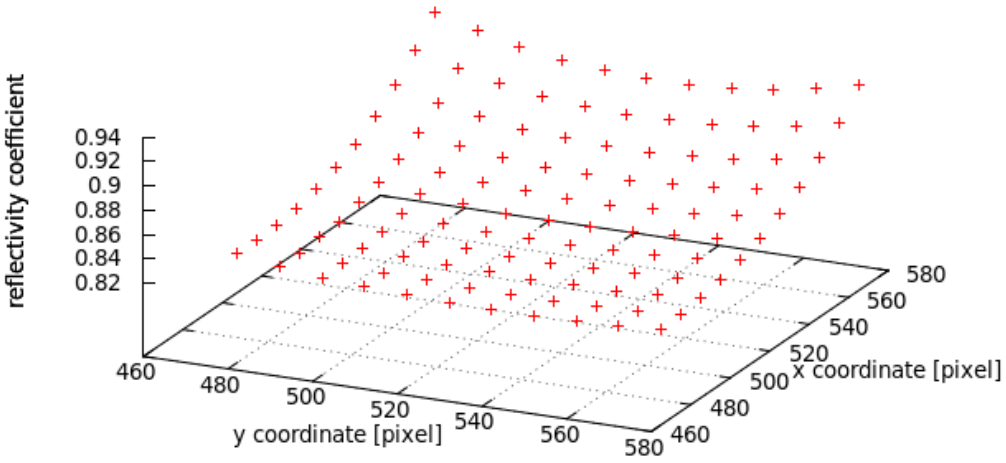

Figure 4.22: Results of the measured reflectivity for *red* of the 4-color-LED. The center of the projection of the mirror into the images of reference measurement are shifted ten pixel wise up to a total of ±50 pixel, around the position measured with the lasers at (517,529).

this trend exactly, they would decrease to 78.7%. The lower error bar of the value of the new setup for 640 nm ends at just 1.3% below this value and thus still includes it. For 590 nm the error bar of the new setup does not include the guessed extrapolation of the old setup. However, the errors made with new setup might be underestimated. For example, it might easily be, that for 590 nm, but also 640 nm, the distance of the screen to the LED during the reference measurement has been measured worse than expected in the error calculations. Anyway, this and the large size of the error bars are due to the provisional state of the new setup and thus not surprising.

4.4.5 Further Test for Improvements

The measurement presented above, is just the last full test measurement done. There have been several tests done on how to improve the performance of the new setup and its components, respectively. Two have been already shown in the previous section:

- The single color LED with a much better, more homogeneous light distribution. If additionally a larger iris with a diameter of about 1 cm is used, the location of the center of the mirror projection into the image taken at reference position is much less crucial than before, due to smaller variations in the intensity over the relevant part of the image.

- The measurements on the LEDs behavior after switching them on for two different power sources (constant current and constant junction voltage). These test have been done with the idea to somehow time the LEDs with the camera to be able to reproduce the same light intensity without waiting for the LED to thermally stabilize.

Additionally there have been done the test following.

Improvements on the screen

As seen in Figure 4.18 left, the screen is not very satisfying with its rough surface and the deformations under its own weight. Therefore a second screen has been polished more and stabilized with a metal frame. Figure 4.23 right shows an image of the improved Teflon screen irradiated head-on with the blue single color LED from a distance of about three meters. The

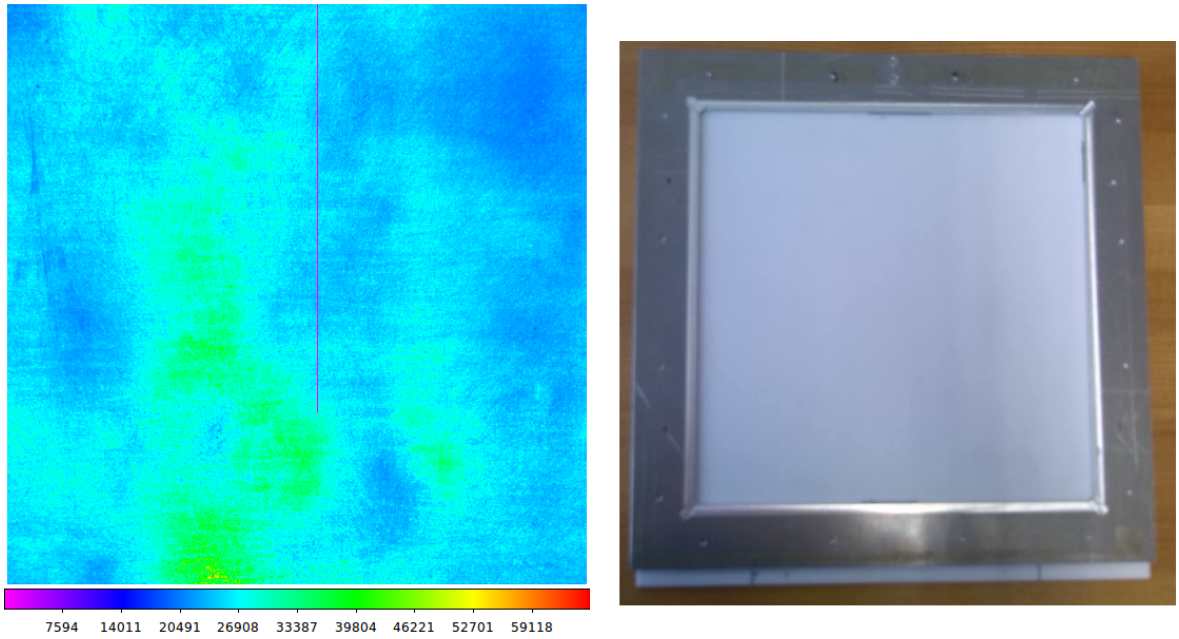

Figure 4.23: left: The light distribution of the blue single color LED on the new Teflon screen. It is expected to me mostly uniform, but shows strong local variations in the intensity of about 25%. right: A picture of the backside of the new Teflon screen.

performance of the improved screen is not very satisfying. While more polishing seems to reduce the seen scratches, the seen internal structures, like to the left of the image in the blue area, are not reduced. Furthermore, the screen shows the cyan area located a little to the left of the image center and extending from the bottom to nearly the top of the image. There the intensity is about 25% higher than in the blue areas around it. This cyan structure might be produced by a deformation of the screen. If this were the case, the metal frame might be retaining the screens bad shape or even enhance it. Additionally, the frame is increasing the weight of the screen and thus make it more likely to tilt in the current mounting.

Influence of the LED lens

As already mentioned before, the (collecting) lenses of the LEDs are influencing the optical path of the radiated light and producing a virtual light source behind the LED. This is illustrated in Figure 4.24 left. To find out how strong this effect is, two reference measurements with different distances of the screen to the 4-color-LED were done. The taken images look similar to Figure 4.20 right. In three dimensions, the light going through the iris is forming a cylinder. The idea was to measure this cylinder at two position, hence the two images, and interpolate the cylinder back to its tip where the virtual light source should be located. As first attempt, the light flux in the two images was determined. The flux is decreasing with one over the square of the distance of the screen to the LED and thus it can be calculated the position of zero distance. Due to the dependence of the flux on the square of the distance, this lead to too large uncertainties, because the distance could not be measured very

precise. Therefore, second attempt, the diameter of the light distribution in the images was determined, as it has only a linear dependence on the measured distances. The problem here is, that the distribution in the images are not of optimal circular shape and actually not of a good elliptical shape either. Additionally, the light distributions do not have any nice features easy to identify and determine, due to the quality of the screen. This can be seen in the shown exemplary profile of such light distribution in Figure 4.24 right. Nevertheless, the measurements indicate that for the 4-color-LED the virtual light source is located one to two cm behind the LED, which is not negligible. When a better screen and better LEDs are available, this test needs to be tried again to get reliable numbers.

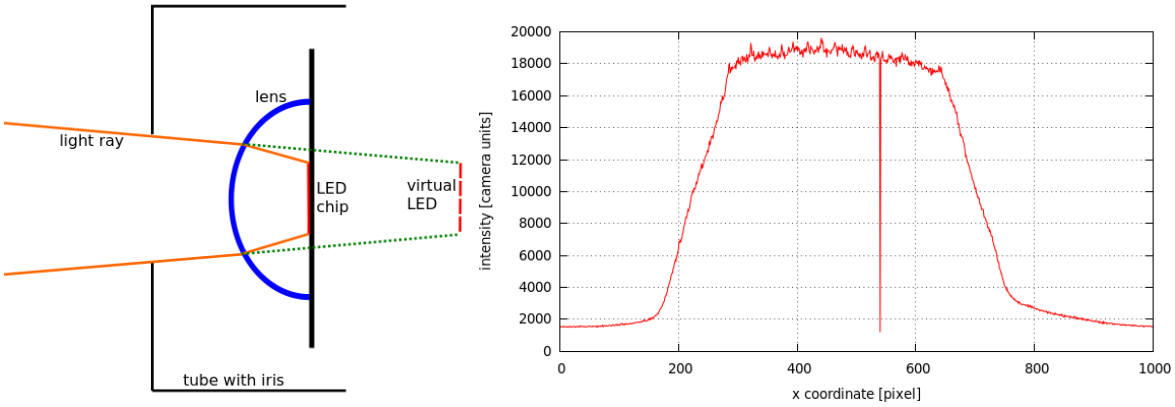

Figure 4.24: left: Sketch illustrating the position of a virtual LED behind the real LED due to the focusing of the lens. right: Profile of a light distribution to determine the location of a virtual light source produced by the lens.

4.5 Summary

The old mirror testing setup developed and built by the MPIK Heidelberg and operated by IAAT had shown a pattern in the measured PSF and reflectivity, which might have been produced by the light filters. After some upgrades, like the replacing the old light filter with new ones of the same kind and from the same producer, the patterns seem to have disappeared [2]. There is a discrepancy between the wavelength dependent behavior of the reflectivity measured with the old setup and the hand reflectometer, but can be explained by overweighting the inner parts of the measured mirror in the averaging over the single mirror points measured with the hand reflectometer. The values for each single points were weighted equally, but the more points measured in the center of the mirror than at the outer parts. The new setup is measuring a constant PSF for all wavelengths with lower values than that of the old setup, as it was expected, and in a time of seconds. Measurements of the reflectivity are of the right order, but still have high uncertainties. This, as well as the still long duration of a measurement of about 30 min for one wavelength (LED), is due to the provisionally state of the setup and the necessary reposition of the camera and screen during the measurement and the resulting need of configuring everything anew for each wavelength. Hence, there is still a lot of room for improvements like a better screen, the use of LEDs that can irradiate the mirrors more homogeneous, e.g. the presented single color LED, and a precise configuration of the setup parts in fixed locations.

[2]The writer of this thesis has not been involved in the upgrading of the old setup and is not claiming any contributions

The LEDs need more tests on the longterm stability of the radiated intensity and on the effect of the lenses. Furthermore, the behavior of the seen intensity and the pixel size with different angles of the camera to the screen need to be investigated with more precision.

4.6 Outlook

The next step for the new setup is the planned implementation into the frame of old setup. When the parts of the new setup do not need to be removable at any time anymore, a precise and time consuming configuration is worth the time and by this alone the precision of the measured reflectivity would should a lot. Additionally, the use of better materials and parts, like single color LEDs and thicker Teflon screen of higher quality will make a good configuration easier and should even increase the setups precision further. Furthermore, an implemented setup would save a lot of time for each measurement. If at some point the reference measurement does not need to be constantly repeated and the power-up of the LEDs precisely and reproducible timed, a full measurement of a mirrors PSF and reflectivity in multiple wavelengths will just be a matter of minutes.

Chapter 5

Annex

Pictures of the actuator test setup

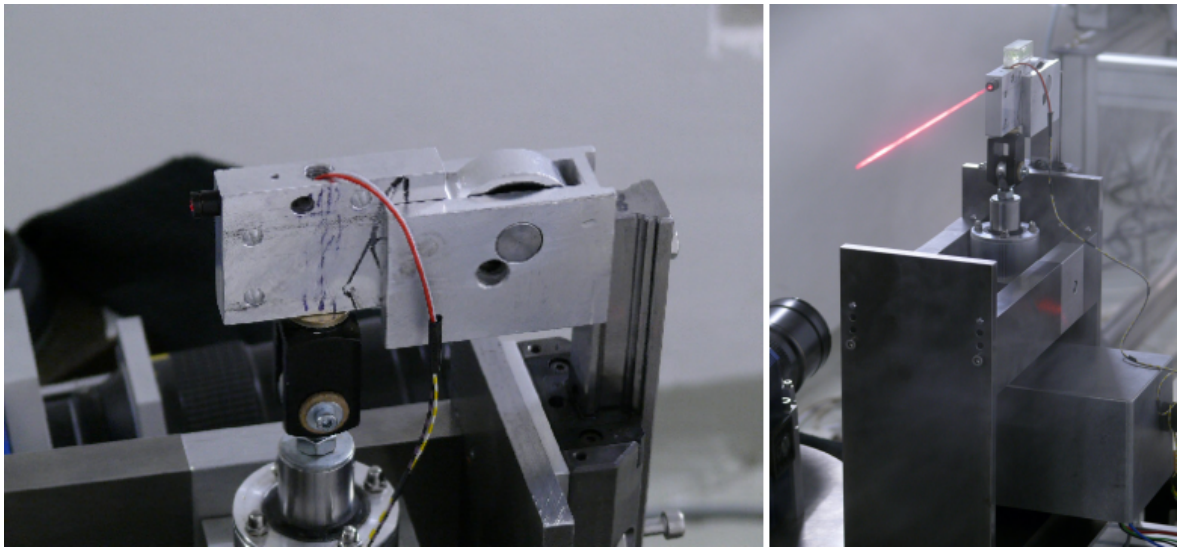

Figure 5.1: Pictures of the setup to test the linearity of the actuators.

Plots of the actuator tests

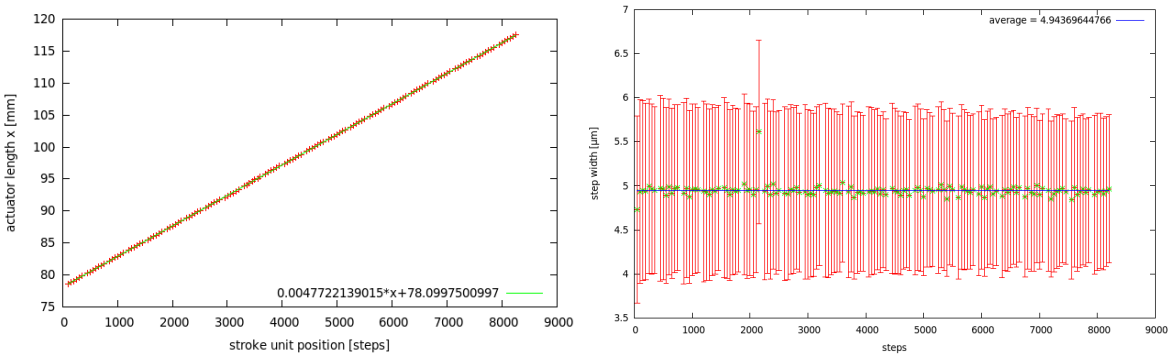

Figure 5.2: An example of results of the longitudinal precision and linearity tests for 30kg weight load pressing on the actuator and moving the stroke unit outwards.
left: Calculated actuator partial lengths x vs the position of the stroke unit in steps. The green line is a linear fit to these values, done with method of the least χ^2. The steepness of the fit is the measured step width in μm.right: Step width Δx between two neighboring data points divided by their difference in position (about 50 steps). Plotted vs the position of the larger data point. The blue line shows the average of single step widths

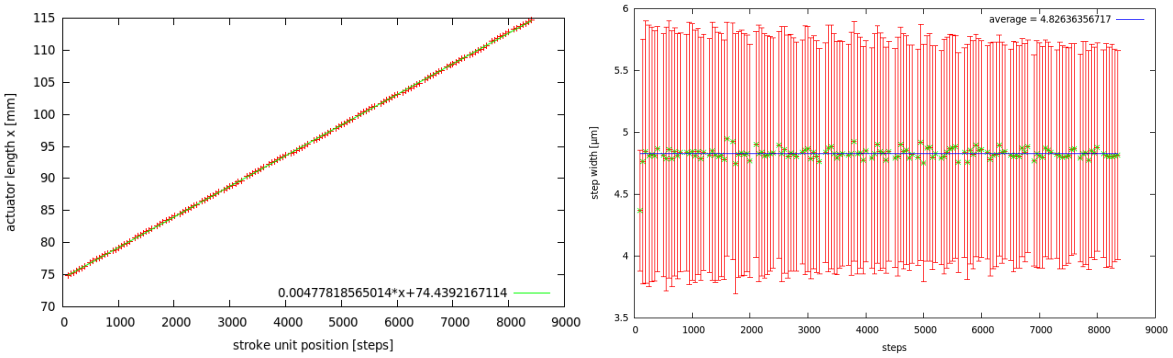

Figure 5.3: The same as Figure 5.2, but for 10 kg, pushing and outward.

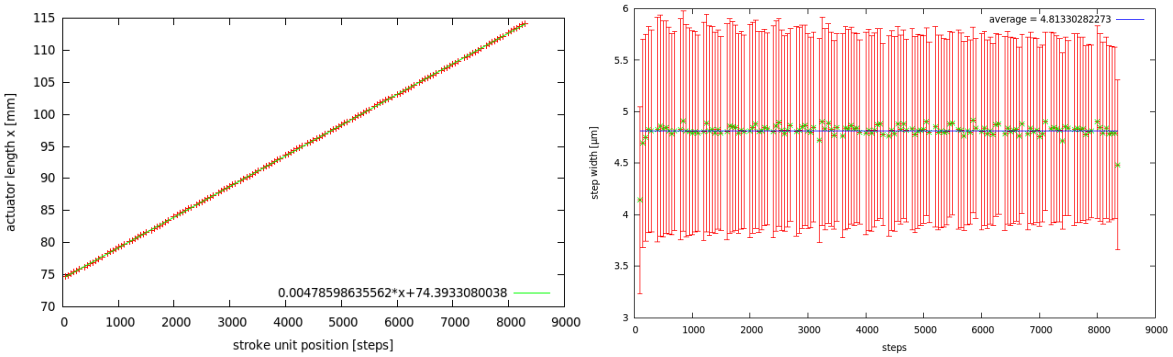

Figure 5.4: The same as Figure 5.2, but for 10 kg pushing and inwards.

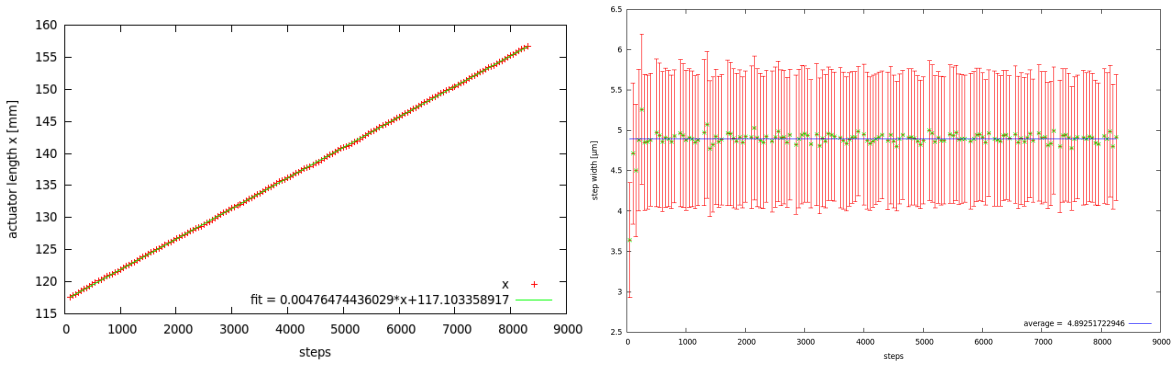

Figure 5.5: The same as Figure 5.2, but for 30 kg pulling vertical and outwards.

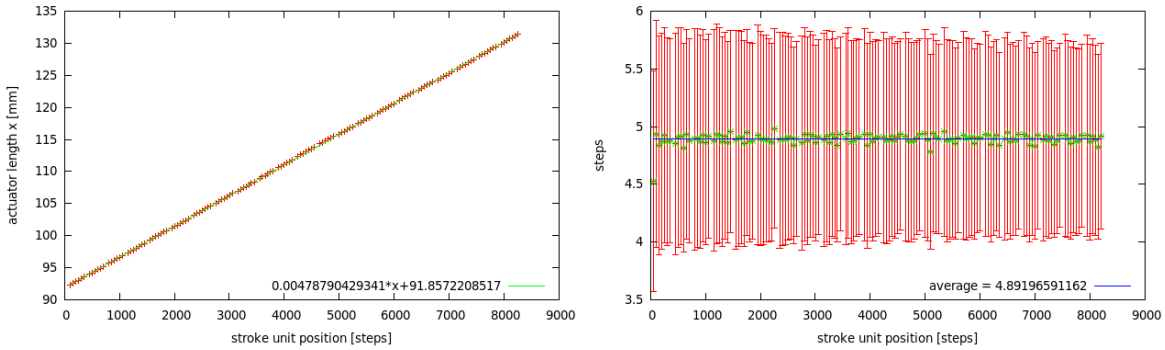

Figure 5.6: The same as Figure 5.2, but for 30 kg pulling upwards and moving outwards.

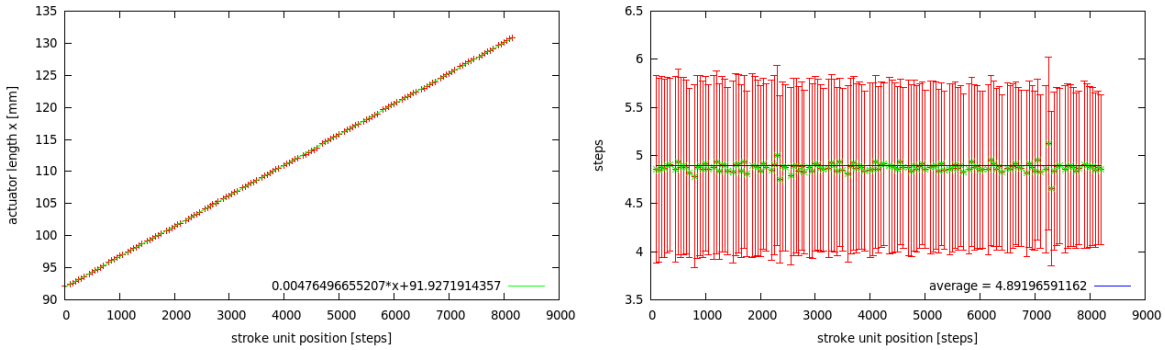

Figure 5.7: The same as Figure 5.2, but for 30 kg pulling upwards and moving inwards.

Changes to the source code of sim_telarray

sim_imagin.c, line 1719:

$$doublerg = ((RandFlat() - 0.5)/0.5 * rang_h) + (0.001 * 2. * 3.14159265359/360.); \\ //RandGauss(0., rang_h);$$

sim_imagin.c, line 1719:

$$doublerg = ((RandFlat() - 0.5)/0.5 * rang_v) + (0.001 * 2. * 3.14159265359/360.); \\ //RandGauss(0., rang_v);$$

Pictures of the new setup

Figure 5.8: Pictures of the components of the new mirror testing setup. 1: The tube with the iris that is positioned before the LEDs. 2: The 4-color-LED. 3: The UV-Led. 4: A laser. 5: The mounted and used Teflon screen. 6: The upgraded Teflon screen. Not in the picture: The Camera.

Images of the light distribution of the remaining 3 colors of the 4-color-LED irradiating the screen head-on

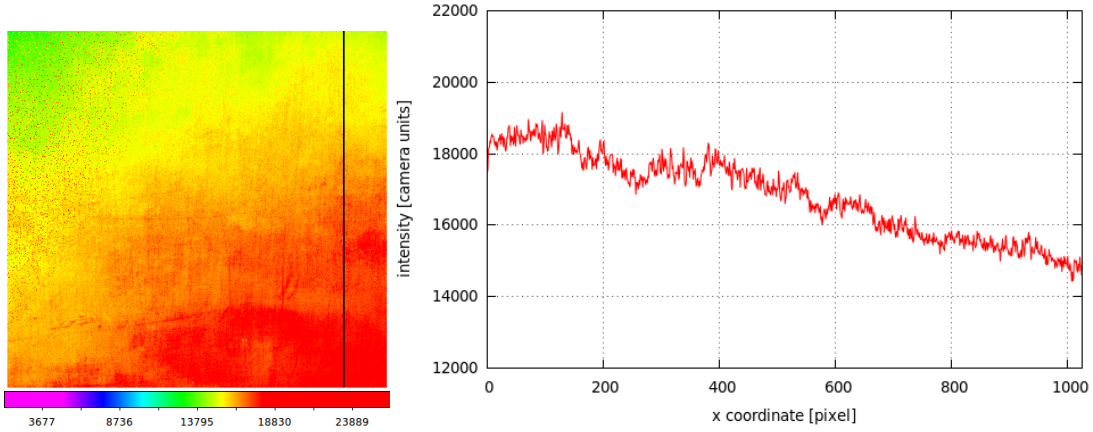

Figure 5.9: left: Image of the light distribution on a Teflon screen irradiated head-on by the 4-color-LED (blue) from a distance of about three meters. right: Profile of the light distribution along the black line.

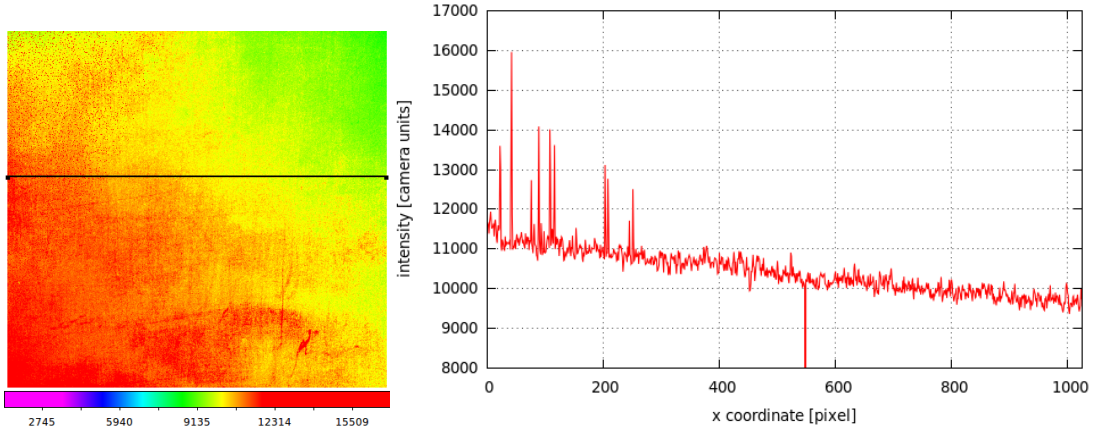

Figure 5.10: left: Image of the light distribution on a Teflon screen irradiated head-on by the 4-color-LED (yellow) from a distance of about three meters. right: Profile of the light distribution along the black line.

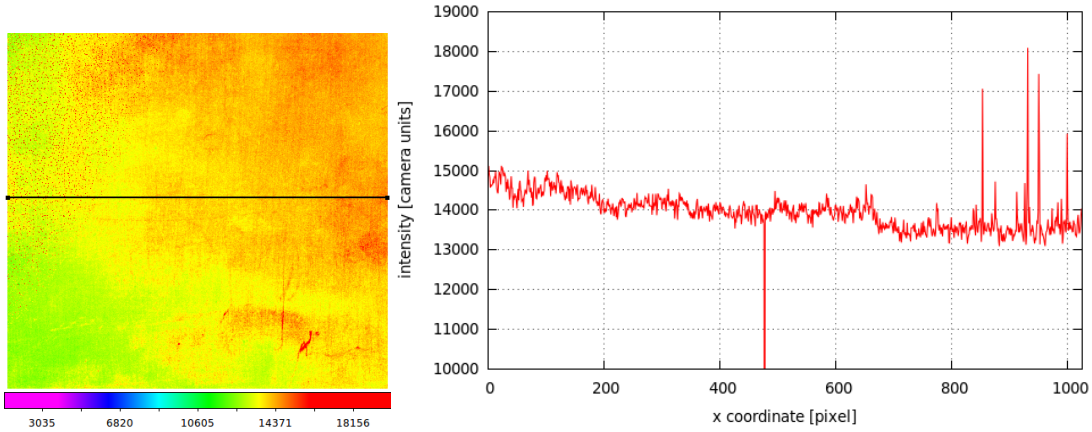

Figure 5.11: left: Image of the light distribution on a Teflon screen irradiated head-on by the 4-color-LED (green) from a distance of about three meters. right: Profile of the light distribution along the black line.

Reference images of the remaining 3 colors of the 4-color-LED

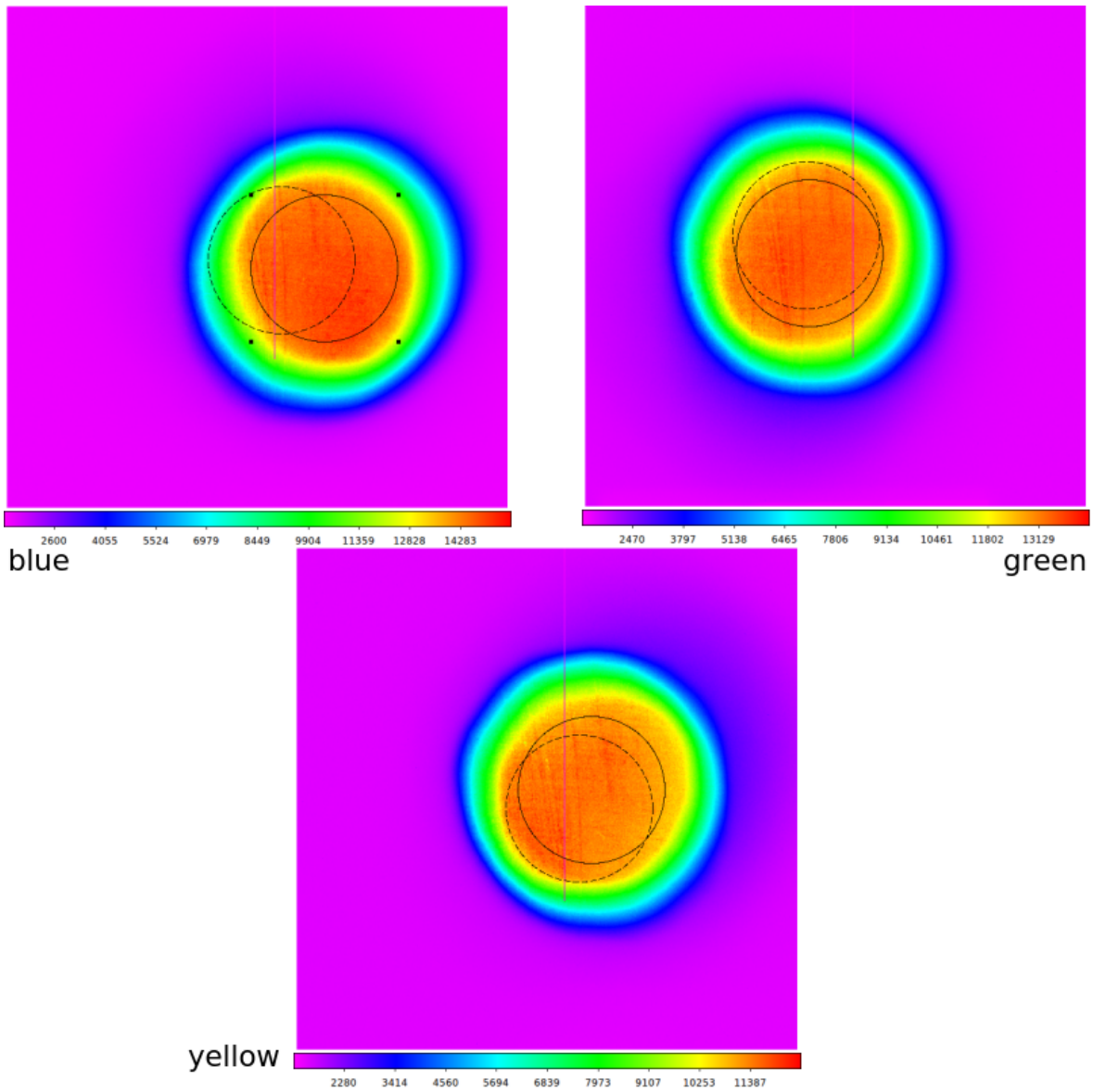

Figure 5.12: Images of light distributions of the 4-color-LED for *blue, green and yellow* at the reference position on the Teflon screen in a distance of about 1.48 m to the LED. The round shape is produced by the iris with a diameter of 6.3 mm, located about 10.8 cm in front of the LED. The dashed circle is located around the center of the MST mirror projected into the image plane and has the same diameter as this projection flat to flat.

Reflectivity calculated with different centers of the mirror projection

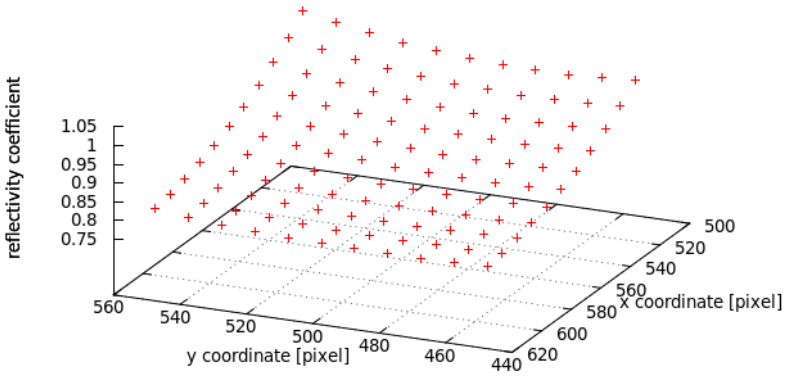

Figure 5.13: Results of the measured reflectivity for *blue* of the 4-color-LED. The center of the projection of the mirror into the images of reference measurement are shifted ten pixel wise up to a total of ±50 pixel, around the position measured with the lasers at (563,505).

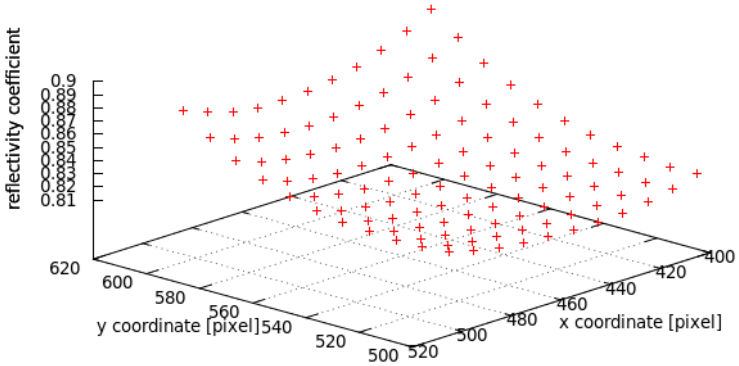

Figure 5.14: Results of the measured reflectivity for *green* of the 4-color-LED. The center of the projection of the mirror into the images of reference measurement are shifted ten pixel wise up to a total of ±50 pixel, around the position measured with the lasers at (453,552).

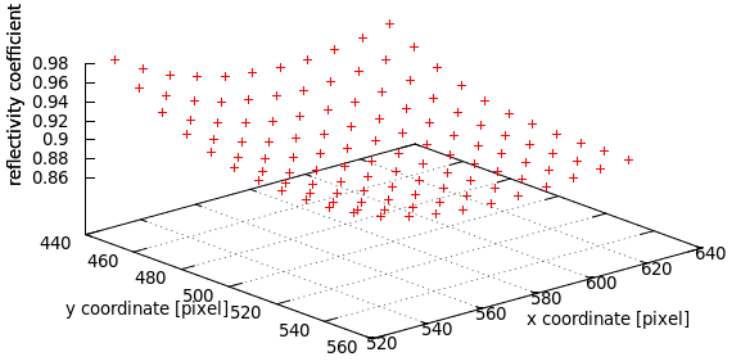

Figure 5.15: Results of the measured reflectivity for *yellow* of the 4-color-LED. The center of the projection of the mirror into the images of reference measurement are shifted ten pixel wise up to a total of ±50 pixel, around the position measured with the lasers at (579,492).

Bibliography

[1] K. Bernlöhr. Monte-carlo images of air showers.

[2] E. Lorenz B.J. Pichler. Production of a diffuse very high reflectivity material for light collection in nuclear detectors. 2000.

[3] The CTA Consortium. Design concepts for the cherenkov telescope array cta. Technical report, The CTA Consortium, 2011.

[4] The CTA Consortium. Status of the nectarcam camera project. Technical report, The CTA Consortium, 2015.

[5] The CTA Consortium. Status of the photomultiplier-based flashcam camera for the cherenkov telescope array. Technical report, The CTA Consortium, 2015.

[6] The CTA Consortium. Status of the technologies for the production of the cherenkov telescope array (cta) mirrors. Technical report, The CTA Consortium, 2015.

[7] F. Aharonian et al. (H.E.S.S. collaboration). A&a 457, 899 (2006).

[8] P. Vincent for the H.E.S.S. Collaboration. H.e.s.s. phase ii. *Proc. of 29th International Cosmic Ray Conference*, Vol. 5, 163 (2005).

[9] Hein Haferkern. *Optik*. WILEY-VCH Verlag GmbH & Co. KGaA Weinheim, 2003.

[10] Eugene Hecht. *Optik*. Oldenburger Wissenschaftsverlag GmbH, 2014.

[11] J. Holder, V. A. Acciari, E. Aliu, T. Arlen, M. Beilicke, W. Benbow, S. M. Bradbury, J. H. Buckley, V. Bugaev, Y. Butt, K. L. Byrum, A. Cannon, O. Celik, A. Cesarini, L. Ciupik, Y. C. K. Chow, P. Cogan, P. Colin, W. Cui, M. K. Daniel, T. Ergin, A. D. Falcone, S. J. Fegan, J. P. Finley, G. Finnegan, P. Fortin, L. F. Fortson, A. Furniss, G. H. Gillanders, J. Grube, R. Guenette, G. Gyuk, D. Hanna, E. Hays, D. Horan, C. M. Hui, T. B. Humensky, A. Imran, P. Kaaret, N. Karlsson, M. Kertzman, D. B. Kieda, J. Kildea, A. Konopelko, H. Krawczynski, F. Krennrich, M. J. Lang, S. Lebohec, G. Maier, A. McCann, M. McCutcheon, P. Moriarty, R. Mukherjee, T. Nagai, J. Niemiec, R. A. Ong, D. Pandel, J. S. Perkins, M. Pohl, J. Quinn, K. Ragan, L. C. Reyes, P. T. Reynolds, H. J. Rose, M. Schroedter, G. H. Sembroski, A. W. Smith, D. Steele, S. P. Swordy, J. A. Toner, L. Valcarcel, V. V. Vassiliev, R. Wagner, S. P. Wakely, J. E. Ward, T. C. Weekes, A. Weinstein, R. J. White, D. A. Williams, S. A. Wissel, M. Wood, and B. Zitzer. Status of the VERITAS Observatory. In F. A. Aharonian, W. Hofmann, and F. Rieger, editors, *American Institute of Physics Conference Series*, volume 1085 of *American Institute of Physics Conference Series*, pages 657–660, December 2008.

[12] S. Lombardi. Advanced stereoscopic gamma-ray shower analysis with the MAGIC telescopes. *International Cosmic Ray Conference*, 3:266, 2011.

[13] Malcolm S. Longair. *High Energy Astrophysics*. University Press, Cambridge, 2011.

[14] S. M. Ritz, N. Gehrels, J. E. McEnery, C. Meegan, P. F. Michelson, D. J. Thompson, and Fermi Mission Team. Fermi (formerly GLAST) Mission Overview. In *American Astronomical Society Meeting Abstracts #213*, volume 41 of *Bulletin of the American Astronomical Society*, page #468.01, January 2009.

[15] Erich Schreiber. Aufbau eines messsystems fuer reflektionsmessungen an h.e.s.s.-teleskopen. diploma thesis, Max-Planck-Institut fur Kernphysik in Heidelberg / Ruprecht-Karls-Universiteat Heidelberg, 2005.

[16] Stefan Schwarzburg. *A Mirror Alignment Control System for Phase II of the HESS Experiment and A Morphology Study of HESS J1837-069*. PhD thesis, Eberhard Karls Universität Tübingen, 2012.

[17] C. M. Urry and P. Padovani. Unified Schemes for Radio-Loud Active Galactic Nuclei. , 107:803, September 1995.

Danksagung

An dieser stelle möchte ich mich bei den Menschen bedanken, die mich auf meinem Weg bis zur Fertigstellung dieser Arbeit unterstützt, bzw. diese erst möglich gemacht haben.

Prof. Dr. Andrea Santangelo: Vielen Dank für das Ermöglichen dieser Diplomarbeit in dem sehr interessanten, vielseitigen und interessanten Themengebiet rund um CTA.

Dr. Gerd Pühlhofer, Dr. Christoph Tenzer, Jürgen Dick, Daniel Gottschall, Felix Eisenkolb, Michael Gschwender, der Werkstatt und den Rest vom Institut: Danke für die viele Unterstützung, angefangen beim Programmieren lernen, Programme erstellen, den Messungen mit dem neuen Messtand und Spiegel schleppen, etc., bis hin zum Korrekturlesen dieser Arbeit.

Diverse Mitgleider meiner Familie: Danke für die nicht nur moralische Unterstützung. Ihr wisst ja schon. ;)

Außerdem eine herzlichen Danke an die kurzen und langen Wegbegleiter während meines Studiums, die mir viel gegeben haben!